2005

Palladium and nickel interactions with stepped 6H-silicon carbide

Andrew A. Woodworth
West Virginia University

PALLADIUM AND NICKEL INTERACTIONS WITH STEPPED 6H-SILICON CARBIDE

By
Andrew A. Woodworth

Dissertation submitted to the
Eberly College of Arts and Sciences
at West Virginia University
in partial fulfillment of the requirements
for the degree of

Doctor of Philosophy
in
Physics

Dr. Charter D. Stinespring, Chair
Dr. Martina E. Bachlechner
Dr. Boyd F. Edwards
Dr. Larry E. Halliburton
Dr. Ayyakkannu Manivannan
Dr. Thomas H. Myers

Department of Physics

Morgantown, West Virginia
2005

Keywords: 6H-SiC, palladium, nickel, AES, AFM, surface preparation.

ABSTRACT

PALLADIUM AND NICKEL INTERACTIONS WITH STEPPED 6H-SILICON CARBIDE

Andrew A. Woodworth

Silicon carbide (SiC) has long been recognized as a semiconductor with potential for use in a number demanding environments. Recent developments in the quality of bulk grown 6H-SiC (and other hexagonal poly-types) have increased interest in issues surrounding the stability of device structures that operate at temperatures in excess of 600^{o}C. It has been observed that the performance of metal-semiconductor devices created on SiC tend to degrade when operating at these temperatures. This change in device performance has been linked to inter-diffusion and reaction at the metal-semiconductor interface. Most of these devices have been fabricated on SiC substrates with surface and sub-surface damage associated with the polishing process (standard surfaces). Recent studies have shown that high temperature hydrogen etching of these substrates removes this damage and produces surfaces with wide atomically flat terraces and nanometer scale steps (stepped surfaces). The basic question this poses is, can such improvements in substrate quality lead to improvements in device performance.

The goal of this research is to better understand the interaction of metals on these stepped surfaces. To accomplish this, detailed surface studies of thermally induced Pd-SiC and Ni-SiC surface interactions have been performed on both the standard and stepped surfaces. The metal films range in thickness from the monolayer level (~0.4 nm) to actual device dimensions (~50 nm) and are deposited under ultrahigh vacuum conditions at ~50 ^{o}C. These films were characterized *in-situ* using Auger electron spectroscopy both before and after annealing at 670 ^{o}C for Pd and 700^{o}C for Ni. The Auger lineshapes provide quantitative and qualitative information on the chemistry of the reaction products. *Ex-situ* atomic force microscopy was used to characterize changes in surface morphology. The results of these experiments yield important insights into the nature of the transport process at the metal-semiconductor interface and the influence of initial surface structure in these processes. In addition differences in the interfacial chemistry for carbide forming metals has been revealed. The results provided insight into the mechanisms where by improvements in substrate quality may lead to improvements in device performance.

ACKNOWLEDGEMENTS

I would like to thank Dr. Charter Stinespring for guiding me through this incredible learning experience. I also owe a great debt to Dr. Martina Bachlechner, Dr. Boyd Edwards, Dr. Larry Halliburton, Dr. Ayyakkannu "Mani" Manivannan, Dr. Thomas Myers, and Dr Kathleen Meehan for not only agreeing to sit on my committee, but also being excellent instructors and mentors. I would also like to sincere thank you the entire Physics Department for their ability not only to do excellent research, but also their ability to take graduate students, from a variety of backgrounds, and make them solid scientist that will benefit their fields for many years to come. I hope that I can live up to the reputation the department has built. I especially, need to thank Siobhan Byrne and Sherry Puskar for their infinite knowledge of how the college works. With out you I would probably be buried to my eyeballs in paper.

Another group that deserves my thanks and gratitude is the Department of Chemical Engineering, who has hosted this wandering physicist for the last five years. A special thanks to Dr. Al Stiller for his translations of papers and chemical insights, Jim Hall for machining all the odds and ends that my research demanded (especially those made of Mo), and Bonnie Helmic and Linda Rodgers for their knowledge of the College of Engineering works. I would also like to than Kolin Brown and the Lane Department of Computer Science and Electrical Engineering for use of the chemical hoods in 309 Engineering Research Building.

I have also been graced with lab-mates, past and present, with whom I have learned and struggled with: Charlie Peng, Katie Ziemer, Vikram Tolini, Srikanth Raghavan, and Tobias Denig. Special thanks to Kyoung-Nae Lee for her work on hydrogen etching of SiC. May your paths be as rich and interesting as mine. I would also like to thank Dr. Bill Chisholm, Dr. Jimmy Stephens at NIOSH, and Dr. Joanna Matheson CPSC for their insights and support this process.

I would also like to thank the researchers at U.S. NETL Facility, in Morgantown WV, for use of their JEOL 4210 SPM and CI Instruments blackbody source. I would especially like to thank Jim Poston, Dr. Steven Woodruff, Dr. Chris Johnson, Ed Fisher and Dr. Rajani Siriwardane for their comments, thoughts and support.

Last but not least, I owe a great debt to my friends and family. Thank you to everyone that has supported and shared in my experiences here in Morgantown, you have made this an incredible experience. To Dad, Mom and Jim: Thank you for your love and support. I would also like to send a special thanks to the Reynolds family for being my surrogate family in Morgantown, and to Bob for all of the added fun and excitement.

This research was funded by U.S. Department of Energy (DOE Contract #DE-FC26-01NT41273), West Virginia Space Grant Consortium, and the Office of Naval Research (ONR Contract #N00014-01-1-0571, and ONR Contract #N00014-00-1-0293 for supporting my research.

TABLE OF CONTENTS

TABLE OF FIGURES

CHAPTER 1: INTRODUCTION

1.1 Overview and Problem Statement

In recent years, significant developments in the quality and reduction in price have made commercially grown bulk hexagonal silicon carbide (α-SiC) a viable material for use as a device platform. These devices are expected to operate in a variety of harsh environments. Of particular interest are high temperature (>600 ^{o}C)[1] applications. To create these devices, a number of metals must be employed in the fabrication and the packaging of the device. Unfortunately, when SiC devices are operated at high temperatures and extended times, an unacceptable amount of degradation in the performance has been observed.[2] This degradation comes from intermixing and reaction at the metal-semiconductor interface found in these devices.

Although numerous studies have tried to stabilize the SiC-metal interface by using combinations different metals and/or oxide layers, little has been done to understand the impact of surface preparation of the α-SiC substrates. Currently, after wafers are cut from the boule, they are mechanically polished and then shipped to the buyer. The buyer then uses a wet chemical etching process to prepare the surface for device fabrication. In subsequent discussions this is referred to as the *standard surface*. Unfortunately, mechanical polishing leaves a wide variety of surface and sub surface damage that is structurally unaffected by the chemical processing. Recently, a high temperature hydrogen etching technique has been developed for removal of the surface and subsurface damage. This technique leaves behind an ordered surface consisting atomically flat terraces.[3] In subsequent discussions, this referred to as *stepped surface*.

This dissertation presents the results of studies that compare and contrast interface interactions of two different stepped and standard surfaces. For these investigations nickel and palladium were chosen as the metals for this study. This choice was motivated by their possible device application, and because of the differences in their know interactions with C and Si. Ni is known to form both metal silicides and a carbide, while Pd only forms metal silicides.

Chapter 1 is designed to give an overview of the problem, an introduction to the properties and applications of SiC, and a brief overview of some simple metal-SiC device structures that involve Ni and Pd. Chapter 2 gives background information on SiC, and a discussion of previous work done on metal-SiC interfaces. Chapter 3 presents the experimental techniques, procedures, and methods used perform the study. In Chapter 4, the results are presented and discussed. Finally, Chapter 5 contains conclusions and recommends future studies.

1.2 Importance of Silicon Carbide

Silicon devices are employed in a myriad of different applications ranging from household electronics to space applications. Despite the success of silicon based electronics, demand for higher integration of electronics in applications in harsh environments (both physically and chemically harsh) and high power applications have driven research into new materials. One such material is SiC a robust, wide bad gap semiconductor with a high breakdown electric field, excellent thermal conductivity, and chemical inertness. Listed in Table 1 are some of SiC's Thermal and electrical properties as compared to Si.

Table 1.1: Selected properties of 4H and 6H SiC.[4,5,6,7,11,24,14]

	6H-SiC	4H-SiC	Si
Bandgap (eV)	3.26	3.03	1.12
Breakdown Electric Field [V/cm (for 1000 V operation)]	$2.2x10^6$	$2.4x10^6$	$2.2x10^5$
Saturated Electron Velocity (cm/s)	$2x10^7$	$2x10^7$	$1x10^7$
Electron Mobility [cm^2/Vs (N_d=$1x10^{-16}$cm-3)]	800	1000	1350
Thermal Conductivity (W/cm*K @RT)	3.0-3.8	3.0-3.8	1.5
Young's Modulus (GPa)	>700	>700	190
Melting Point (^oC)	1414	1800*	1800*
Electron Affinities (eV)	3.7-4.0	3.1-3.6	4.05

*Sublimates

The SiC's wide band gap prevents electrons from being thermally excited from the valance band to the conduction band as easily as Si. This, along with SiC's physical stability at elevated temperatures[8], and high thermal conductivity, make SiC an ideal semiconductor for high temperature situations where minimal cooling is available. Such applications include control modules integrated into both automobile and aircraft engines. Integrated electronics would eliminate a large amount of wiring currently needed in these applications, which is a source of weight and possible electrical failures.

SiC also resists most chemical attacks and it is not etched by most acids.[9,10] This chemical inertness makes SiC ideal for sensors in chemically harsh environments. Typical applications include exhaust streams from, automobiles, gas turbine engines, and power plants. Sensors in these locations would provide real-time monitoring and hence

more control of combustion processes. Improved efficiencies would help reduce both the economic and environmental cost of power production.[11,12]

SiC's high electric breakdown field and thermal conductivity make it ideal for high voltage applications (5 kV-10 kV). These include thyristors used in traction control and high-voltage DC transmission.[13] The combination of high electric breakdown field with the wide band gap allows heavy doping while maintaining the desired electrical characteristics of the material. This makes SiC a desirable material for high frequency applications.[14] SiC has also been shown to be a suitable material for high radiation environments.[15] Applications include high energy beam lines and space craft.[16]

1.3 Ohmic Contacts and Schottky Barriers.

When a semiconductor and metal are put into contact they will form either a Schottky or an Ohmic junction. Ohmic contacts are desirable for making contacts to electronics where electrons need to be transferred with little or no resistance. While Schottky barriers make p-n like junctions and are uses in variety device structures. The nature of the metal-semiconductor junction is determined by the electron affinity of the semiconductor and the work function of the metal. In the fabrication of simple gas sensors, the Schottky barrier is the key component as described later.

A Schottky junction is formed if the electron affinity of the metal greater than that of the semiconductor. This case is shown in Figure 1.1. When the materials are brought together the Fermi energy must be kept constant over the materials and the vacuum levels must be the same at the interface, hence, the band structure of the semiconductor is bent near the interfaces as depicted in Figure 1.1. Here where Φ_m and Φ_n the work functions for the metal and n-type semiconductor respectively, and χ is the electron affinity of the semi-conductor. For metals the electron affinity is the same as the work function. The Schottky barrier can act much like p-n junction when a voltage is applied with forward biasing (for an n type junction) allowing electrons to flow from the semiconductor to the metal. In a reverse bias situation there is still a barrier for the electrons to pass over, and hence the current is limited as in a p-n junction.

Another important characteristic of Schottky junctions is the width of the barrier. The probability of an electron tunneling through the Schottky barrier is determined by its width. The width of the Schottky barrier is determined by the surface density of charge states of the metal-semiconductor interface, which is in turn, is controlled by the doping

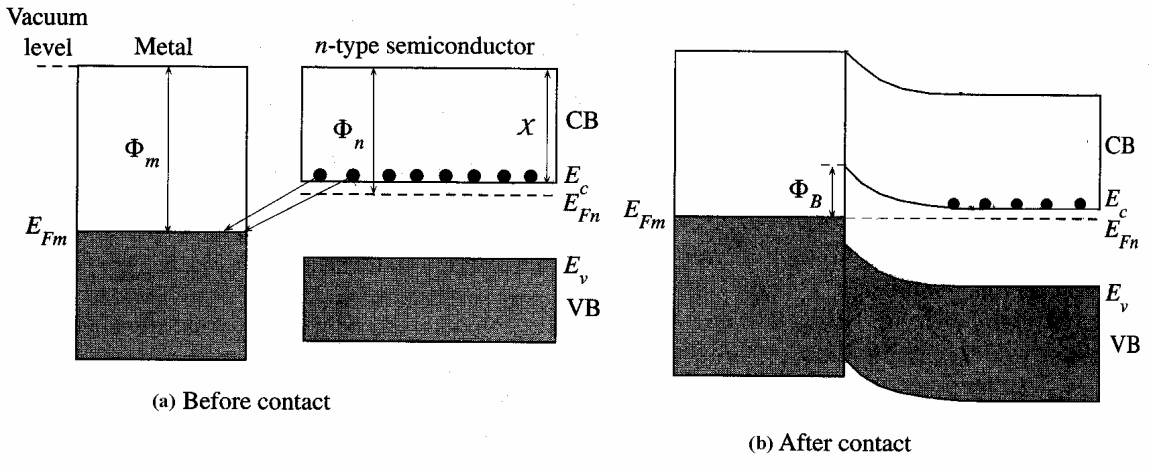

Figure 1.1. Diagram of a Schottky barrier formed by a metal and n type semiconductor.

or defects present at the interface. If the barrier becomes too thin the junction becomes Ohmic. For a more in-depth discussion of these effects please read J. Crofton *et al*.

Ohmic contacts formed then the electron affinity of the metal is smaller then the semiconductor. Again the Fermi energy must be the same across both materials and the vacuum level must be the same at the interface. Therefore the conduction band of the semiconductor must bend down (Figure 1.2).

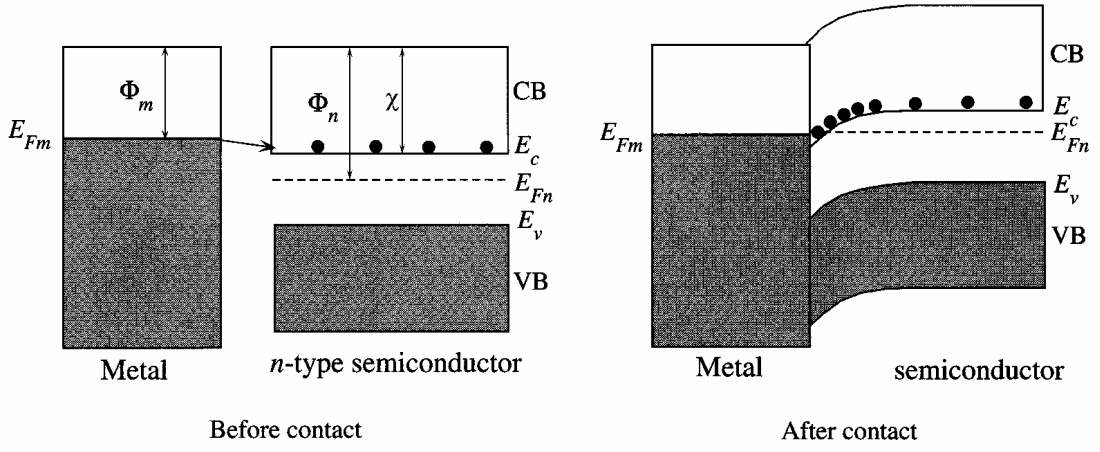

Figure 1.2. Illustration of an Ohmic junction.[17]

1.4 Importance of Palladium

Pd has an FCC crystal structure with a cube edge of 0.389 nm. In reference to SiC, Pd is of interest for several reasons. First of all, it has a relatively high melting point (1554.9 ^{o}C). This makes using Pd at elevated temperatures possible. Second, Pd is known as a refectory and catalytic material. Of particular interest are the interactions of Pd with H_2, O_2, and a variety of hydrocarbons. In these reactions, the Pd facilitates a reaction that produces H_2O, N_xO_y, and CO_2 with excess H atoms being absorbed by the Pd.[18] This is illustrated schematically in Figure 1.4.

Pd is also known to form compounds with silicon known as silicides. These silicides can come in a variety of different forms with formula Pd_xSi, where x = 1,2,3 ect. The most commonly observed structures are PdSi (orthorhombic), Pd_2Si (hexagonal and rhombohedral), and Pd_3Si(orthorhombic).[20]

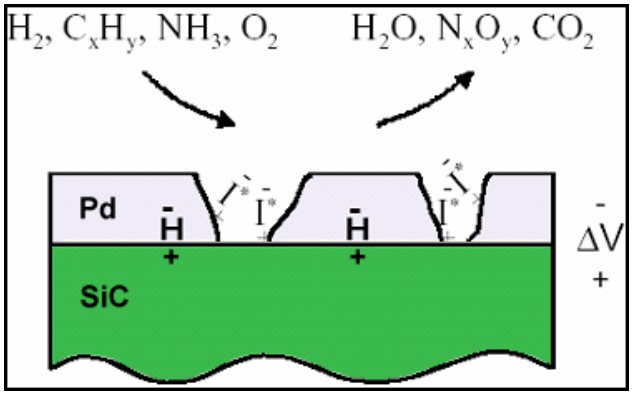

Figure 1.3. Illustration of the operation of a MOS gas sensing device.[19]

Pd has an electron affinity of 5.12 eV in the elemental for and 5.0 eV in the silicide form.[21] This high electron affinity means that Pd forms a Schottky barrier with SiC. When H ions are positioned on the SiC-Pd interface as shown in Figure 1.4, the local charge density is changed and hence changes the barrier height altering the electrical response of the diode structure. Figure 1.5 demonstrates the difference in current-voltage characteristics of a junction in the presence of O and propane.. The shift in electrical characteristics with absorbed H from hydrocarbon interactions makes Pd a viable candidate for gas sensor work in

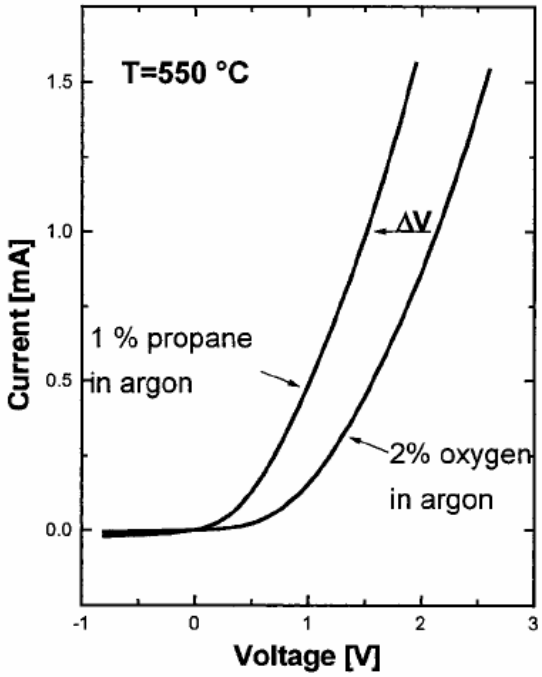

Figure 1.4. Electrical response of a Schottky junction made of refractory materials and SiC when exposed to different gasses.

exhaust streams.

1.5 Importance of Nickel

Ni forms an FCC structure with a cube edge of 0.325 nm. Like Pd, Ni has a high melting point (1455 ^{o}C) which makes it useful for high temperature applications. Ni forms both silicides and carbides. Commonly found silicides include Ni_2Si (orthorombic), NiSi (cubic), and $NiSi_2$ (orthorombic). The common form of the carbide is Ni_3C (hexagonal). This state is metastable and does not exist above 500 ^{o}C.[22]

Ni has a work function of 5.15 eV in the elemental form and 4.1-4.5 eV in the silicide form.[23],[49] Therefore, a Schottky diode with varying electron transmission characteristics depending on the doping concentrations of SiC can formed Because of Nickel's high melting point and Schottky barriers Ni has been studied extensively for use in high power/temperature rectifiers, and as contacts in high power/temperature devices.[24]

CHAPTER 2: METAL SILICON CARBIDE INTERACTION

Based on the preceding discussion, interaction of metals with SiC under a variety of conditions is of critical importance to device formation and function. For this study, we have chosen Pd and Ni as the metals of interest because of their potential uses and known interactions with C and silicon. Pd is a refectory material that forms a Schottky junction with 6H-SiC, and it is known to form silicides. Ni also forms Schottky junctions with SiC, and forms both silicides and carbides. This chapter is gives a brief overview of silicon carbide. This includes a discussion of the crystal structure, the growth process, limiting defects, standard methods of surface preparation, and metallization of SiC. In particular previous research related to Pd and Ni interactions with SiC is reviewed. A key difference between the experiments in the studies discussed in this chapter (the literature) and the ones presented in Chapter 4 (our work) is the method of surface preparation. Therefore, special attention is given to surface preparation methods used in the experiments discussed below.

2.1 A General Silicon Carbide Background

SiC consist of silicon and C atoms sp^3 bonded in what is known as a bi-layer, which can be stacked to form cubic, hexagonal, and rhombohedral structures. In total more than 250 different polytypes can be formed.[26] Polytypes are referred to by a number followed by a letter (e.g. 6H). The number represents the number of Si-C bi-layers are contained in each unit cell. The letter refers to the structure (H=hexagonal C=cubic R=rhombohedral) of the crystal.

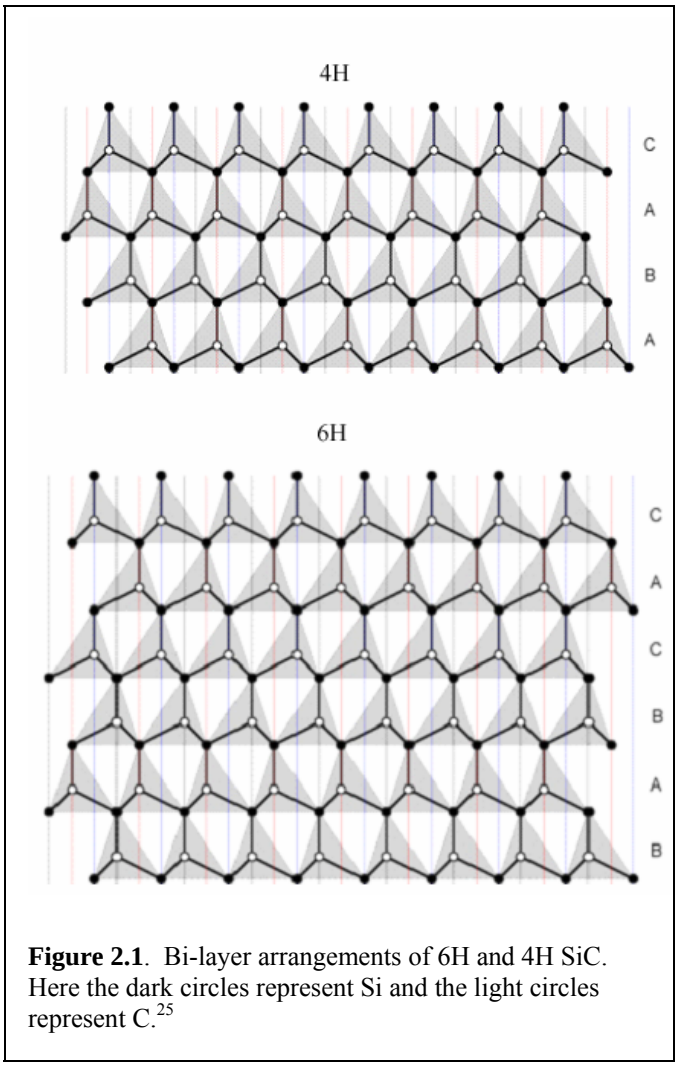

Figure 2.1. Bi-layer arrangements of 6H and 4H SiC. Here the dark circles represent Si and the light circles represent C.[25]

There is one cubic polytype which is referred to as 3C-SiC or β-SiC. There are also numerous hexagonal polytypes referred to collectively as α-SiC. The 6H, 4H, and 15H polytypes are the most commonly observed in PVT growth processes.[27] The most commonly available SiC wafers are n type 4H and 6H-SiC. Figure 2.1 illustrates the bi-layer structure sequence used to obtain the 4H and 6H structure.

2.1.1 Growth Process and Limiting Defects

The conventional process for growing large single crystal semiconductors in boules from a melt is impractical SiC. This is because melt growth of SiC requires pressures greater than 10^4 atm and temperatures in excess of 3200 ^oC.[29] In 1955, Von J. A. Lely published a paper describing a physical vapor transport (PVT) method to grow single crystal α-SiC on the walls of a graphite reactor in an inert gas.[28] Today, large single crystals are grown via the Modified-Lely process. The modified Lely process is a PVT method that employs a seed crystal to start the growth instead of allowing the crystals to nucleate and grow on the walls of the reactor.[27] The method also uses an inert background gas which can be used to introduce dopants in the crystal.[29]

Despite being able to grow single crystal α-SiC with increasing boule diameters, many different defects that effect device performance have limited the usefulness of the material. Among these defects are thermal decomposition cavities, basal plane dislocation, screw dislocations and micropipes. Of particular concern are screw dislocations and micropipes because of their effects on the electrical properties of α-SiC. Micropipes have been shown to reduce the breakdown voltages more than 50%, to host microplasmas, and to increase leakage currents.[44] Screw dislocations have been observed to reduce the breakdown voltages up to 30% and to reduce carrier lifetime.

Currently there are an increasing number of vendors of 6H-SiC in the USA. Two of the oldest are CREE Inc. and Sterling Semiconductor which was recently bought by Dow Corning. This work focuses on CREE and Dow Corning/Sterling substrates. Both companies offer 6H-SiC wafers with micropipe densities of less than 15 per cm^2. However, screw dislocations are still on the order of 10^4 per cm[4,30]

2.1.2 Standard Surface Preparation

Surface preparation plays a significant role in the metal-SiC interaction. This section describes the standard method for preparing SiC as a substrate for device fabrication.

α-SiC is grown in a single crystal boule and then is cut either perpendicular or at a specific angle to the c axis. The wafer is then polished by the vendor and shipped to the devices fabricator. The device fabricator uses organic solvents (i.e. trichloroethylene, methanol, acetone, ect.) to remove contaminants introduced by polishing and handling of the wafers. The next step is to remove the native oxide by immersing the SiC in concentrated hydrofluoric (HF) acid. This produces the SiC surface on which most devices are fabricated. It should also be noted that the general procedure outlined above is similar to the procedure for cleaning Si before using it as a substrate for device fabrication.[31,32,33,34] It should be noted that to date there has only one other group (Hunter *et al.* at NASA Glenn, Cleveland OH) who investigated the effects of surface preparation on metal/SiC devices, and this work was published only recently.

2.2 Metallization of SiC

As mentioned before the goal of creating SiC devices is to create electronics that can operate at elevated temperatures in excess of 600 ^{o}C and harsh environments (e.g. gas sensors in the exhaust from a power plant) for extended periods of time. The last challenge in making these devices is to control inter-diffusion and reaction of the metal-SiC interface. Metallization of SiC has been studied since the mid 1980s, and it continues to be an area great interest.[36]

2.2.1 Palladium-Silicon Carbide Interactions

As mentioned before, Pd-SiC devices can be used for diode gas sensors. These gas sensors have been demonstrated to have a sensitivity to both hydrogen and hydrocarbons[35,37]and have been operated at temperatures of up to 600 ^{o}C.[36] The simplest of these structures is a Schottky diode formed by a thin Pd film deposited directly on the SiC substrate. Figure 2.2 shows an example of such a gas sensor fabricated by researchers at the NASA Glenn research Center. The two large squares are the diode structures and associated contacts. Unfortunately, long term heating in application environment severely affects the sensitivity of these devices.[37]

Key early studies of metal-SiC interactions were made by V. M. Bermudez[38] at the Naval Research Laboratory in the early 1980s. Bermudez conducted his studies on (0001) 6H-SiC wafers that had been cleaned by Ar^{+}-ion bombardment. In his work, he concluded that Pd and Si start to react at room temperature to form Pd_3Si and Pd_4Si. When the sample were annealed Bermudez found that a mixture of Pd_2Si and Pd_3Si were present. He concluded that "dissolved C may inhibit the conversion to Pd_2Si the most stable phase, which occurs for Pd/Si." The primary difficulty in interpreting Bermudez's results is that Ar^{+}-ion etching amorphizes the SiC surface[39] and it is therefore not clear that the results accurately reflect the true surface interactions with Pd. In particular it is possible

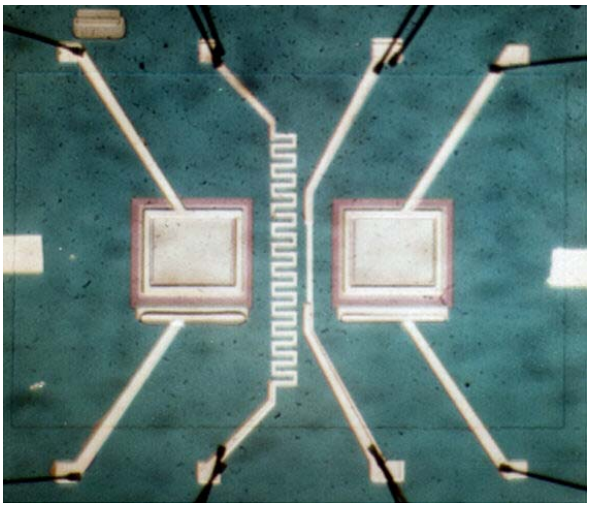

Figure 2.2. Pd-SiC hydrogen gas sensor Courtesy: NASA Glenn Research Center.[36]

that the native SiC surface may not form Pd_2Si and Pd_3Si (for example) under equilibrium conditions.

One of the most useful results of Bermudez's work was to link the line shape of the Si-LMM spectra to the specific stoichiometry of the Pd silicide. This key piece of information will be discussed in the experimental section and used in our data analysis.

Extensive research has been done at the NASA Glenn Research Center, from 1990 to the present, in which many gas sensing devices have been fabricated and tested.[2,37,40] Until recently all of these have used the standard method of surface preparation. Their results demonstrate the importance of inter-diffusion and reaction at the metal-semiconductor interface.

"Post-mortem analyses" of these devices revealed a thin passivation layer composed of PdO and SiO_x on top the Pd/SiC structure. Further analysis revealed that the interfacial region was greatly broadened and composed of Pd_xSi with the predominate species being PdSi and Pd_2Si. Graphite was also found to be present. L-Y. Chen *et al.*[2] concluded "In order to stabilize the diode properties at high temperature, the diffusion and chemical reactions at both the surface and metal-semiconductor interface of the device must be minimized."

Other papers have highlighted the implications of both silicides and graphite formation. First of all, silicide and graphite both have different electron affinities than Pd. Therefore, the Schottky barrier height will be altered. Also several studies show that C and Si vacancies at the interface are responsible for altering the electrical properties.[41,42]

In other studies at NASA, oxide layers of 5.0 nm in thickness were created to form a diffusion barrier between the Pd and SiC. This oxide layer did retard the inter-diffusion Pd, Si and C but at the cost of sensitivity. This is illustrated in Figure 2.3 which shows the current response of sensors with (b) and without (a) the oxide layer before and after annealing. Before annealing and after, the sensor without the oxide layer has a current response a 100 time grater than the sensor with the layer. This is in contradiction to work done elsewhere[43]. Specifically Ekedahal *et al.* report that the sensor depends on having a thin oxide layer (0.5-1 nm) on which the absorbed H ions collect. It is unclear why this discrepancy exist. Also, there is a remnant oxide that is left after the SiC is HF treated which has been consistently observed in out lab and is discussed in Chapter 4. This surface oxide is not mentioned in any of the papers from the group at NASA GRC.

In 2002 Nuedeck *et al.* developed a method to produce atomically flat mesas on SiC on which they fabricated devices.[44] These mesa devices showed remarkable improvement in long term device operation. After 500 hours of operation at 300 ^{o}C, the device created on the atomically flat mesa had a response 100

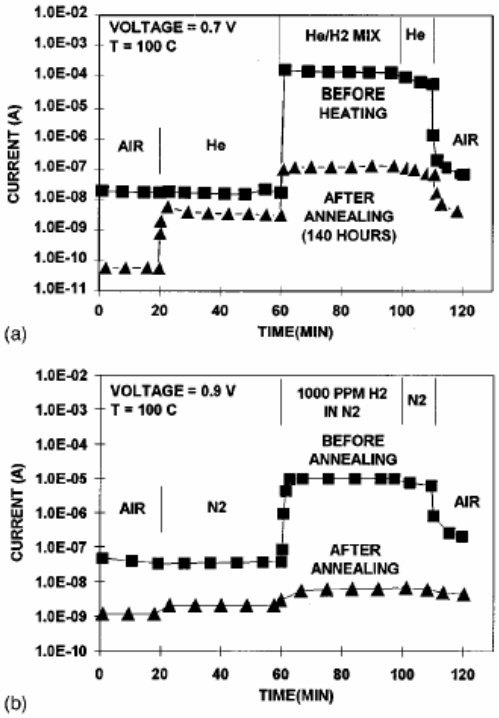

Figure 2.3. The forward current vs. time at 100 °C before and after annealing at 425 °C for 140 h in air of (a) a Pd/SiC diode at 0.7 V and (b) a Pd/SiO2 /SiC diode at 0.9 V.[2]

times that of the device created on a standard surface.[45] They have also had some success with using chromium carbide as a diffusion barrier in conjunction with platinum (another refectory metal with similar proprieties and issues as Pd). These studies on atomically flat mesas closely matches the studies presented in Chapter 4 of this dissertation.

2.2.2 Ni-Silicon Carbide Interactions

Tounge *et al.*[46] was responsible for much of the early work on the interaction of Ni with silicon, and this was the basis for many of our initial thoughts surrounding the metallization of SiC. A recent paper (January 2005) by Nikitina *at al.*[42] gives an excellent review of the issues surrounding the interaction of Ni with SiC and the implications of those interactions for the electronic structure of Schottky junctions. Robbie *et al.*[47] provides a set of experiments that most closely follow ours in the materials, preparations, conditions, and analysis methods.

Prior to the work of Toung *et al.*, it was known that several monolayers of Ni will react with Si at room temperature to form Ni-silicides. Toung *et al.* showed that the thickness of initial Ni layer deposited on the Si (111) determines the crystallinity of the silicide formed after annealing. When Ni films with an initial thickness of 0-0.7 nm are annealed at 450 ^{o}C-550 ^{o}C, a single crystal silicide film of a particular orientation is created. For Ni films of initial thickness of 0.8-1.5 nm an amorphous silicide layer is formed. When a film of 1.6-2.0 nm of Ni was deposited and annealed single crystal silicide with different orientation is formed. Annealing thick initial films (2.1 nm and greater) produces a polycrystalline film. Ni-Si (111) experiments were annealed. The same experiment was tried for Si(100) surface with similar results for initial films thickness greater than 1.0 nm but less than 3.0 nm. In both cases, subsequent depositions

and anneals of Ni reproduced the same single crystal film. One key remark that was made is that the crystallinity was not detected if the surface had any detectable contamination. Therefore Toung *et al.* stressed the importance of the pretreatment.[48]

Nikitia *et al.* recently did an extensive review of the previous work on α-SiC (standard surfaces only), and produced some revealing data that gives insight into the effects of silicide formation on the electronic structure. A problem with Ni-SiC junction is that they tend to become Ohmic after reaching high temperatures. The formation of Ni silicides starts about 500 ^{o}C. Experimental fitting of electrical data using the thermionic-field emission model gives a Schottky barrier height of 0.35 eV -0.4 eV.[11,49] Based upon the possible range of work functions of nickel silicides (4.6 eV-5 eV) and the electron affinity of α-SiC (3.08 eV-4.0 eV) a SiC-Ni-silicide junctions should form a barrier of 0.6 eV. Nakitina *et al.* mentioned roughness of the surface may be another factor that plays a role in the reduction of the barrier. Other direct measurements of the barrier height revealed un-uniform values[50]. In addition Ni_2Si was found to be present in the mixture of silicides present at 600 ^{o}C. Ni_2Si is usually only reported to form at temperatures greater than 900 ^{o}C. These observations led Nikitina *et al.* to "conclude that Ni_2Si formation is not the major factor in forming Ohmic contacts on *n*-type SiC."

Ni is well known as catalyst in the graphitization of C.[51]. Han *et al* observed that different microstructures are formed when 100 μm thick Ni films are annealed on 4H-SiC (prepared using standard techniques) at different temperatures. This is illustrated by Figure 2.4 which is taken from their work. The 100μm film starts out (a) with a sharp Ni-SiC interface, but after annealing at 800^{o}C, Si out-diffuses to form $Ni_{31}Si_{12}$ on the surface with Ni_2Si underneath. This leaves behind a C rich band close to the SiC substrate.

Annealing at 950°C (c) produced a significant out-diffusion of C, which resulted in a graphite layer on the surface, a mixture of Ni silicides underneath, and a C rich layer near the SiC substrate. These observations have lead to a variety of opinions about the role of C in the changing electrical characteristics of Ni-SiC junctions.[50,52,53]

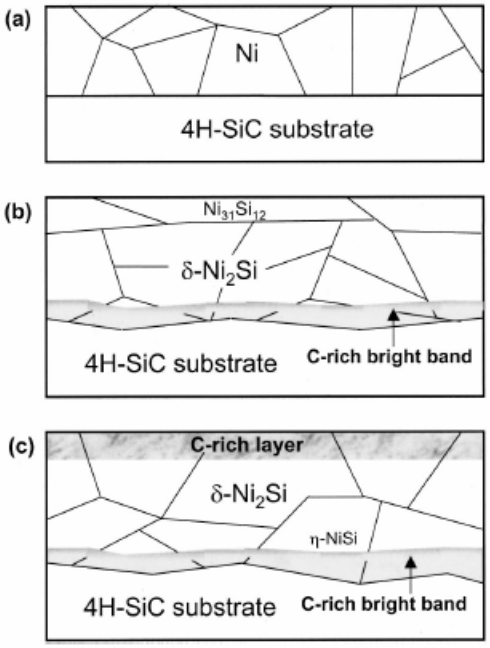

Figure 2.4. Schematic illustrations of the microstructure at the interface of the Ni contact, deduced from cross-sectional TEM and XRD analysis: (a) as deposited and after annealing at (b) 800 °C and (c) 950 °C.

Nikitina *et al.* performed a set of experiments aimed at determining the role of C in changing the electronic structure of the Ni-SiC junction. Their substrates were, n-type 4H-SiC cut 8° off axis with a polished C face obtained from CREE, Inc. Reactive ion etching was used to remove the thin insulating layer which comes on the wafer from the vendor. This was followed by a wet oxidation step, and finally, oxide removal via HF dip. Please note that the final roughness, and/or spectroscopic analysis of the surface after the pre-deposition preparation is not provided. Therefore there is no gauge for the possible initial chemical or crystal state of the surface.

What Nikitina *et al.* were able to determine is that the C vacancies at the metal-semiconductor interface are responsible for the changes in electrical characteristics.

Therefore, they conclude that positively charged C vacancies near the interface region reduce the Schottky barrier width and increase the electron tunneling probability,[54] and it is this rather than the silicide formation, per-se, that changes the electrical properties.

Nikitina *et al.* also stated "the change in contact behavior from the rectifying to Ohmic caused by these vacancies, may be masked by high doping levels and/or poor crystal quality of the initial SiC layer used in the experiment." As will be shown later, surfaces prepared by standard preparation methods have surface defects that are the result of wafer polishing.

Robbie *et al.* examined Ni-SiC interactions to understand the formation of Graphite intercalation compounds (GICs). These compounds are not of interest to our studies but, the means and manner by which the study was carried out is close to the experiments presented in this dissertation were conducted. The similarities are: both studies used Ni on stepped 6H-SiC (0001) at elevated temperatures with initial Ni film thicknesses on the order 2.5 monolayers (ML) (0.4 nm) using AFM and AES as methods of analysis.

Robbie *et al.* used on axis 6H-SiC (0001) from CREE Inc. The samples were chemically cleaned and HF dipped . Samples where then hydrogen etched in a hot wall reactor at 1500 ^{o}C for 30 minutes This removed material to an estimated depth of 200 nm leaving a stepped surface. After hydrogen etching samples were stored under high vacuum until loaded into a UHV system. The UHV system was equipped with an *in situ* STM, sputtering source LEED, and sample heating system. Once in the UHV system, an initial 2 minute, 950 ^{o}C anneal was performed to remove any surface impurities. Ni films were deposited by dc magnetron sputtering using Ar gas. Heat treatments were done at

800 ^{o}C, 900 ^{o}C, and 1000 ^{o}C. LEED and STM images were taken before and after each step. *Ex situ* analysis includes atomic force microscopy (AFM) and microspot Auger electron spectroscopy (AES).

These experiments yielded two simple results: Two different types of 3D islands formed when Ni deposited on an atomically stepped 6H-SiC surface was annealed. Type 1 islands were observed after annealing at 800 ^{o}C and tended to be 100 nm to 250 nm in diameter, 20 nm to30 nm high and did not seem to have any preferential position on the step or terraces. They also had flat tops and exhibited an ordered structure of Ni on graphite when examined using STM. Type 2 islands were observed after annealing at 1000 ^{o}C and tended to be about 1.5 μm in diameter and 10 nm in height. They seem to be NiSi with a Si rich surface. For the most part, type 2 islands like the type 1 islands did not appear to have a preferential orientation. Sometimes, however, type 1 and type 2 islands appeared together.

CHAPTER 3: EXPERIMENTAL APPROACH

This chapter has three main purposes. a), to outline the equipment and techniques used to run the experiments (Section 3.1), b), to give background information on the analysis techniques used to collect data (Section 3.2),c), to describe in detail the procedures used to run the experiments (Section 3.3). The discussion draws heavily on the work done by former researchers in this lab, Peng and Ziemer.

3.1 Experimental Instrumentation

This section describes the two equipment used to prepare the SiC substrates deposit Pd and Ni. Section 3.1.1 describes a UHV system that that was used to deposit and anneal metals and SiC substrates, along with the chamber that houses the Auger Electron spectrometer. Section 3.1.2 describes the high temperature furnace used to hydrogen etch SiC in the process of preparing substrates.

3.1.1 UHV System

All of the experiments were conducted in the ultra-high vacuum system pictured in Figure 3.1. The system consists of two chambers: One chamber for growth, and another for analysis. Both chambers have base pressures ~$5x10^{-10}$ Torr. The growth chamber is pumped by a Varian turbo molecular pump and a Leybold turbo molecular pump with a combined pumping capacity of 850 l/s. The analysis chamber is pumped with a Perkin Elmer TN BX3 ion pump (1200 l/s) and an auxiliary sublimation pump.

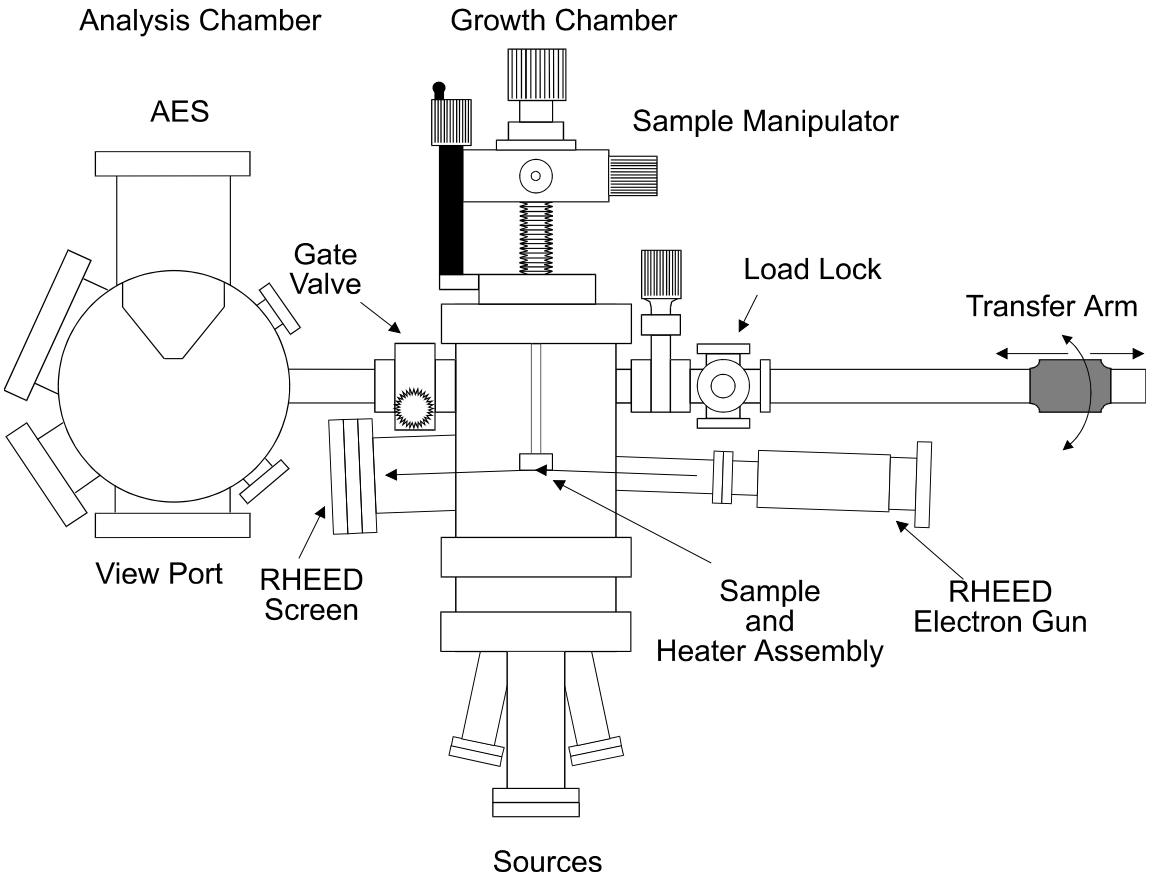

Figure 3.1. Schematic of the UHV system used in the experiments.

Samples are mounted on a molybdenum puck (Figure 3.2) using tantalum wires, and then are introduced into the system via a load-lock. The load-lock is pumped out by a Pfeiffer pumping stand to a pressure of 10^{-7} Torr prior to opening the gate valve to the growth chamber. Samples are transferred between the load lock, the growth chamber, and the

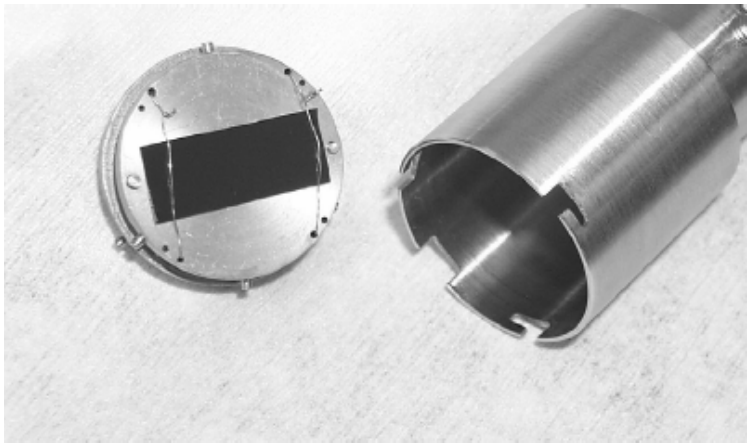

Figure 3.2. Molybdenum sample puck and holder.

analysis chamber, and the analysis chamber by a magnetically coupled transfer arm.

The growth chamber is equipped with a precision leak valve for doing gas source molecular beam epitaxy (GSMBE) and an Applied Epi High Temperature Effusion Cell, model EPI-10-HT (Figure 3.3), used for metal depositions. The high temperature cell is capable of temperatures of up 2000 ^{o}C. Metals are held in a BeO liner inside of a W crucible and heated via tungsten filaments. A thermocouple touching the base of the crucible monitors the temperature. The growth chamber is also equipped with an *x, y, z* and θ sample manipulator with a built in sample heater and k-type thermocouple. An in-depth description of the sample manipulator, heater, and thermocouple is given by Ziemer. While the back face temperature is monitored by the k-type thermocouple, an optical pyrometer (Omega Fiber Optic Infrared Sensor-OS1562) was employed to

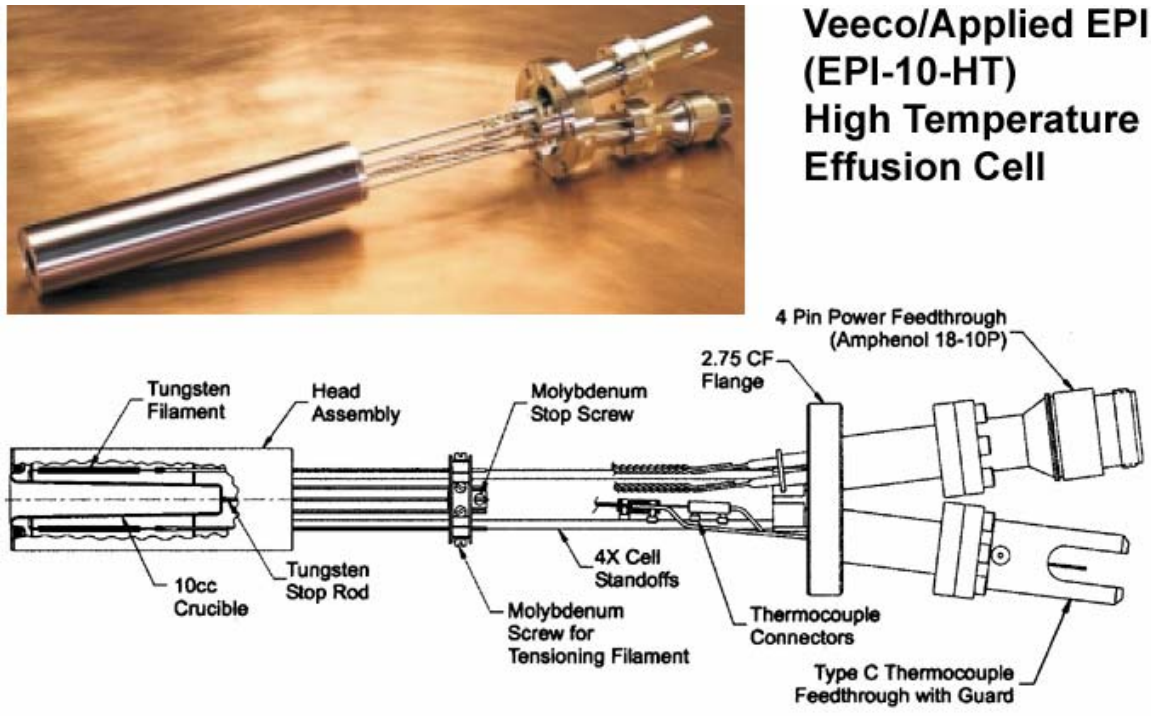

Figure 3.3. High temperature source—Courtesy of Veeco/EPI

monitor the front face of the sample. The growth chamber is also equipped with a Staib Instruments Reflection High Energy Electron Diffraction (RHEED) device to monitor surface evolution and a Physical Electronics argon ion sputtering gun to prepare surfaces.

The analysis chamber is equipped with a Physical Electronics scanning Auger electron spectroscopy system consisting of a Physical Electronics model 15-110A single pass cylindrical mirror energy analyzer with internal electron gun. Data accusation is performed with an RBD Enterprises 147 computer interface and Auger Scan software.

3.1.2 High Temperature Hydrogen Furnace

High temperature hydrogen annealing was used to create atomically stepped surfaces on 6H-SiC. A schematic diagram of this apparatus is shown in Figure 3.3. The high temperature hydrogen 48" alumina tube furnace (1730-12 HT Furnace) manufactured by CM Furnaces Inc. was used to perform the hydrogen annealing. The furnace is designed operated at temperatures up to 2000 ^{o}C and flow rates of 50 SCFH (standard cubic feet per hour) of hydrogen and 100 SCFH of Ar. To obtain a uniform temperature profile along alumina tube, the furnace has 8 heating elements.

Process gas is mixed using manifold that controls the individual flow rate of each gas. After being mixed, the gasses flow through the tube and then exit through a burn-off-torch designed to combust hydrogen. It should also be noted that for purposes of safety, the entire furnace was placed in a fume hood.

Samples to be etched were placed on a carborundum plate at a place near the center of the hot zone in the alumina tube. Using a k-type thermocouple in a ceramic tube the temperature inside of the alumina has been correlated with the external thermocouple reading displayed on the on the furnace.

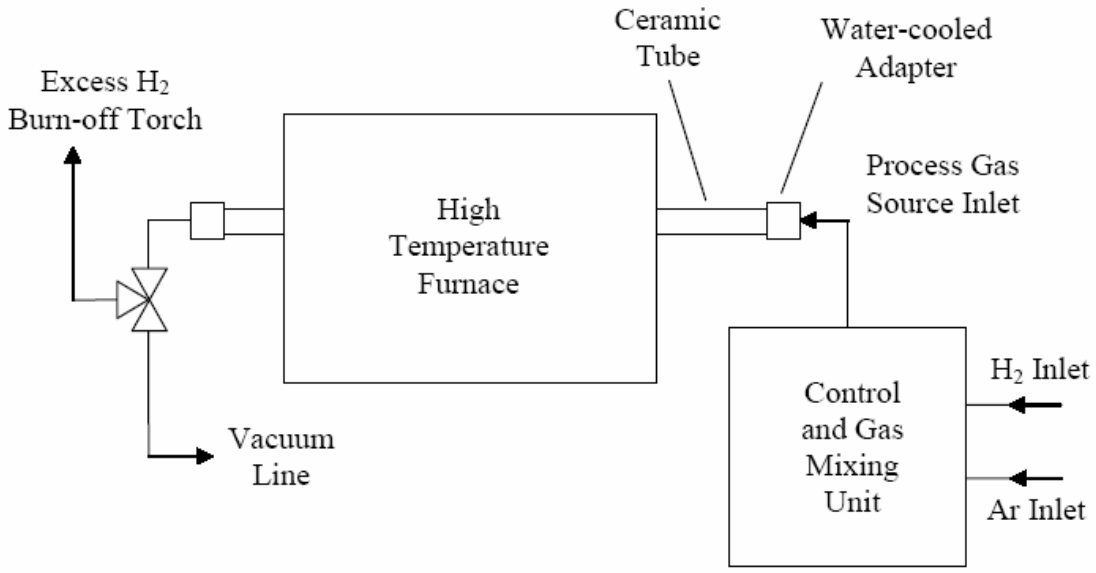

Figure 3.4. Schematic of the high temperature hydrogen furnace used for annealing SiC substrates.

The adapters on either end of the alumina tube are Swage-Loc fittings with water cooling jackets added by the Chemical Engineering Shop. These allowed for rapid and reproducible sealing of the tube. Using a rotary mechanical pump the alumina tube was evacuated to ~10^{-3} Torr (confirmed with a 0-100 Torr MKS Baratron pressure transducer). This ensures that little or no air, water vapor, or other contaminates are present before or after the hydrogen etching process. Moreover, this process ensures that there are no hydrogen/Ar leaks.

For all of the experiments, ultra high purity hydrogen was used as the reactant and ultra high purity Ar was used as the inert background gas. All gas lines were made of 316 stainless steel and pumped out to the mili-Torr range to ensure absence of leaks and to remove contaminants such as air and water vapor. For a more in-depth discussion of please refer to the work by Peng.

3.3 Analysis Techniques

To accurately study the interaction of the Pd with the SiC, several surface sensitive techniques were employed. These included Auger electron spectroscopy (AES) and Atomic force microscopy (AFM).

3.3.1 Auger Electron Spectroscopy (AES)

AES is an extremely surface sensitive technique that provides elemental and chemical information about a particular species present in a sample. This technique examines the energy spectrum of electrons produced by a non-radiative recombination process first observed by Pierre Auger.[55] Hence, electrons produced by this process are known as Auger electrons.

The key steps in the Auger emission process are illustrated in Figure 3.5. When excited by an incident (primary) electron beam, a core electron of an atom maybe removed, and the atom goes through a relaxation process where the core vacancy is filled by an electron from an outer shell. The energy lost by the electron filling the core vacancy, E_K-E_{L_1} in this case, can be accounted for by either the emission of a photon or the emission of an outer shell electron (the Auger electron). The kinetic energy of the

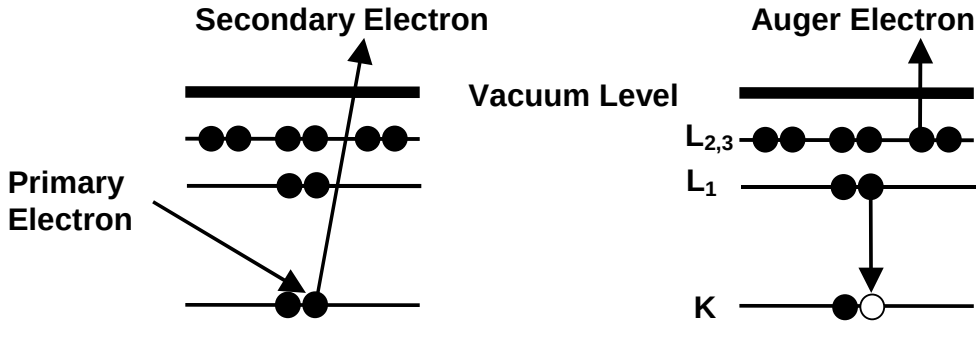

Figure 3.5. Auger electron emission process.

emitted electron, $E_{kinetic}$, given by Equation 3.1

$$E_{kinitic} = E_K - E_{L_1} - E_{L_{2,3}} \tag{3.1}$$

Consequently, the kinetic energy of the ejected electron reflects the identity of the atom from which it was ejected. Moreover, if the level from which the Auger electron was emitted is a valence level (involved in chemical binding) the Auger lineshape will also provide chemical information on the nature of the bond. Therefore, the peak positions and line shapes of the resulting energy spectrum are both of interest and carry useful information.

Figures 3.6 (a) and (b) display an AES spectrum of SiC. Figure 3.6 (a) show the N(E) spectra that is collected by the spectrometer and Figure 3.6 (b) displays the

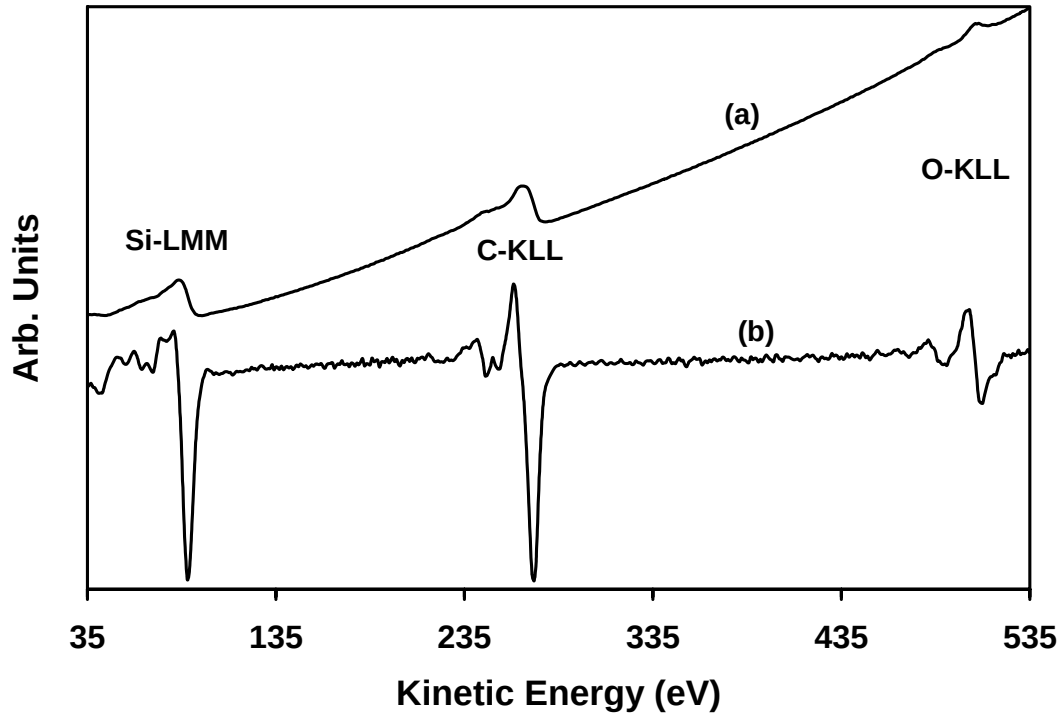

Figure 3.6. a) N(E) and b) dN/dE spectra of SiC.

derivative spectrum of the spectrum shown in (a). In both spectra clearly visible are the C-KLL, Si-LMM, and O-KLL peaks. Derivative spectra, as shown in Figure 3.6 (b), are commonly used because of the accentuated details of the line shape and elimination of the rising back ground which is due primarily to in-elastically scattered electrons.

3.3.1.1 Influence of Chemical States on AES Lineshapes

As mentioned above, AES line shapes contain chemical information. This dissertation uses this information to delineate how different atoms are chemically bound. The species of particular interest to these studies are C, Si, Pd, and Ni. The C-KLL and the Si-LMM peaks were used as the primary source of chemical information. C can be bound in one of three states: graphite, SiC and NiC_3. Si can be found in one of five states: elemental Si, SiO_x, SiC, Pd_xSi, and $NiSi_x$.

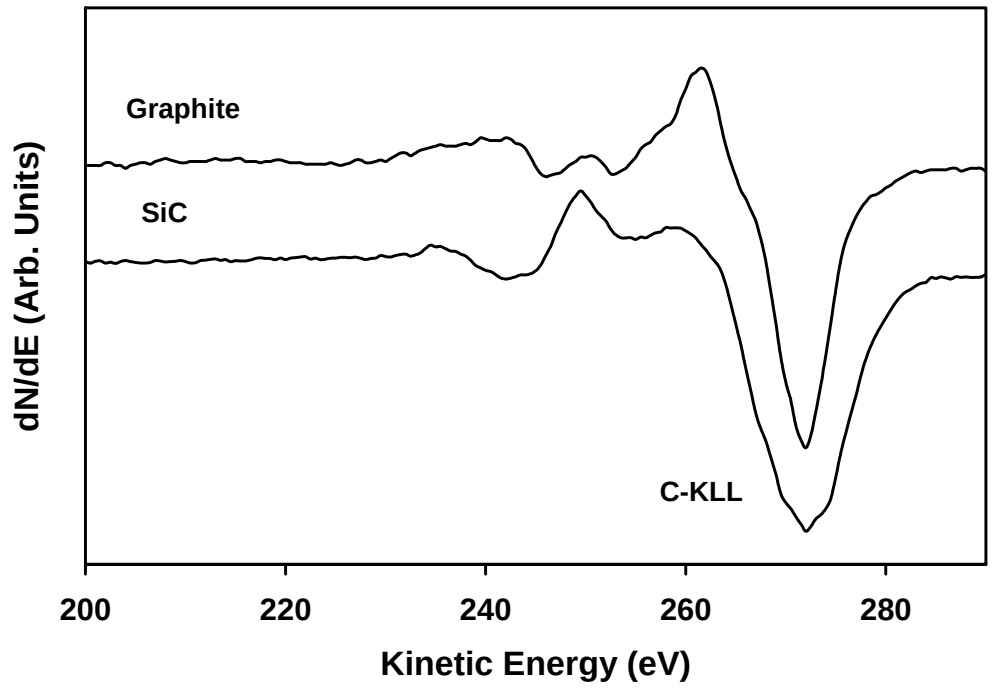

Figure 3.7. C-KLL spectra of graphite and SiC.

Previous studies in this lab have documented the changes in the C-KLL line shape for diamond, SiC, and graphite.[3,5,56,57] The C-KLL line shapes for SiC and graphite are illustrated in Figure 3.8. The C-KLL peak of C bound in SiC has three distinctive features. First, the lower wing of the C-KLL peak at 272 eV is relatively narrow with a shoulder at 266 eV, while the upper wing at 262 eV rises well above the base line. Second, there is an additional characteristic peak at 252 eV. Third, there is a well defined plasmon features at 245 eV. The sp^2 or graphite C-KLL spectrum, shown in Figure 3.7, reveals three distinctively different features. First, the C-KLL peak has a relatively broad lower wing at 272 eV, with a rounder upper wing at 259 eV. Second, there is characteristic feature at 250 eV that rises above the upper wing. Third, there is a plasmon feature at 242 eV.

Amoddeo *et al.*[58] performed a detailed study of C on crystalline Ni (111) surfaces. They documented, as shown in Figure 3.8, that when Ni forms a carbide, the C-KLL reflects this in three ways. First of all, the lower wing at 272 eV is a doublet with a very narrow upper wing at 265 eV that rises well above the background. Second there is a sharp peak at 259 eV. Third, is a sharp plasmon feature at 253 eV.

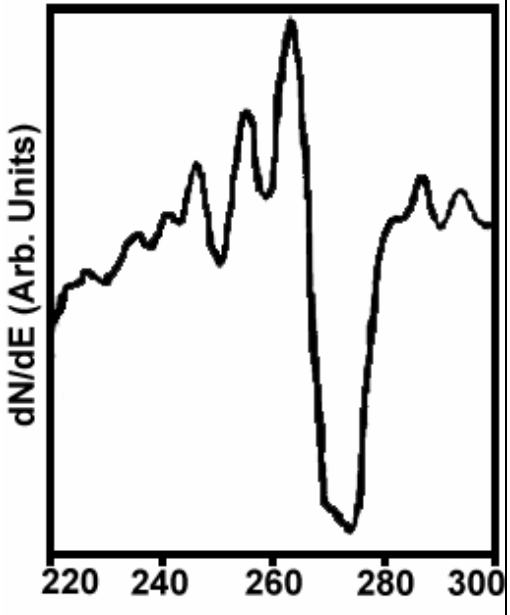

Figure 3.8. C-KLL spectrum for Ni carbide.

The Si-KLL line shape also gives information as to how the Si atoms are bound. Figure3.9 shows the spectra for elemental Si, SiC, Pd_xSi and SiO_x. The Si-LMM peak for

elemental Si and has a narrow sharp lower wing at 92 eV with a well defined upper wing at 84 eV. Compared to the elemental Si-LMM peak, the lower wing Si-LMM peak for SiC is noticeably broader and is shifted to 88 eV. Also the upper wing of the SiC Si-LMM spectra is shifted to 80 eV and is much less sharp. When Si is bound to oxygen the peak again is shifted to lower energies, broadens significantly, and two peaks emerge at 53 eV and 63 eV. In our experience these peaks begin to emerge at very lo oxygen levels. If the film is SiO_2 the lower wing will be located at 76 eV. Because the SiO_x Si-LMM peak in Figure 3.9 is at 83 eV, the spectra is representative of a $SiO_{x<2}$ composition.

Of the spectra shown in Figure 3.8, the Si-LMM spectrum for Pd_xSi is most unique. The set of five peaks (76 eV, 81 eV, 87 eV, 92 eV and 96 eV) appear when a Pd

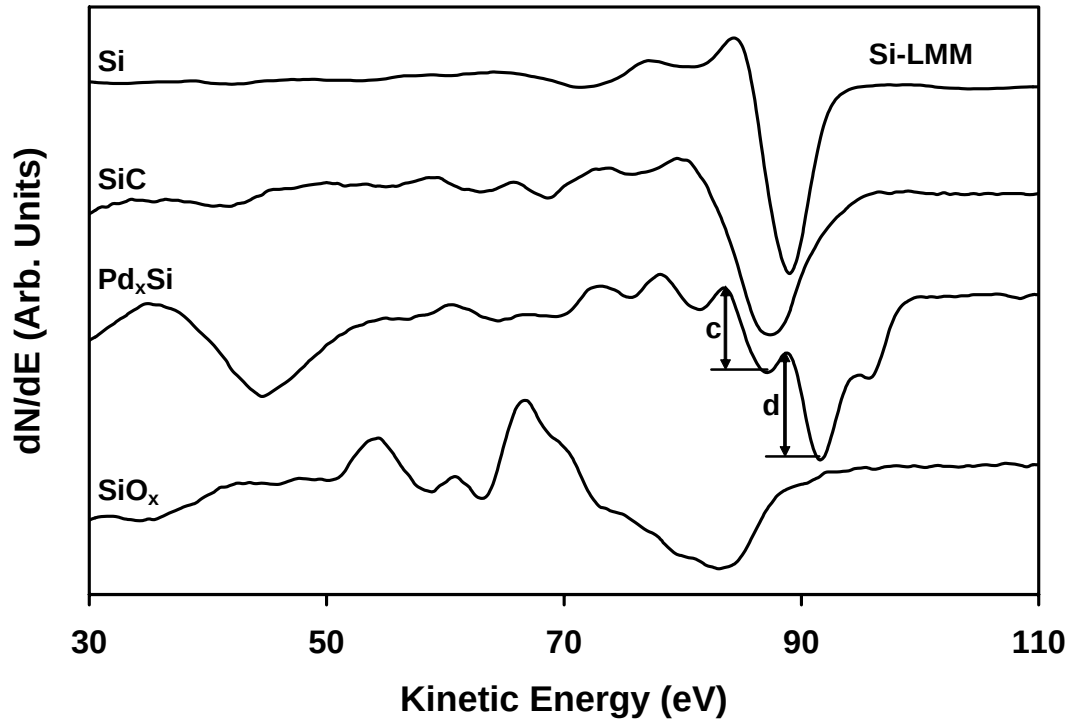

Figure 3.9. Si-LMM spectra of Si, SiC Pd_xSi, and SiO_x and SiC.

silicide is formed. Bermudez[38] demonstrated that the ratio of these peaks can be used to determine the stoichiometry of the silicide. Marked on the Pd_xSi spectrum in Figure 3.9 are peak-to-peak heights c and d. It is the ratio of these heights that is linked to the stoichiometry of the film as follows: c/d ~ 0.5 = Pd_2Si, c/d ~ 0.7 = Pd_3Si, c/d ~ 1.5. = Pd_4Si. Unfortunately, no such correlation is available in the literature for Ni silicides.

3.3.1.2 Quantification of AES

Besides chemical information, relative intensities of the AES peaks can also provide information on amount of a specific species present in the sampling volume. To obtain this information the total intensity of an elemental peak in an AES spectrum must be understood. This is achieved by examining the AES general intensity equation (3.2).

$$I_i = A \cdot I_p \cdot N_i \cdot \beta_i \cdot \Phi_i \cdot \Psi_i \cdot R \cdot T_i \cdot \lambda_i \cdot \cos\theta \tag{3.2}$$

Where:

I = intensity due to the i^{th} species

A = surface area analyzed

I_p = primary beam current

N_i = number density of atoms of i^{th} species producing the signal

β_i = backscattering factor for i^{th} specie

Φ_i = ionization cross section for i^{th} specie

Ψ_i = transition probability for i^{th} specie

R = surface roughness factor

T_i = instrument transmission factor for the i^{th} specie

λ_i = mean free path of the i^{th} specie

θ = angle of incident beam from sample normal

As is seen in equation (3.2) the Intensity of the signal depends on the analyzer, the concentration of elemental species involved, and the physics of the electron generation, and emission process. The dependence of the signal intensity on N_i can be used to gain information about the relative percentages of elemental species present on a surface. While using the same instrument with the same beam current settings instrument dependant variables that are not associated with a particular elemental species can be considered constant and their subscripts can be dropped (e.g.. $A_i=A_k$, $I_{pi}=I_{pk}$ and $\theta_i=\theta_k$). Since θ, λ, Ψ, B, and T are a combination of element[59] and detector dependant[39] factors we can write them into one experimentally determined quantity know as the sensitivity factor S The placement of the elemental species (depth form the surface) is taken into account by the in elastic mean free path (IMFP) or λ_i which will be discussed in a Section 3.3.1.3. It should be noted that λ also is taken into account in S.

$$S_i = \lambda_i \cdot \Phi_i \cdot \Psi_i \cdot T_i \cdot B_i \tag{3.3}$$

Also note that the surface roughness factor R is dropped. Surface roughness can play a major role in the AES peak intensity.[39] Studies have shown that if the surface area doubles the AES intensity is cut by 30 % or greater.[60,61] However, the roughness of the surfaces considered in this dissertation are relatively smooth (RMS roughness of < 15 nm), and therefore changes in surface area are relatively small (< 4 %). Therefore, surface roughness is not likely to play a role in AES peak intensities.

This results in a reduced general intensity Equation 3.4.

$$I_i = N_i \cdot S_i \cdot A \cdot I \cdot \cos\theta \tag{3.4}$$

Solving 3.4 for N_i

$$N_i = \frac{I_i}{S_i \cdot A \cdot I \cdot \cos\theta} \tag{3.6}$$

At this point the concentration of a particular species *Xi* can be determined.

$$X_i = \frac{N_i}{\sum_{k=1}^{n} N_k} = \frac{I_i/(S_i \cdot A \cdot I \cdot \cos\theta)}{\sum_{k=1}^{n} I_k/(S_k \cdot A \cdot I \cdot \cos\theta)} = \frac{I_i/S_i}{\sum_{k=1}^{n} I_k/S_k} \tag{3.5}$$

Equation 3.5 with experimentally determined sensitivity factors S (Si/C = 1.06) is used to determine the stoichiometry of SiC surfaces detailed in Chapter 4. Work done by Ziemer in this determined that the error in measured AES intensities to be +/- 3.6 % and 5.1 % in normalized intensities.

3.3.1.3 Mean Free Path

AES is a particularly surface sensitive technique. This sensitivity is due to rather short inelastic mean free path (IMFP) or λ for Auger electrons. The IMFP is a measure of how far an average electron travels before it undergoes an inelastic collision. The two greatest influences on the IMFP are the kinetic energy of the electron and the medium through which the electron is traveling. Figure 3.10 shows the probability of an electron escaping the surface without being inelastically scattered, verses the ratio of the sampling depth/IMFP. When the sampling depth becomes greater than 4 times the IMFP the probability of the electron escaping the surface without under going an inelastic collision

is less than 2%. Therefore, 98 % of the electrons, that contribute to the intensity of a given AES peak, originate less than 4 IMFPs from the surface.

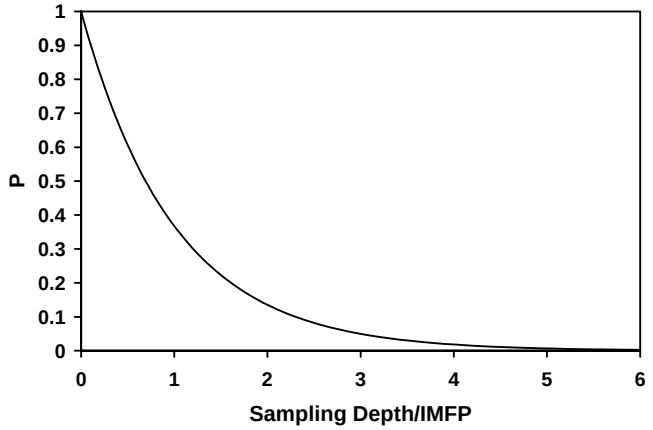

Figure 3.10. Probability of an electron undergoing an inelastic collision vs. sampling depth/IMFP(λ).

IMFPs also depend on the kinetic energy of the electron. IMFPs has been shown to have a minimum value for electrons with a kinetic energy of about 100 eV.[62,63] Further analysis by Seah and Dench[64] showed that IMFPs of inorganic compounds can be described by Equation 3.6, where *a* is the thickness of a monolayer and E is the kinetic energy of the electron.

$$\lambda_m = \frac{2170}{E^2} + 0.72 \cdot (a \cdot E)^{1/2} \tag{3.6}$$

Ballard[65] later noted that for inorganic solids improvements can be made in Seah and Dench's formula by including more information about the electron-impact ionization cross-section. Mean free paths used in this dissertation to describe the stoichiometry of SiC surfaces prior to metal deposition were obtained from the NIST Electron Inelastic-Mean-Free-Path Database published in December 2000.[66]

3.3.2 Atomic Force Microscopy (AFM)

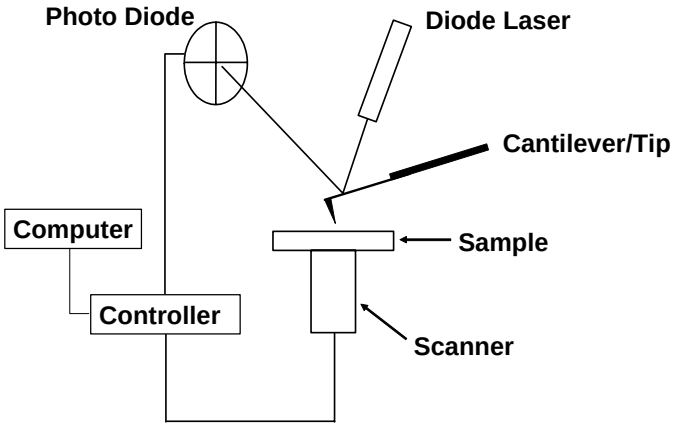

Figure 3.11. Schematic of the fundamental components of an AFM.

Atomic force microscopy (AFM) was used to gain morphology data of the surfaces. AFM analysis provides not only detailed images of surface morphology but also 3 dimensional measurements of surface features. AFMs have angstrom level sensitivity to out of plane or height measurement, and lateral resolution on the order ~2 nm.[67]

All AFMs are made up of six basic components. These include a Laser, AFM tip/cantilever, photodiode (PD), computer, controller, and scanner. Though there are several ways to configure these basic components, a common configuration found in several AFMs including the one used for this dissertation is shown in Figure 3.11.

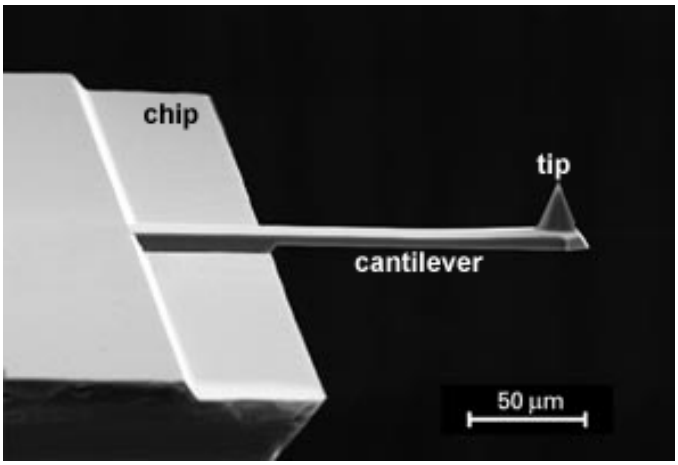

Figure 3.12. Image of a AFM chip, cantilever and tip.[68]

One of the most important components of the AFM is the tip show in Figure 3.12. The tip is the physical interface between the instrument and the sample. Tips are general silicon and made by e-beam lithography.

Each tip is connected to wide piece of silicon know as the cantilever. The cantilever then in turn attached to an even larger piece of silicon known as the chip. Tips come in a variety of shapes and dimensions. For this set of experiments, conical shaped silicon tips with a nitride coating (to reduce surface-tip interactions) were used. The radius of curvature of the end of the tips was less than 20 nm. Like tips, cantilevers come in variety of different shapes and sizes. For these experiments cantilevers shaped like diving boards were used as shown in Figure 3.12.

The second most important part of the device is the scanner. The scanner is either employed to move the tip across the sample or move the sample under the tip depending on the configuration of the system. The most common scanner, and used in this set of experiments, is the piezo-electric tube scanners which moves the sample under the tip. Voltage is applied across the tube forcing the tube to bend. Voltages are applied in orthogonal directions to create a rastering and up and down motion. A couple of difficulties arise for the design of the scanner. First, because the motion of the end of the scanner is an arc there are nonlinearities that enter into the data collection especially with large area (>5μm) scans. Second, the piezo-electric response is non-linear to the voltage applied and hence can cause bending or stretching of the outer edges of images during large area scans (>10 nm). This nonlinearity is dealt with in the image/data manipulation software by fitting a nonlinear curve (of a selected order) to the data and then subtracts that curve to flatten the image. Special care should be taken not to over-fit the curve to the surface as fitting can also result in the loss or creation of features in the data. A red diode laser and photo detector used to track the movements of the cantilever. A solid state controller is used to move the scanner and maintain the feed back loop (to be

described shortly). Finally, a computer is used to both collect the data and give input to the controller.

An AFM works by moving the tip over the surface. While the tip is scanning over the surface the tip's interactions with the surface affect the motion of the cantilever. Using the laser light reflected off of the back side of the cantilever, the photodiode collects data on the deflection of the cantilever. This data is used in two different ways: as input for a feed back loop which maintains a constant tip-to-sample force by altering the vertical position (constant force mode) or to directly create a map of the morphology of the surface (constant height mode). Without an active feed back loop constant height mode has the advantage of reduced noise, but because of limited flex in the cantilever sample roughness must be less than ~2 nm. Constant force mode has more inherent noise in the system due to the feed back loop, but because the piezo-electric scanner can move in the vertical direction (~700 nm) the risk for running the tip into the sample is greatly reduced. Data taken by AFM in this dissertation was done in constant force mode.

There are several ways the tip can be employed to reveal information about the

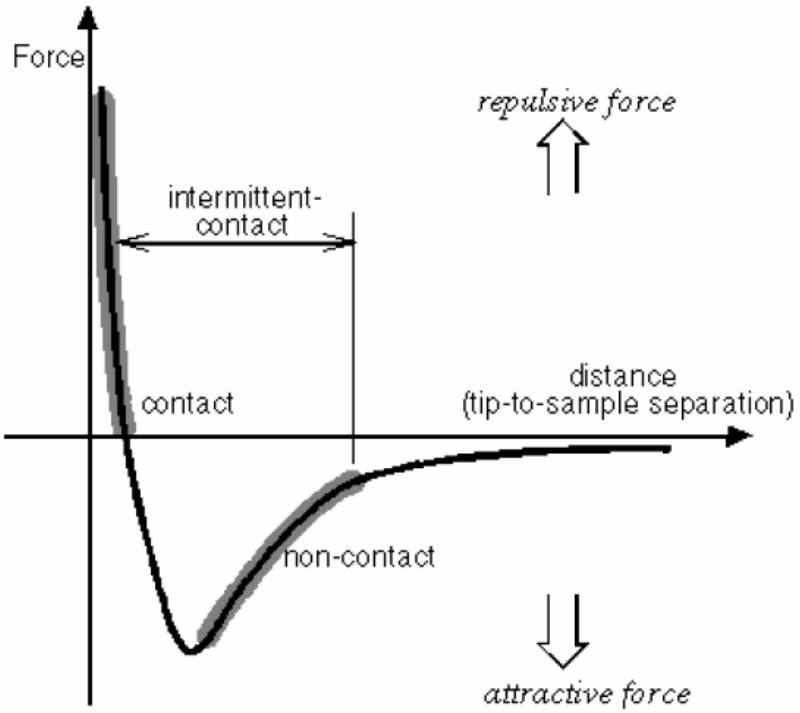

Figure 3.13. Illustration of the van der Wall's force curve.[69]

sample surface and, in some cases, subsurface features. The most common method is known as contact mode. In contact mode the tip is brought so close to the surface that it is repelled by the surface as described by van der Wall's forces (Figure 3.13). In this mode of operation the motion of the cantilever directly reflects the contours of the sample surface. The second most common mode of operation is known by many different names, but for the sake of simplicity and to avoid any legal implications I will refer to the mode as acoustic (AC) mode. In AC mode the cantilever is forced into an oscillation at a known frequency. The tip is then brought close to the surface so the oscillations of the cantilever are affected by the van der Wall's force. Depending on the oscillation of the

cantilever and device settings the tip may or may not be making intermittent contact with the surface.[70] The controller then uses the change in amplitude either as information in the feed back loop or as raw data. The advantage of AC mode over contact mode is that there is a reduced tip to sample force therefore making the technique less destructive and more sensitive to the sample surface. The down side to the technique is the added noise sent into the system due to the motion of the cantilever. For these sets of experiments AC mode was used.

3.3.2.1 AFM Error Analysis

The AFM was calibrated using a combination of height and lateral standards. For height calibration a 20 nm +/- 1.0nm height standard (TGZ01) produced by Mikro Mash was used. Device noise, at most, contributed a totals f 0.05 nm of uncertainty to height measurements, making the total uncertainty in calibration +/-1.05 nm. Lateral calibration was accomplished using a standard with a grid of cones with a 1 μm +/- 0.05 μm periodicity produced by Veeco Instruments.[71] Lateral noise of the device was determined to be much less than 0.05 nm and therefore is not considered. Height and lateral positions of an AFM are derived from a known relationship between voltage applied to the piezo-electric scanner and the displacement of the tip. For lateral motion this is a polynomial with a linear and non linear term while for height motions the relationship is purely linear. Since, in both cases, the linear term controls the distance measured by the system, the uncertainty becomes a function of the size of the measurement. Therefore, both height and lateral measurements are +/-5 %. The lateral standard was also used to check the tip for asymmetries that lead to image artifacts. Also, rotated scans were taken of features to determine if features were real or artifacts of the tip.

3.4 Experimental Procedures

The experiments were run using 3.5^{o} off axis 6H-SiC from CREE Inc. and on axis 6H-SiC from Dow Corning (formerly Sterling Semiconductors). The 1"-2" 6H-SiC wafers were cut into 1x1 cm^2 squares as shown in Figure 3.14. After being diced, half of the samples were put through one of two surface preparation procedures described in Section 3.4.1.

Next the surface morphology was determined using AFM analysis. After AFM analysis is performed the sample is then put through the degreasing procedure and hydrofluoric (HF) acid dip before the hydrogen etching step. AFM analysis has confirmed that the chemical etching does not affect the surface morphology. After a

Figure 3.14. Image of a diced and un-diced CREE Inc. 1" 6H-SiC wafer.

repeat of the initial chemical treatment the sample is mounted on a molybdenum sample puck and introduced into the system. For samples that will have thick films (>45 nm) deposited, a stainless steel grid is placed to create a shadow mask make millimeter sized squares necessary for current-voltage (IV) analysis.

After being introduced into the growth system, AES analysis is run to check the surface composition of the sample. The sample is then transferred to the growth chamber manipulator and the sample is annealed while optical pyrometer readings and back face temperatures are taken so that a correlation between back-face and front-face temperatures can be made. After this anneal the sample is transferred back to the analysis chamber to ensure that the surface composition has not changed.

Next, the sample is transferred back to the growth chamber. The manipulator is set to a known position, and the effusion cell is set to a temperature at which the deposition rate has been determined. At this point a Molybdenum shutter covering the effusion cell is opened to deposit the metal film. After deposition the sample is transferred for post deposition AES analysis.

Now, the sample is transferred back to the growth chamber manipulator to be annealed. At this point the front-face/back-face temperature correlation is employed to determine the necessary back face temperature to obtain the desired front face temperature. From this point on, the emissivity of the sample is not known so the optical pyrometer can only be used to determine if the face has come to a thermal equilibrium. After annealing, the sample is cooled to 100 ^{o}C or less, transferred and a final AES analysis is performed. After the AES analysis is completed, the sample is removed from the system and AFM analysis is performed.

3.4.1 Surface Preparation

Surface preparation is necessary for three main reasons. First, after the SiC wafer is diced a layer of particulate and other contaminates are left on the surface. Second SiC, like Si, has a natural oxide that must be removed and the surface passivated. Third, samples that come from the vendor are mechanically polished and have scratches that are as deep as 20 nm and as wide as 250 nm wide. These scratches are known to be associated with sub-surface damage. Part of this study is to determine the effects of the surface and sub-surface damage caused by the polishing, by comparing the interactions to those on an ordered surface. A high temperature hydrogen etching or annealing process is employed to create an atomically stepped surface.

3.4.1.1 Preparation of the Standard Surface

This procedure produces what is referred to as the *standard surface* since it is representative of those presently used in device fabrication, as previously discussed. First the surface is degreased using a combination of chemical and mechanical means as listed below. Note, this procedure is done at room temperature, is know as the *degreasing procedure* or *degrease*.

1. 5 minutes in tetrachloraethelene (TCE)
2. 5 minutes in TCE
3. 2 minutes in acetone
4. 5 minutes in methanol
5. 5 minutes in methanol
6. Blow dry with ultra high purity (UHP) argon.
7. Clean surface vigorously with acetic acid on a q-tip

8. Clean surface vigorously with methanol on a q-tip

9. Blow-dry with UHP nitrogen

The next, and final step in the pretreatment of the standard surface, is to remove the oxide layer using a buffered HF solution. This step, known as the *HF dip*, outlined below, was developed from the Modified Fenner Etch (MFE) used for silicon as studied by L.H. Hirch[72].

1. Degrease

2. Rinse with De-ionized H_2O for 5 minutes

3. Submerge in 10:1 De-ionized H_2O /reagent alcohol: HF for 10 minutes

4. Rinse with reagent grade alcohol for 5-10 seconds

5. Blow dry with UHP nitrogen

6. Optically inspected for water marks and particulate

It should be noted the HF comes from the supplier cut 1:1 with de-ionized H_2O. The rest of the dilution is done with reagent alcohol (HPLC grade), which consists of ethyl, methyl and iso-propanol alcohols.

3.4.1.2 Preparation of Stepped Surfaces

To remove surface and sub surface polishing damage, the SiC samples were etched in hydrogen at 1600 ^{o}C. This process leaves the surface with atomically flat terraces 50-200 nm wide with steps heights on the order of one 6H-SiC unit cell high (1.5 nm). This surface will henceforth be referred to as the *stepped surface*.

After dicing, the samples are degreased and HF dipped as described in the standard surface preparation section. Then the sample was placed on a carborundum holder in a predetermined position in the hydrogen furnace. The furnace is then

evacuated to ~10^3 Torr and then UHP Ar is flowed through the furnace at a rate of 8 SCFH. The furnace is ramped at 400 ^oC/hour to 1000 ^oC and then 300 ^oC/hour to 1600 ^oC and immediately back down in the reverse order. Ramp rates were dictated by safety of the alumina and stress on the heating filaments. Hydrogen is introduced at 1000 ^oC and constitutes 5% of the entire flow. After hydrogen etching is concluded the sample is removed and AFM is performed to check the morphology of the surface. The final step is a repeat of the degreasing and HF dip procedure used prior to the hydrogen etch. For information on this process please read the work by Peng.

3.4.2 Deposition of Metals

Deposition of the metals was carried out using the VEECO/EPI high temperature effusion cell (EPI-10-HT) displayed in Figure 3.2. The metals were placed in a W crucible with a 10 cc BeO liner that had been out gassed at 1500 ^oC under UHV. The purity of the elemental Pd and Ni were 99.99 % and 99.999 % respectively. A Mo shutter over the end of the effusion cell was used to control the length of the deposition process.

There are two key parameters that influence the deposition rate. These are sample position and effusion cell temperature. Equation 3.7 describes the flux (J) from the effusion cell.

$$J = \frac{(dM/dt)\cos^2\theta}{\pi r^2} \tag{3.7}$$

Here dM/dt is the rate (mass/time) at which material is leaving the cell, θ is the polar angle to the point at which the flux is being evaluated and r is the distance from the cell to the evaluation point on the substrate. Since flux from the Knudsen cell has a $\cos^2\theta$

dependence of the polar angle and a $1/r^2$ dependence, repositioning of the sample accurately with in the chamber is important to be able to recreate deposition rates. Therefore the sample was always set to the same position for deposition. Also, the lateral dimensions of the samples used in these experiments were small compared to *r*, therefore the $\Delta\theta$ (sample center to sample edge) is approximately 0. This means the variation of flux over the sample surface is negligible. The second critical factor in reproducing deposition rates in the temperature of the effusion cell since this is a key factor in determining *dM/dt.*

Temperature is the main control over vapor pressure of the metal which in turn regulates the mass-flux-rate, Γ, generated by the cell. This generally is expressed by Equation 3.8.

$$\Gamma = C \exp\left(-\frac{\Delta H_{evap}}{T} \right) / \sqrt{T} \tag{3.8}$$

ΔH_{evap} is the latent heat of evaporation of the material *C* is material dependent constant and *T* is the temperature of the cell. Since $dM/dt = A*\Gamma$ (where *A* is the surface area of the cell), equation 3.11 demonstrates the dependence of the flux at the sample on the temperature of the effusion cell.

For these experiments, deposition rates were determined by mass gain at a single sample position and selected effusion cell temperatures. These same conditions were used to carry out all of the depositions. Error in the deposition rates and subsequently the thicknesses of the films was determined to be 15 % of the predicted thickness.

3.4.3 Annealing of the Samples

Annealing the samples was done by radiative heating via a Ta wire wound heater mounted behind the sample puck, as described by in detail by Ziemer. A spring loaded thermocouple touching the back of the puck was used to monitor the heating of the puck. However, due to the nature of the experiments, it was not possible to use a binding agent to increase thermal conductivity between the puck and the sample.

Using an optical pyrometer and an experimentally determined emissivity for SiC (documented by Peng[3] and confirmed in the literature) temperature differences between the thermocouple and front face of the sample was determined to be as great as 200 ^{o}C, and varied sample to sample. Unfortunately, the emissivity of the annealed metal films was impossible to predict, making the use of the optical pyrometer for determining front face temperatures impossible. Therefore, the samples were annealed prior to deposition, and temperature curves correlating thermocouple temperature to the front face temperature of the sample were created. The correlation curves were used to determine the thermocouple temperature that corresponds to the desired sample temperature.

During the annealing process the thermocouple used to determine absolute temperature using the correlation curve, mentioned above, while the optical pyrometer was used to determine when the surface of the sample has reached an equilibrium temperature. All samples were cooled temperatures less than 100 ^{o}C before being transferred to the analysis chamber for annealing.

3.4.3.1 Calibration of the Optical Pyrometer

The optical pyrometer was calibrated using a CI systems high temperature black body source with an accuracy of +/- 3.0 ^{o}C, with an emissivity of 0.99 +/-0.01, located at

the U.S. DOE NETL facility located Morgantown, WV. After calibrating, data was taken and without a UHV window in between the optical pyrometer and the black body source. A curve relating the temperature difference, between the optical pyrometer readings and the black body temperature, was constructed (Figure 3.15). This calibration curve was used to eliminate temperature inaccuracies due to losses caused by the window on the UHV chamber. Based upon factory specifications of the optical pyrometer and the black

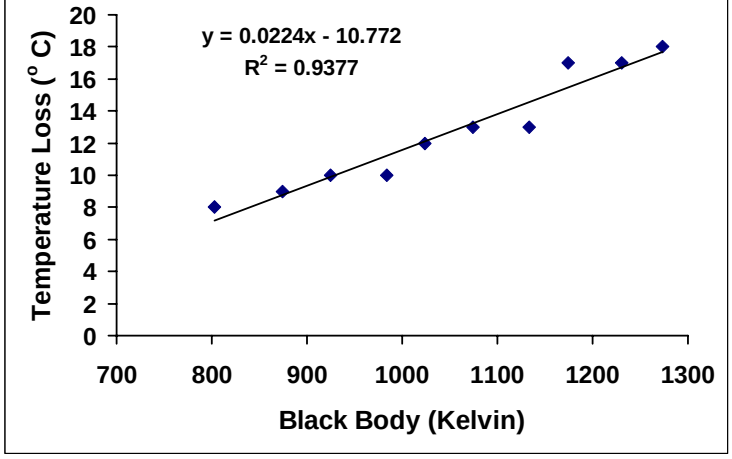

Figure 3.15. Calibration curve used to correct the optical pyrometer's temperature readings due to optical losses caused by the UHV window in between the sample and the pyrometer. Temperature loss is the difference between the known temperature of the black body source and the optical pyrometer reading.

body source temperatures, error in temperature readings was +/- 3.0 ^{o}C or +/- 1% of the temperature read by the optical pyrometer (whichever is greater).

CHAPTER 4: RESULTS AND DISCUSSION

The experiments outlined in Chapter 3 arise from the idea that chemical and structural state of the initial (pre-deposition of metals) surface have a strong effect on the interactions of metals with α-SiC. Specifically, the experiments focuses on two distinctly different α-SiC surfaces, referred to as *stepped* and *standard*. The physical and chemical differences between these surfaces will be examined in section 4.1. Next, the interactions of Pd with stepped and standard surfaces will be considered in section 4.2. To help understand the interactions of Pd with SiC (primarily the formation of silicides), the results of a study of Pd interactions with Pd-hydrogen terminated Si (100) 1x1 are discussed first. The last section 4.3 deals with the interactions of Ni with both stepped and standard surfaces. As for Pd, the results of a study of Ni-Si interactions are also discussed.

4.1 Surface Preparation of 6H-SiC

The two surface preparation methods discussed in Chapter 3 produce chemically and physically different surfaces. In this section, the chemical and physical changes in the surface produced by each step in these surface preparation methods will be discussed. For the remainder of this chapter and Chapter 5, the surface produced by the method described in section 3.4.1.1 will be known as the ***standard surface*** and the surface produced by the procedure described in section 3.4.1.2 will be known as the ***stepped surface***.

As mentioned in Chapter 2, the polishing of wafers (after being cut from the boule) leaves the surface in a wide variety of irregular states. Based on the RMS roughness measurements, the roughest and smoothest observed standard surfaces are illustrated in Figure 4.1.

The roughest sample surface shown in Figure 4.1 (a), representative of CREE samples, has scratches as large as 20 nm deep and 500 nm across with an over all RMS roughness of 2.2 nm. At the other end of the spectrum, the smoothest surface, shown in Figure 4.1 (b) representative of the Dow Corning/Sterling semiconductor samples, has small irregular bumps with an overall RMS roughness of 0.5 nm. Even though this surface seems much less rough it is still irregular.

Hydrogen etching eliminates much of the damage caused by polishing. Figure 4.2 illustrates a stepped surface for both a 3.5^{o} off axis wafer (a) and an on axis (b). When etched, the on axis wafers produce terraces 100-300 nm wide with step heights of 1.0-1.5 nm. The RMS roughness on the terraces is approximately 0.2 nm (Figure 4.2 b). Hydrogen etching also uncovers other crystallographic defects. Although it is not pictured, long trench-like defects are seen running parallel, perpendicular, 30^{o} and 60^{o} to the step edges. The depth of the trench tends to be an integer number of the step height, and their width varies, but it is not usually more than one third of the step width. It is not known what crystallographic feature or defect causes these trenches.

Off-axis samples produce much narrower, less well-ordered steps shown in Figure 4.2 (a). These steps have terrace widths of 27-41 nm and step heights of 0.35 nm-1.32 nm. The overall RMS roughness of the surface is 0.4 nm while the terraces have an RMS roughness of 0.2 nm This is an improvement over the 2.2 nm RMS roughness of standard

surfaces observed on other samples from the same wafer. Like the on-axis sample, some crystal defects were seen after hydrogen etching. Breaks in the terraces were observed to almost always run perpendicular to the step, be one terrace width and have a depth of one step. It is not known what crystallographic feature causes these breaks.

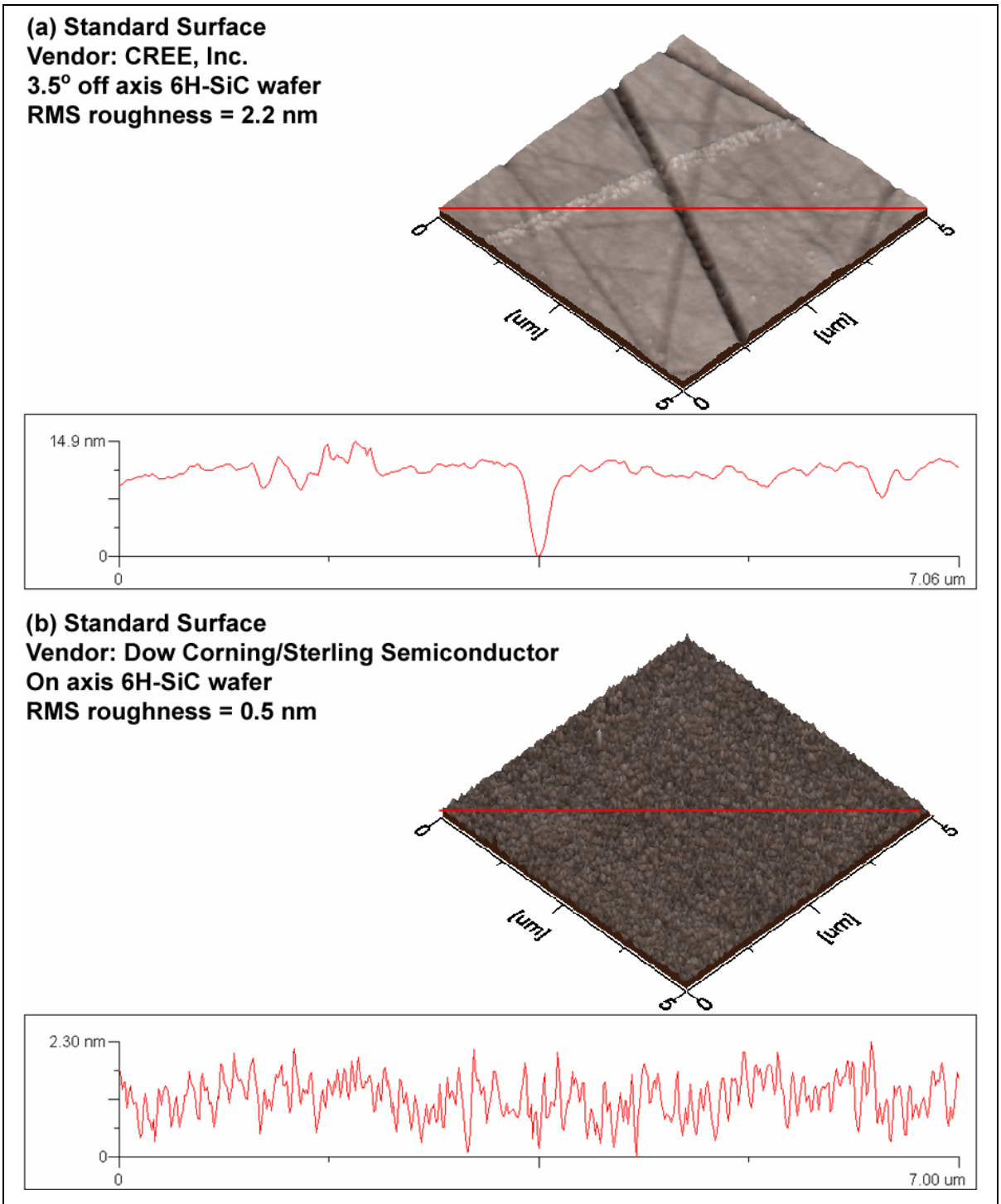

Figure 4.1. AFM images showing the roughest (a) and smoothest (b) standard surfaces. The insets are line profiles taken along the red lines on the 3D plots.

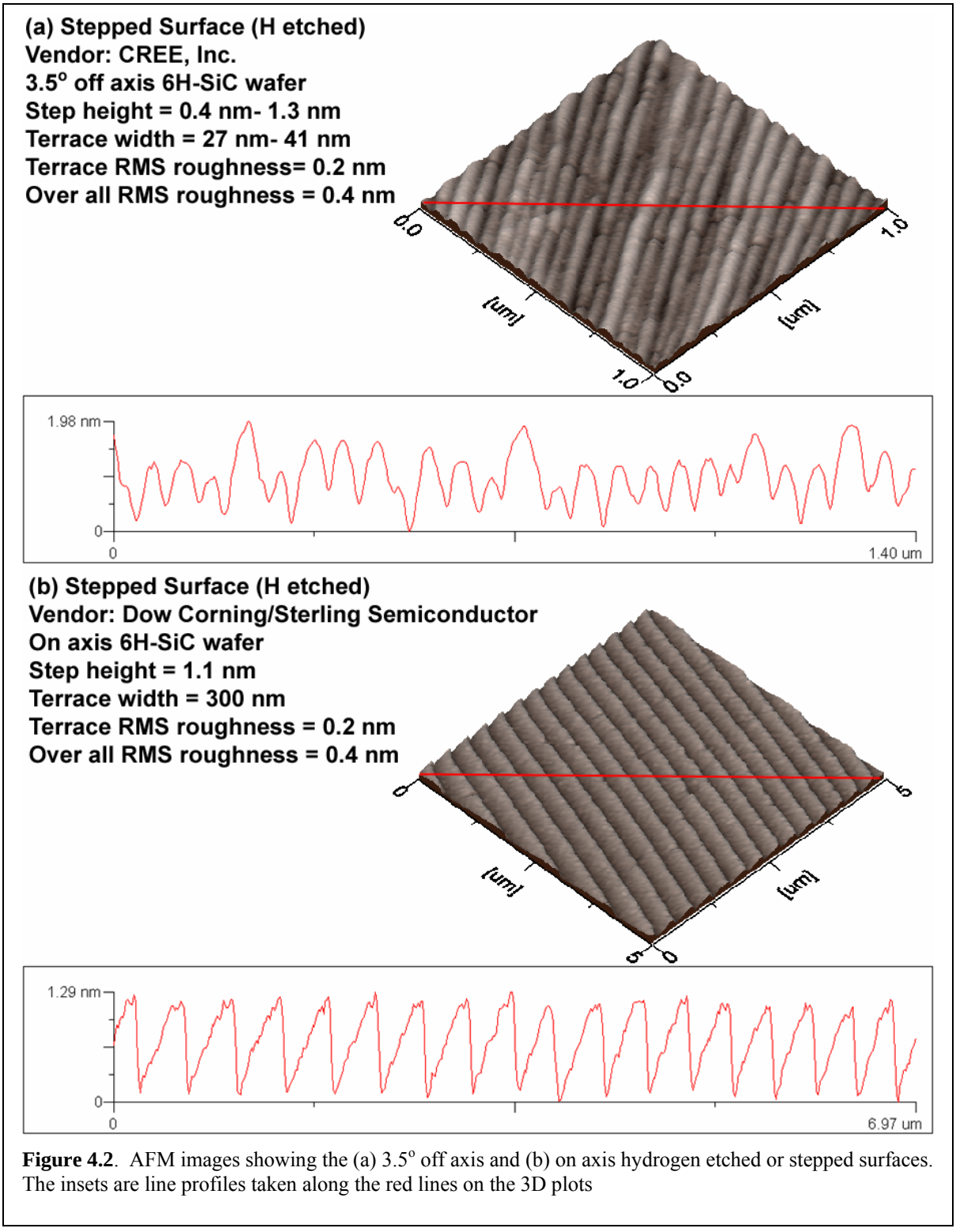

Figure 4.2. AFM images showing the (a) 3.5° off axis and (b) on axis hydrogen etched or stepped surfaces. The insets are line profiles taken along the red lines on the 3D plots

Not only are the physical characteristics of the surface changed by the hydrogen etching, but also the chemical properties were changed as well. Figure 4.3 gives an overview of how the AES intensities of O, C, and Si change with the different processing

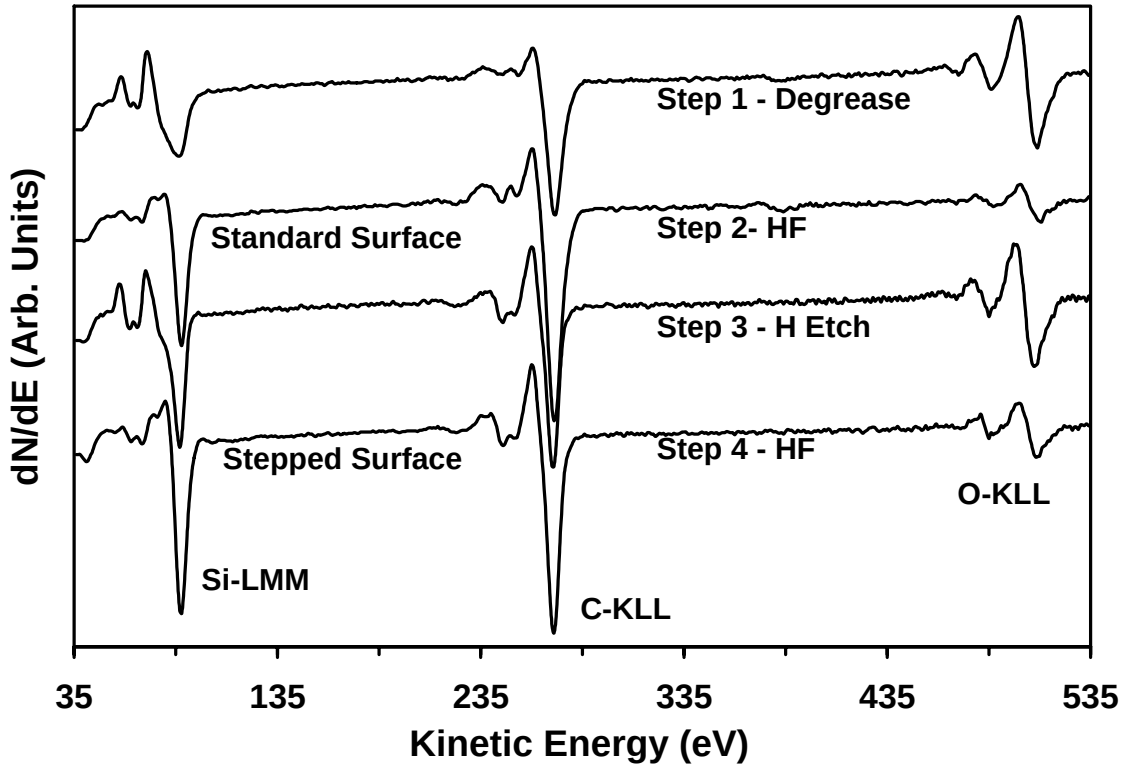

Figure 4.3. AES spectra illustrating the chemical changes of SiC for each of the surface preparation steps.

steps. When wafers arrive from the vendor they have a thin layer of oxide on them. After the initial degreasing (Step 1) to remove C contaminates, a strong O-KLL peak is present, but after an initial HF dip (Step 2), the intensity of the peak is reduced but not eliminated. The O-KLL peak increases to nearly that in step 1 after the hydrogen etching (Step 3) which is indicative of a new oxide layer on the sample. A final HF dip (Step 4) is used to remove as much of this oxide as possible. Note that not all of the oxide is

removed from either the stepped or standard surfaces. This is not addressed in any of the literature concerning standard surfaces. Future studies are planned to explore the complete removal of the remaining oxide on the stepped surfaces using atomic hydrogen etching under UHV conditions.

Figure 4.4 shows Si-LMM spectra for each of the steps in the cleaning process. These spectra reveal a change in the chemical state of Si after the each step. After the

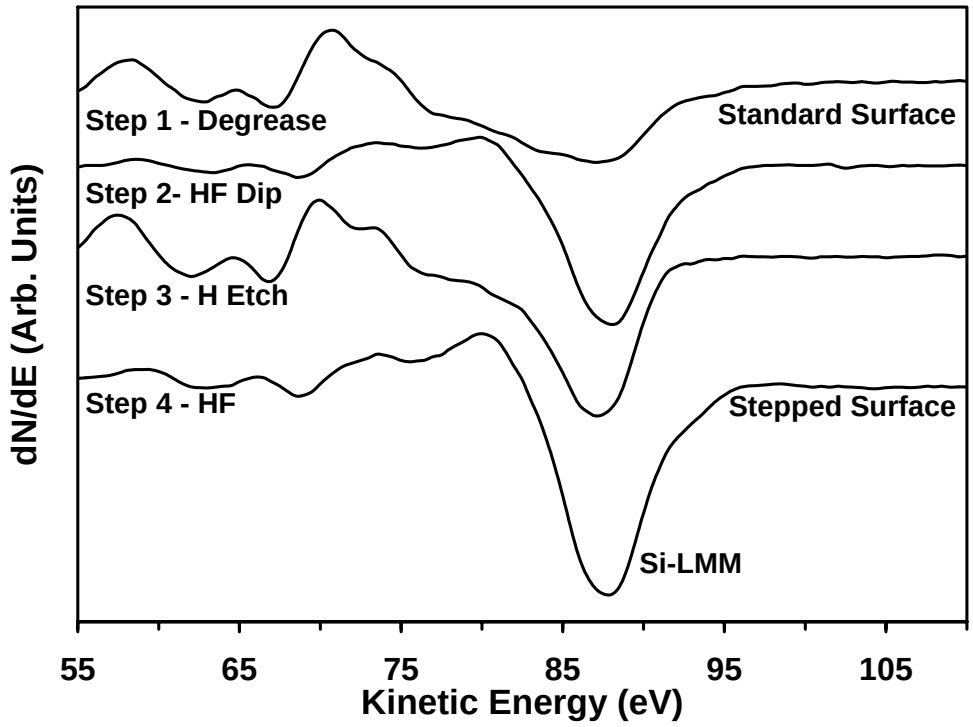

Figure 4.4. Si-LMM spectra illustrating the chemical changes of SiC during Surface preparation.

degreasing process (Step 1 in Figure 4.4) the lower wing of the Si-LMM peak at 88 eV is very broad and there are relatively strong features at 67 eV and 62 eV. This lineshape is indicative of a SiO_x film.[73] After the initial HF dip (Step 2 in Figure 4.4) the lower wing of the Si-LMM is greatly sharpened and the peaks at 67 eV, and 62 eV are reduced in intensity. This lineshape is close to that expected for SiC. After the hydrogen etching

process (Step 3 in Figure 4.4) the lower Si-LMM wing is, again, broadened and there is a re-emergence of the peaks at 62 eV, and 67 eV. This line shape is a convolution of SiO_x–Si and SiC-Si. After the hydrogen etched surface is HF dipped (Step 4 in Figure 4.4) the oxide is again removed and the Si-LMM lineshape is that of SiC-Si.

Absolute standards are difficult to establish, however, using a several simplifying assumptions, crude approximations of the oxide thickness of each step can be made. In general, if I_0 is the peak-to-peak intensity of an AES peak representative of the bulk material, and I is the corresponding intensity attenuated by an overlayer (e.g. an oxide) of thickness t then

$$\frac{I}{I_0} = e^{-t/\lambda} \tag{4.1}$$

where λ is the IMFP (as discussed in 3.3.1.3) for electrons of that AES peak. If the C-KLL intensity in Step 2 (Figure 4.5) is taken as I_0 (this neglects the very thin O overlayer on this surface), the intensity of the C-KLL in Step 1 (Figure 4.5) as I, and then λ = 0.91 nm, the thickness of the oxide in layer in Step 1 is 0.47 nm. Assuming a nominal Si-O bi-layer thickness ~0.23 nm (the C-Si bi-layer is ~ 0.23 nm) the oxide overlayer on the degreased surface corresponds to two Si-O bi-layers. Similarly, the thickness of the oxide layer in Step 3 (Figure 4.4) is 0.22 nm or about one bi-layer or approximately one monolayer of oxygen. Similarly, the oxide thickness for step 4 is 0.03 nm or less than one monolayer. This, of course, is probably pushing the of the continuum model which Equation 4.1 is based, but it does give a semi-quantitative sense of how thick the oxide layers are.

As with the Si-LMM spectra, the C-KLL spectra, shown in Figure 4.5, undergo some significant changes. The lineshape for Step 4, in Figure 4.5, is essentially that

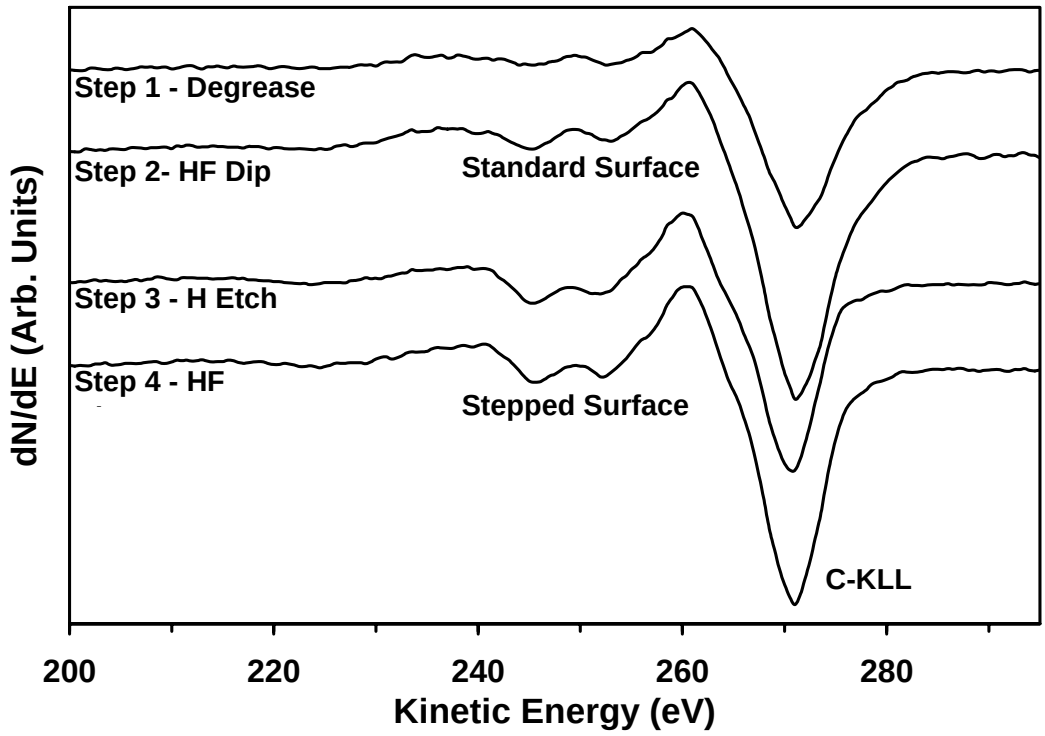

Figure 4.5 C-KLL spectra illustrating the chemical changes of SiC during Surface preparation.

expected for SiC. After the degrease (Step 1 Figure 4.5) the lower wing of the C-KLL line at 272 eV is relatively wide as is the upper wing at 260 eV. Also the characteristic features at 245 eV and 252 eV and the shoulder at 266 eV are nonexistent. The HF dip (Step 2 in Figure 4.5) helps sharpen the lower wing and upper wing (261 eV) and plasmon peak. However, it is only after the hydrogen etch (Step 3 in Figure 4.5) that the shoulder at 266 eV is present. A final HF dip (Step 4 in Figure 4.5) removes a significant amount of oxide attenuating the C-KLL spectra sharpening all of the features at 245 and 252 eV.

The Si/C ratio of the standard surface (Step 3 in Figure 4.3) is 0.6 while that for the stepped surface is 0.8. These values were calculated by using Equation 3.5 with sensitivity factor ($S_{Si}/S_C = 1.06$), that includes λ, based upon measurements of stoichiometric films grown using monomethyl silane.

4.2 Pd Studies

This section presents the study aimed at investigating the interaction of Pd with stepped and standard surfaces on 6H-SiC, both at room temperature and annealed at 670 ^{o}C. As a basis for this, the results of a study of Pd interaction with the Si (100) 1x1 hydrogen terminated surface are probed first. Then the results for the interactions between Pd and SiC are given.

4.2.1 Pd Interactions on the Si (100) Surface

To better understand the formation of Pd silicides with SiC, a study of Pd interaction with the Si (100) surface was conducted. In these studies, the Si (100) surface was cleaned and stripped off the oxide layer using the modified Fenner etch (MFE). This is known to produce the hydrogen terminated Si (100) 1x1 surface. In this study AES spectra were obtained for four un-annealed Pd films of different thicknesses (0.7 nm – 2.8 nm) and a 2.8 nm film annealed at 500 ^{o}C.

Figure 4.6 shows a series of spectra depicting the evolution of the surface starting with the elemental Si-KLL peak (92 eV) of the Si. (100). After 0.7 nm of Pd is deposited, an elemental Pd peak is observed at 45 eV and the main elemental Si-LMM

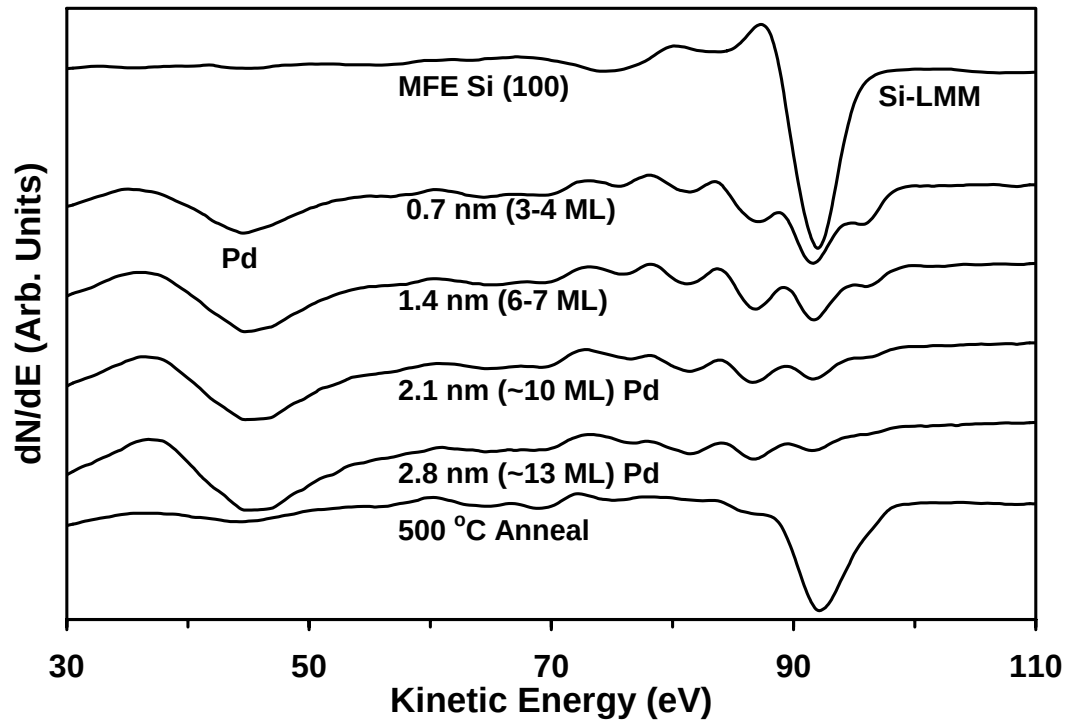

Figure 4.6. Si-LMM spectra for the Pd- Si (100) study.

peak at 92eV is replaced by a set of silicide peaks 76 eV, 81 eV, 87 eV, 92 eV and 96 eV indicating that Pd reacts at room temperature with Si to form silicides. Using the peak to peak ratios of the 87 eV and 92 eV silicide features as documented in the work by V M Bermudez,[38] (as described in Section 3.3.1.1 and shown in Figure 3.9) the stoichiometry of the deposited silicides were found to be: Pd_3Si for the 0.7nm film, $Pd_{3<x<4}Si$ for the 1.4 nm film, Pd_4Si for the 2.1 nm film and $Pd_{x>4}Si$ for the 2.8 nm film. The fact that silicide peaks are clearly seen even after 13-14 ML of Pd is deposited suggests that Si reacts

readily with Pd and that there is significant intermixing of Si and Pd at room temperature. After the 500 ^{o}C anneal, the re-emergence of a strong peak at 92 eV, along with the disappearance of the silicide peaks, suggest that the resulting film is silicon rich. However, the peak does not have the strong shoulder at 87eV characteristic of elemental Si. This is combination with the weak Pd peak at 45 eV suggest that Si may possibly still interacting with the Pd.

4.2.2 Pd Interactions with Stepped and Standard 6H-SiC

This section deals with interaction of both annealed and un-annealed Pd films of different thicknesses on stepped and standard surfaces. The discussion will start with a discussion of the un-annealed Pd films, in order to establish the initial state of the deposited films. This will be followed by the discussion of the annealed films. Figures containing the AFM images of the annealed standard and stepped surfaces are located at the end of this section. This is done so that the evolution of the surface morphology can be easily viewed. In each case, the figure containing micrographs is followed by a figure of representative line profiles from the images.

AFM and AES results for un-annealed films on standard and stepped surfaces produced the same results. Because the results are so similar, and for the sake of brevity, it is only necessary to show one set of results which exemplifies un-annealed Pd films on SiC.

Figure 4.7 shows AES results for un-annealed α-SiC with Pd films of 0.4nm (1-2 ML), 0.7 nm (2-3 ML) and 8.5 nm (~39 ML). As the thicker films are deposited there is increase in the Pd-MNN peak at 327 eV and the Pd peak at 45 eV. At the same time the Si-LMM peak is simply attenuated, and it exhibits no line shape changes associated with silicide formation. The only suggestion of an interaction of Pd with the SiC is a slight shift of the Pd feature at 45 eV. The C-KLL C peak broadens and is attenuated. The broadening occurs because the Pd-MNN peak at 282 eV increases in intensity as the Pd film increase in thickness. This Pd-MNN peak at 282 eV is important to remember later when considering the implications of line shape changes to the C-KLL peak at 272 eV. It should also be noted that the O-KLL peak is almost completely attenuated with 0.7 nm (3-4 ML) of Pd deposited, and the peak is not visible when 39-40 ML are present.

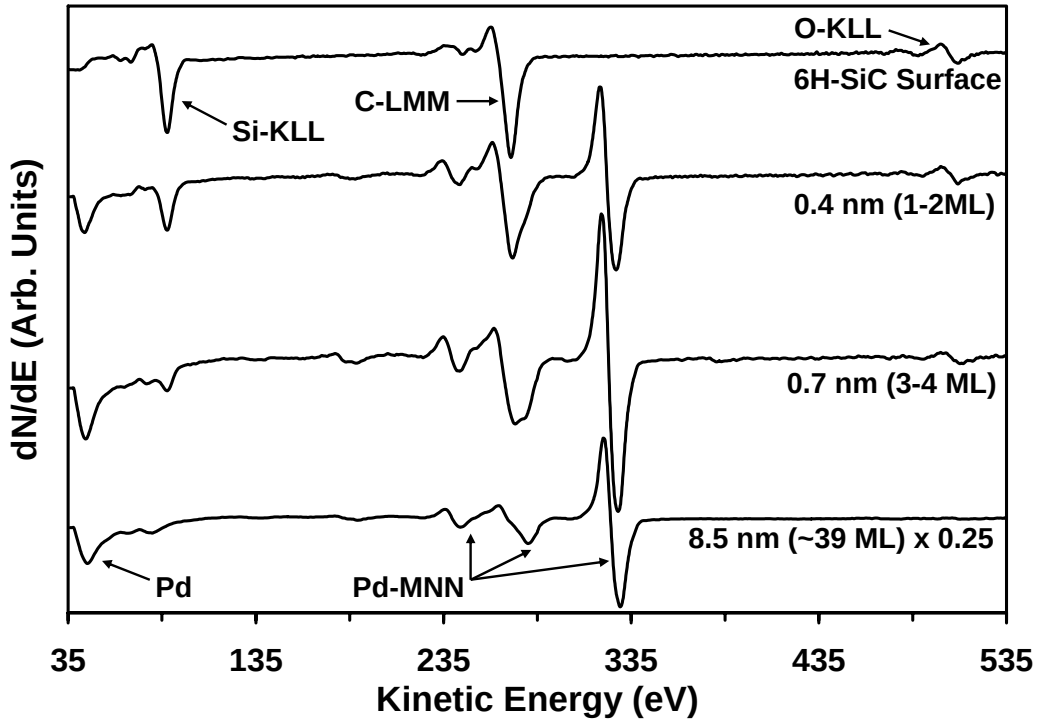

Figure 4.7. Survey spectra of un-annealed Pd films on a 6H-SiC.

Figure 4.8 show the AFM images for an on axis stepped surface with a 46 nm (257 ML) thick film of un-annealed Pd. The RMS roughness of the terraces is 0.26 nm and 0.50 nm over all. This compares closely to 0.26 nm and 0.35 nm for the terrace and overall (respectively) RMS roughness for the stepped on axis sample presented in Figure 4.2 (b). Moreover, the steps are still clearly visible. Again, similar results were observed for standard surfaces. Hence, Pd forms a stable conformal film on both standard and stepped surfaces at room temperature.

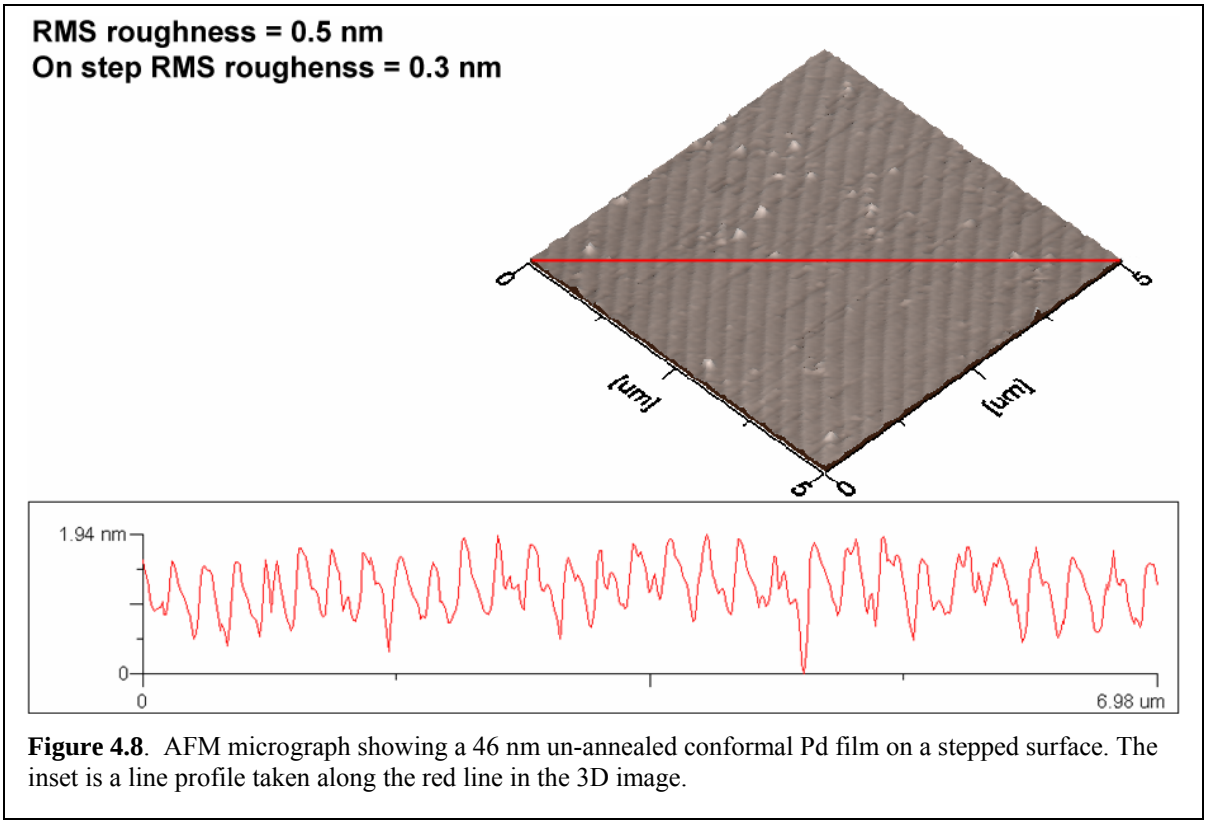

Figure 4.8. AFM micrograph showing a 46 nm un-annealed conformal Pd film on a stepped surface. The inset is a line profile taken along the red line in the 3D image.

After annealing at 670 ^{o}C, the surface composition and morphology are found to be strong functions of the initial surface morphology and initial film thickness. In the subsequent discussion, all Pd-film-thickness values refer to the initial Pd-film thickness prior to annealing, and unless other wise mentioned the films have been annealed.

Figure 4.9 shows the Si-LMM AES spectral region for a series of annealed Pd films on the standard SiC surface as well as reference spectra for the initial SiC surface and the 46.5 nm thick Pd overlayer prior to annealing. Figure 4.10 shows the corresponding C-KLL and Pd-MNN spectral regions. Compared with the reference spectrum for SiC (Standard Surface in Figure 4.9), the spectrum for the annealed 0.4 nm (1-2 ML) film shown in Figure 4.9 shows evidence of attenuation. In addition, it provides evidence of broadening in the lower wing of the Si-LMM peak at 88 eV and the emergence of a weak shoulder at 94 eV. As seen in Figure 4.9 for the thick Pd overlayer, there are no elemental Pd features that can contribute to the Si-LMM lineshape in this region. Consequently the observed lineshape changes are indicative a reaction to form Pd_xSi. The spectra for the films of 0.7 nm (3-4 nm) and 8.5 nm (~38 ML) thickness

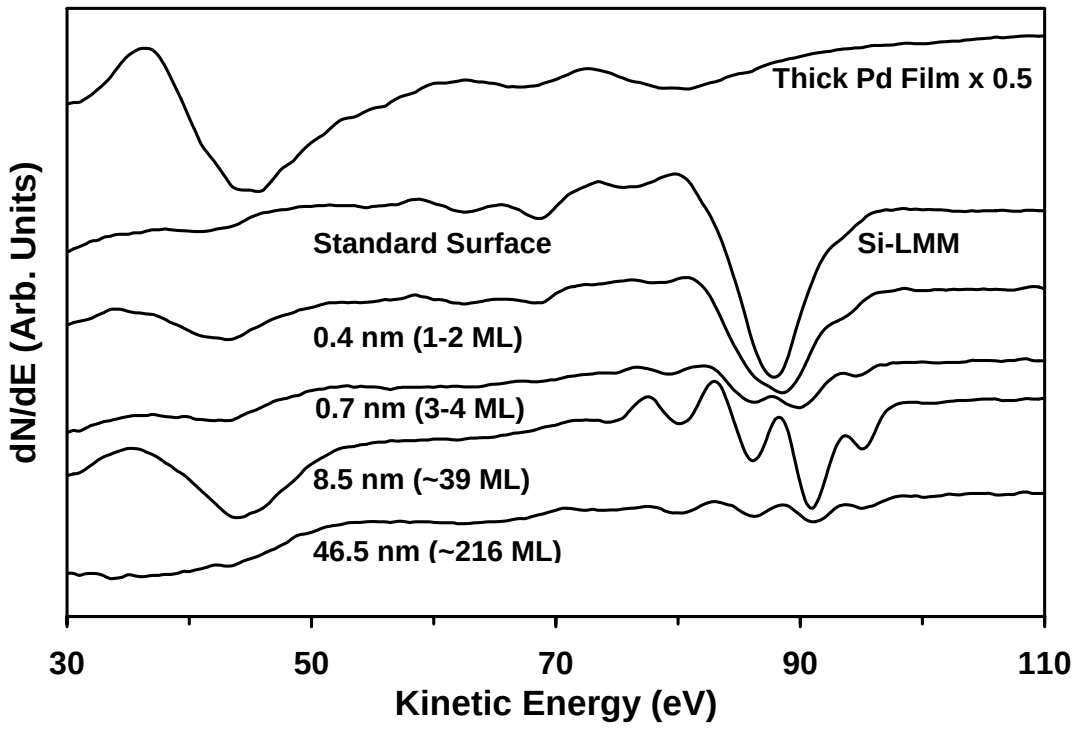

Figure 4.9. Si-LMM spectra of annealed Pd films on standard surfaces.

(Figure 4.10) exhibit increasingly well-formed silicide peaks. Again, following Bermudez,[38] the ratio of the peak-to-peak intensities of the silicide features indicate that the composition of the silicide corresponds to $Pd_{x>4}Si$ for the 0.7 nm film and Pd_3Si for the 8.5 nm film. For the annealed 46.5 nm (~257 ML) film (Figure 4.9), the composition also corresponds to Pd_3Si, but the overall spectrum is significantly attenuated compared to the spectrum for the 8.5 nm film.

Compared with the C-KLL reference spectrum for SiC shown in Figure 4.10 (Standard Surface), the C-KLL lineshape for the 0.4 nm film shown in Figure 4.10 provides evidence of broadening of the lower wing at 272 eV as well as a broadening and reduction in intensity of the upper wing at 261 eV. While there is no significant change in intensity of the feature at 250 eV, there is a sharpening of the plasmon feature at 236

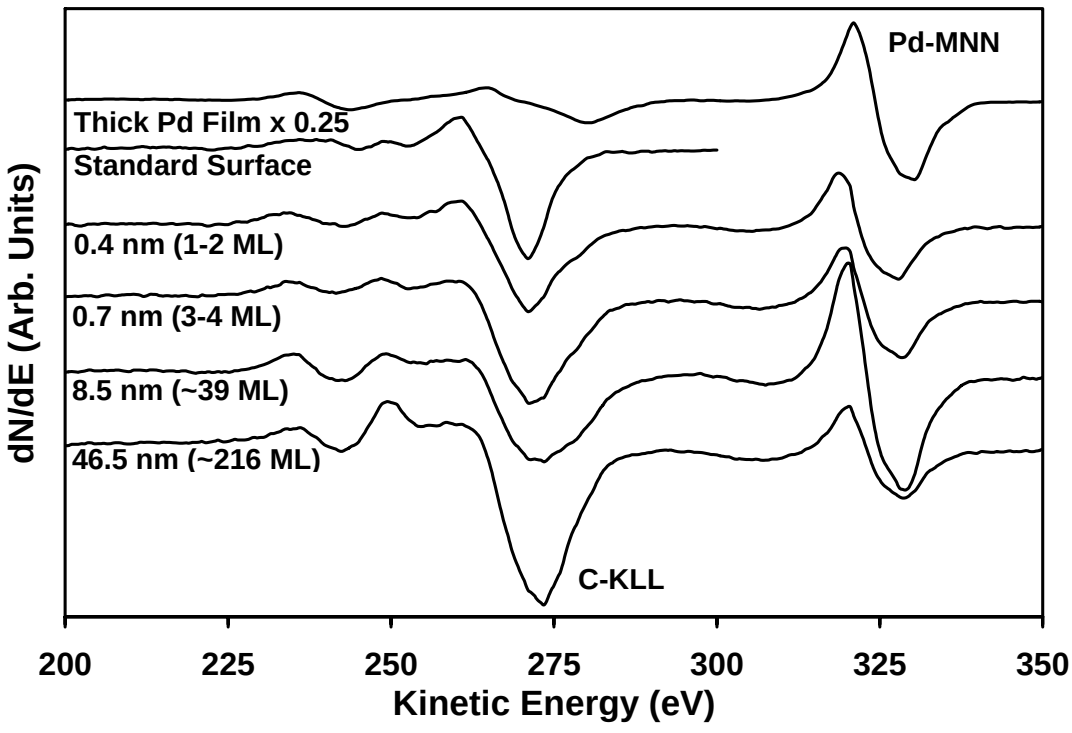

Figure 4.10. C-KLL and Pd-MNN spectra of annealed Pd films on standard surfaces.

eV. In the absence of Pd, these changes would be indicative of a conversion of C from the sp^3-C state in SiC to the sp^2-C state in graphite.[74] With Pd present, however, features in the Pd-MNN (Figure 4.10 Thick Pd Film) may also contribute to these changes. The situation is further complicated by the fact that the Pd-MNN lineshape may change as Pd reacts with Si. Given the relative intensities of the Pd-MNN peaks, however, their main effect on the C-KLL peak in 0.4 nm spectra (Figure 4.10) is simply to broaden the lower wing of the C-KLL peak. The lineshape changes associated with the upper wing of the C-KLL peak in 0.4 nm spectra are due primarily to graphite formation. As evidenced in the 0.7 nm, 8.5 nm and 46.5 nm spectra (Figure 4.10), these changes continue with increasing initial Pd film thickness to the extent that the C-KLL lineshape in Figure 4.10 for the 46.5 nm film is representative of graphite rather than SiC.

The Si-LMM in the 8.5 and 46.5 nm spectra in Figure 4.9 both correspond to Pd_3Si. Consequently, we expect to see same amount of C (graphite) in the AES sampling volume because the stoichiometry is the same. In particular, since the lineshapes are not changing, the peak-to-peak C-KLL /Si-LMM intensity ratios should be the same. What is observed, however, is roughly ten-fold increase in this ratio on going from the 8.5 nm to the 46.5 nm film. For this to occur with no change in lineshape requires that the graphite overlay the silicide for the 46.5 nm film. Based on the attenuation of the Si-LMM peaks for the 46.5 nm film relative to the 8.5 nm film (Figure 4.10), the thickness of the graphite layer is ~0.8 nm.

Figure 4.11 shows the Si-LMM AES spectral region for a series of annealed Pd films on the stepped SiC surface as well as reference spectra for the initial stepped SiC surface and the thick (46.5 nm) Pd overlayer prior to annealing. Figure 4.12 shows the corresponding C-KLL and Pd-MNN spectral regions. As before, there are no features in the Pd spectrum (Thick Pd Film Figure 4.11) that can contribute to the Si-LMM lineshape. Compared with the spectrum for the stepped surface , the spectrum for the 0.4 nm (1-2 ML) film seen in Figure 4.11 is attenuated, as it should be, by the Pd overlayer, but otherwise shows no evidence of reaction to form the silicide. This contrasts with the standard surface where reaction to form Pd_xSi is observed, and it suggests that the stepped surface is more thermally stable than the standard surface. This is most likely due to improved crystal ordering for the stepped surface as compared to the standard

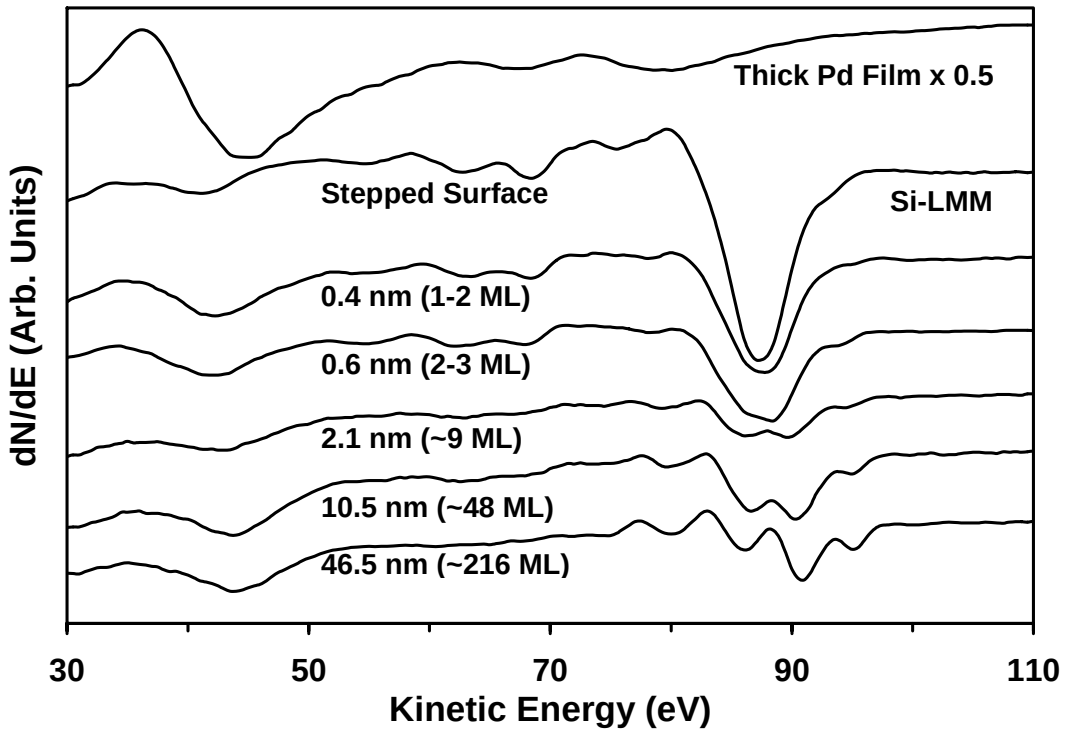

Figure 4.11. Si-LMM spectra of annealed Pd films on stepped surfaces.

surface that still has surface and near-surface damage associated with the polishing process. It is clear from this observation that reactant mobility plays a role in initiating reactions at the Pd-SiC interface.

The Si-LMM spectrum in Figure 4.11 for the 0.6 nm (2-3 ML) film shows clear evidence of silicide formation, and the spectra for the 10.5 nm (~48 ML) and 46.5 nm (~216 ML) films exhibit increasingly well formed silicide peaks. Based on lineshape analyses, these films correspond to $Pd_{x>4}Si$ and Pd_3Si, respectively.

The C-KLL spectra for the annealed films on stepped surface are shown in Figure 4.12. These are similar to those for the standard surface with respect to the conversion of sp^3-C to the sp^2-C. That is, again lineshape changes corresponding to graphite formation along with the reaction to form Pd_xSi are observed. As just noted above, composition of

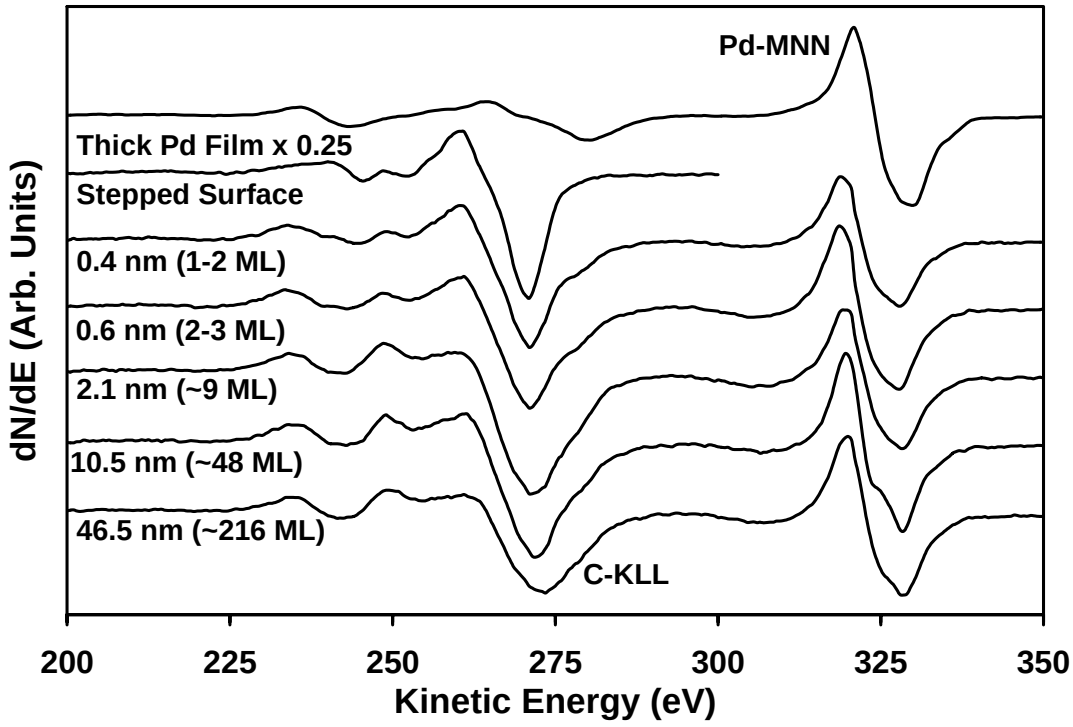

Figure 4.12. C-KLL and Pd-MNN spectra of annealed Pd films on stepped surfaces.

the 10.5 nm and 46.5 nm films are $Pd_{x>4}Si$ and Pd_3Si, respectively. Thus, the graphitic contribution to the spectrum for 46.5 nm film should be greater than that of the spectrum for the 10.5 nm annealed. This, however, is not observed, and in fact, the overall intensity of the C-KLL peak for 46.5 nm is slightly less than 10.5 nm. This is consistent with the silicide overlaying the graphite on the stepped surface, which contrasts with a graphitic overlayer for the standard surface.

This behavior once again suggests possible differences in the reactant transport and mobility mechanisms for the stepped and standard surfaces. Specifically, the results are consistent with silicide growth by Si out-diffusion and reaction on the stepped surface, while growth on the standard surface involves Pd in diffusion. In this case, it appears that the surface and near-surface damage on the standard surfaces not only facilitates the initiation of the reaction but also helps to set the direction of reactant transport.

As mentioned previously the as deposited Pd films are conformal with the substrate surface. Annealing these films at 670 ^{o}C leads not only to silicide formation but also to characteristically different film morphologies that depend on the initial surface. Figure 4.13 shows the morphologies of 0.4 nm, 8.4 nm, and 46.5 nm films on a standard surface. Figure 4.14 shows the corresponding line profiles. The image of the 0.4 nm film shows that the standard surface is clearly visible, and the RMS surface roughness is 0.44 nm (compared to 0.50 nm for the as-received sample in figure 4.1). The small clusters seen on the surface are possibly reacted Pd, and the initial formation of hillocks observed with thicker films. This corresponds well to the AES spectra (Figures 4.9 and 4.10) that show a slight reaction between the Pd film and SiC. The image of the 8.4 nm film in

Figure 4.13 shows many small tightly packed clusters. The surface of the 8.4 nm film has an over all RMS roughness of 16.8 nm, which is twice the thickness of the original film. The large RMS roughness value and change in surface morphology correspond to a silicide (Pd_3Si) peaks in Figure 4.9 for the 8.4 nm film. The AFM image of the 46.5 nm film in Figure 4.13 reveals large irregular hillock features. The 46.5 nm film has an overall RMS roughness 8.3 nm, less than half the value for the 8.4 nm surface, demonstrating the dependence of the morphology on the thickness of the original Pd film. As previously discussed, the AES spectra (Figures 4.9 and 4.10) for the 46.5 nm surface's reveal that Pd_3Si is present but is greatly attenuated. Therefore, the change in surface morphology is most likely due to the production of a graphite overlayer on the surface.

The AFM images of the film annealed on stepped surfaces provide striking difference in morphology. For the 0.4 nm film the AFM is essentially the same as before the deposition. There is no evidence of any changes in morphology. This correlates to the matching set of AES spectra in Figure 4.11 and 4.12 which indicate that the 0.4 nm Pd film on the stepped surface has not reacted with the Pd (in contrast to 0.4 nm film on the standard surface.) Therefore, the lack of change in morphology strengthens the argument that the stepped surface is more thermally stable then the standard surface.

The AFM images for the 5 nm (2-3 ML), 6 nm (2-3ML), 2.1 nm (9-10 ML) and 10.5 (48 ML) film in Figure 4.15 show the evolution of triangular features on the stepped surface. This is in contrast to the round hillock like features observed on the 38 ML film on the standard surface in Figure 4.13, demonstrating the dependence of morphology on the surface. Please note that the shape of these features was determined to be real and not an artifact of the AFM tip. As the thickness of the film increases from 0.5 nm to 2.1 nm

the RMS roughness increases from 0.43 nm to 2.1nm. As shown by the line profiles for the 2-3 ML (0.5nm), 2-3 ML (6 nm), 9-10 ML films in Figure 4.16, triangular features are ~100 nm from their vertex to base and their maximum heights vary from 4.1nm to 13 nm depending on the initial film thickness.

The line profile for the 48 ML film (Figure 4.16) was chosen as a representative profile of the entire surface showing features of 677 nm across and 37 nm high, with an over all surface RMS roughness of 11.1 nm. However there were features found as large as 1100 nm wide and 51 nm high. The AFM image of the 48 ML film (Figure 4.15) shows that the surface features are still triangular in shape, but are much less well defined. The change in shape and size of the features signals that a thickness driven transition in morphology has taken place.

When a 46.5 nm Pd film on the stepped surface was annealed, hillock-like Pd_3Si features replaced the triangular crystallites observed for the thinner films. Like the 46.5 nm film on the standard surface, the graphite production seems to be associated with a change in growth mode of the film. The line profiles of the hillock features observed on the 46.5 nm stepped surface are show in Figure 4.16, and may be compared with 46.5 nm film on the standard surface shown in Figure 4.14. This highlights the difference in morphology between the films. The difference is that the hillocks on the 46.5 nm film on the stepped surface tend to be much taller and narrower. This is consistent with the AES results for the 46.5 nm film on the stepped surface indicating silicide had pushed through to the surface. Hence, a different growth mode exists between the 46.5nm films on the standard and stepped surfaces.

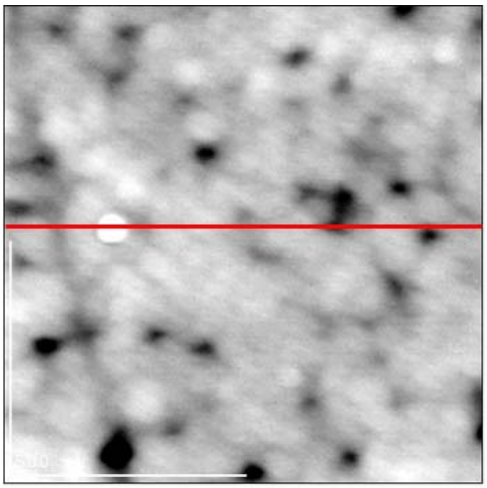

0.4 nm (1-2 ML)
RMS roughness= 0.44 nm

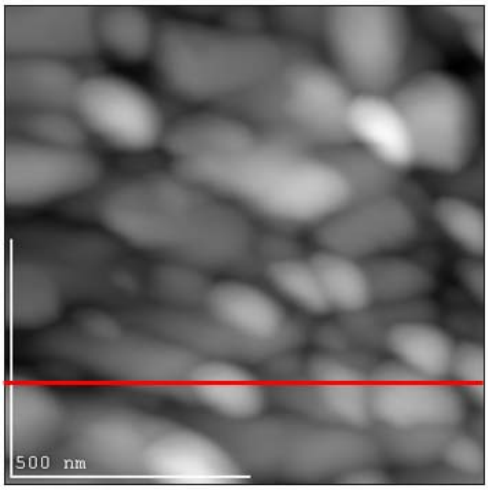

8.4 nm (~39 ML)
RMS roughness= 16.8 nm

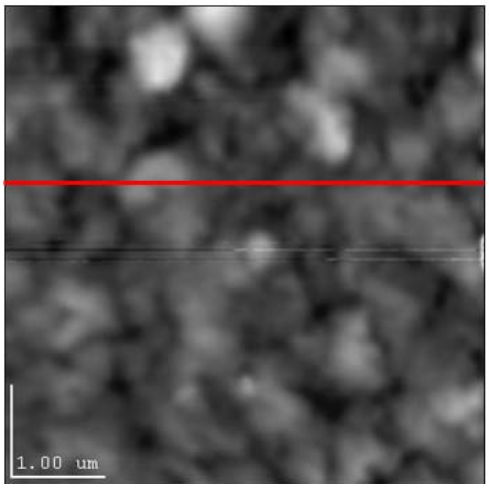

46.5 nm (~216 ML)
RMS roughness= 8.3 nm

Figure 4.13. AFM images of Pd films annealed on standard surfaces**.** The red line across each AFM image correspond to a line profile in Figure 4.14.

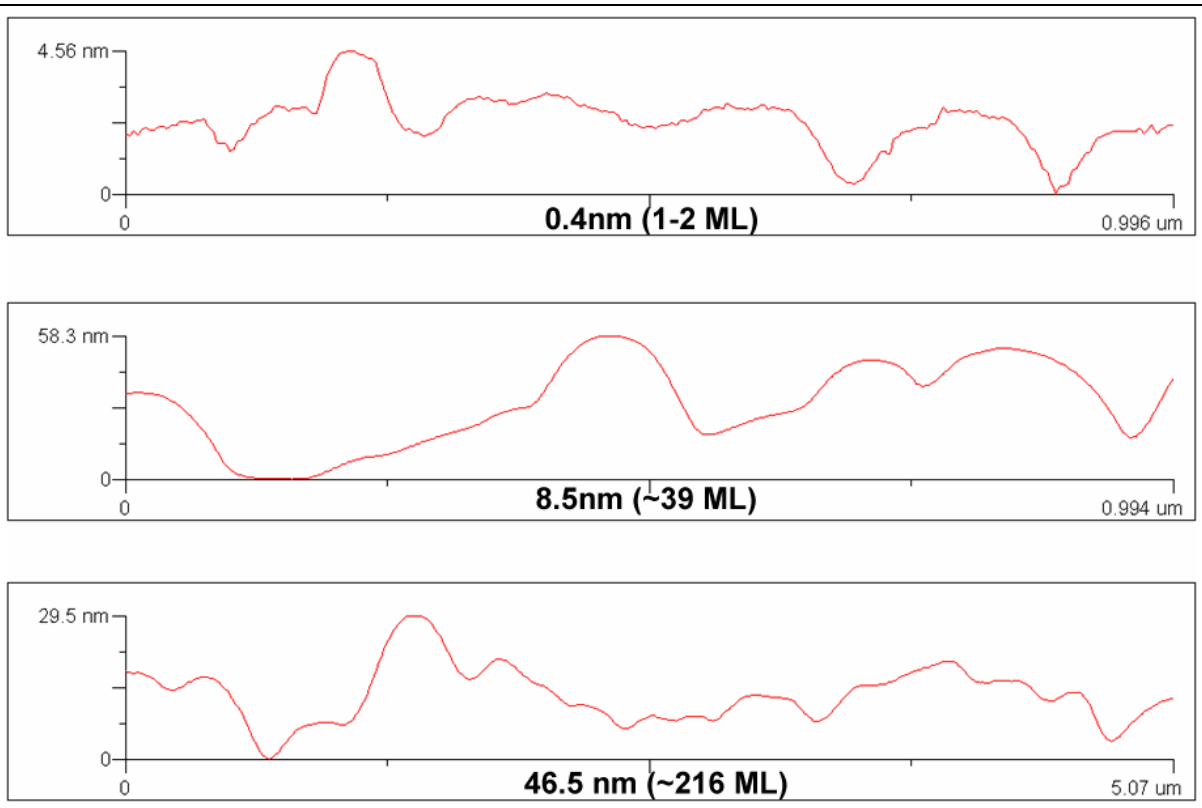

Figure 4.14. Line profiles for AFM images of annealed Pd films on standard surfaces (Figure 4.15). Note the line profiles correspond to the red lines across the respective images in Figure 4.15.

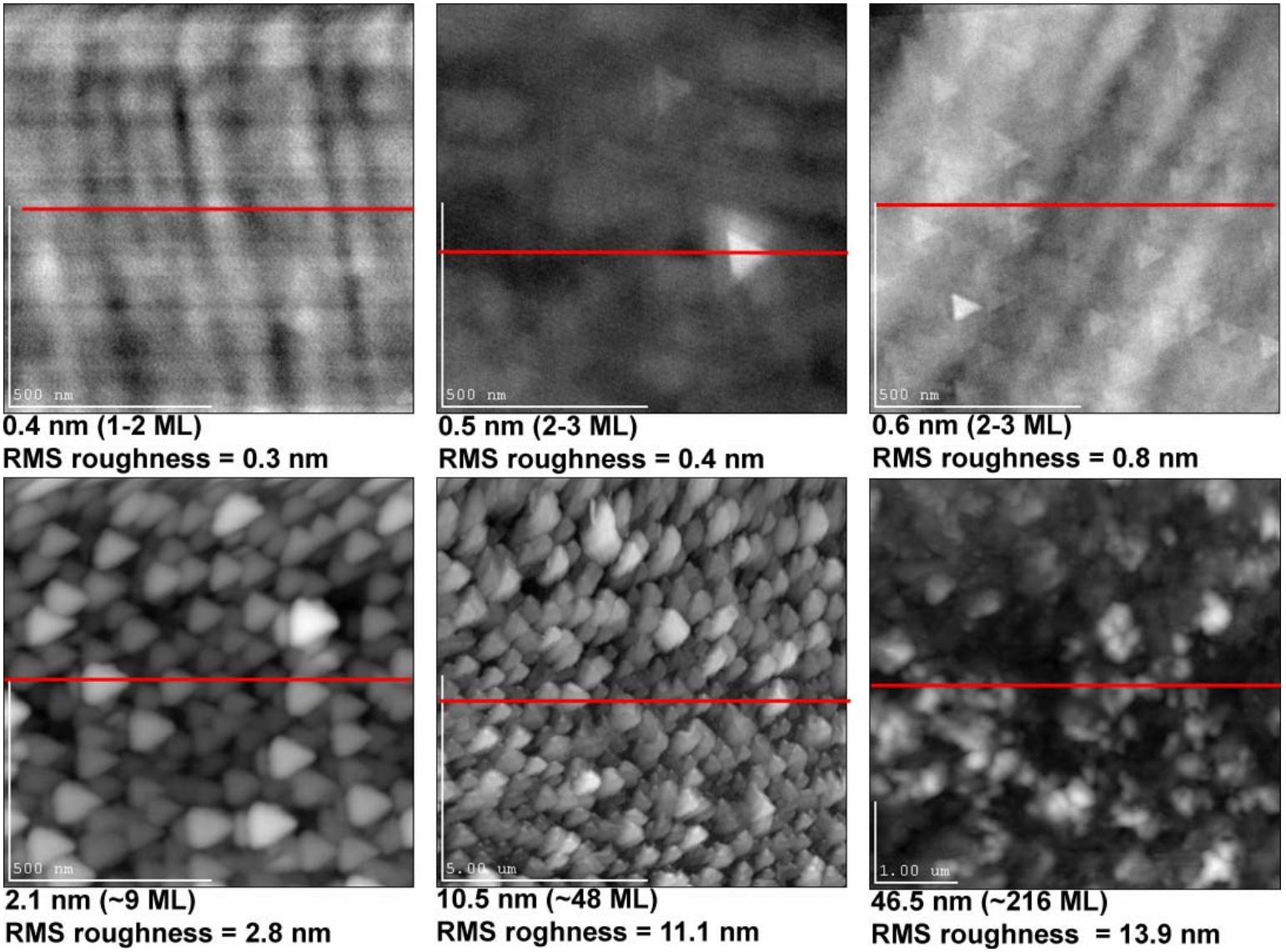

Figure 4.15. AFM images of Pd films annealed on stepped surfaces. The red line across each AFM image correspond to a line profile in Figure 4.16.

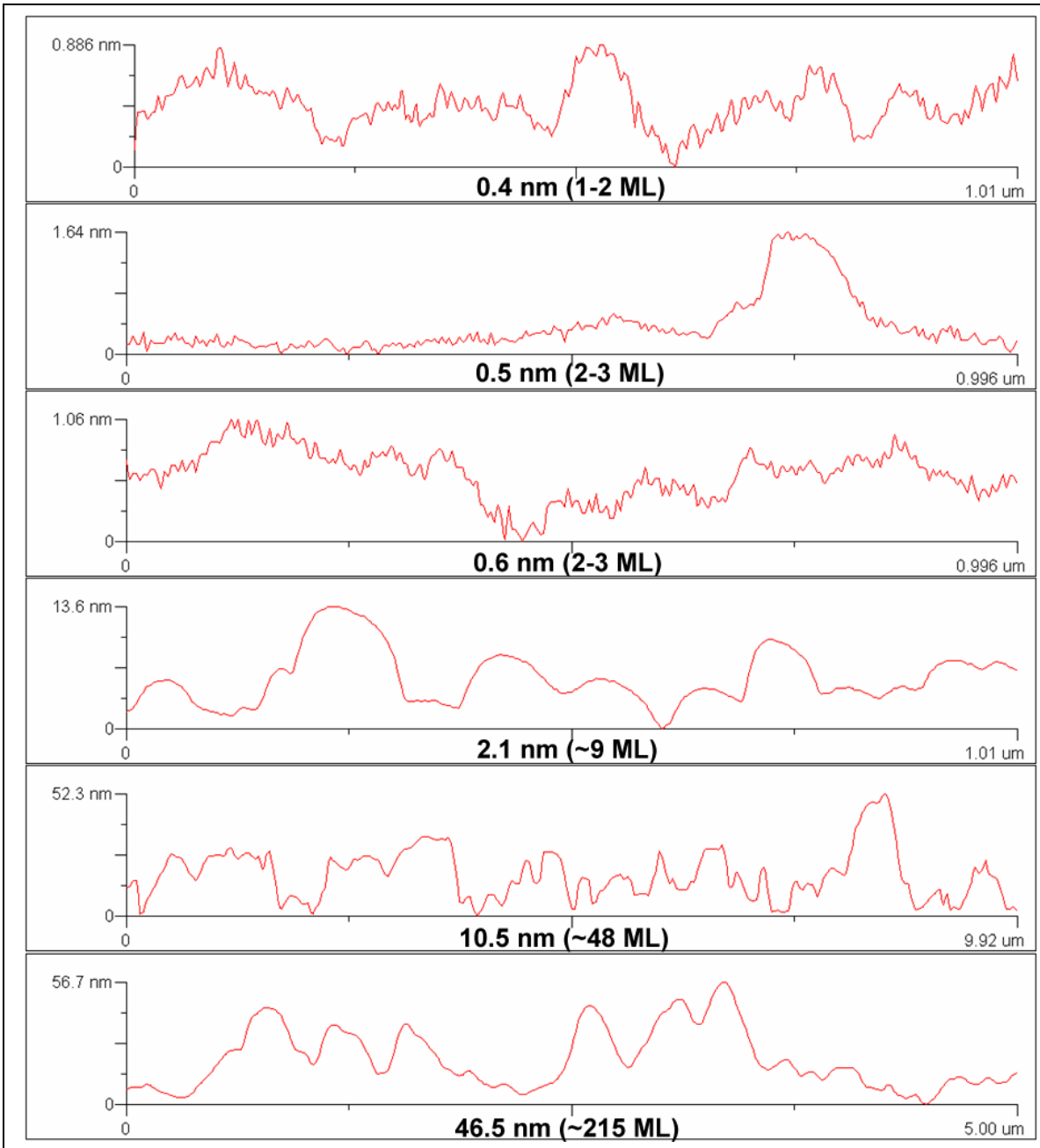

Figure 4.16. Line profiles for AFM images of annealed Pd films on stepped surfaces. Note the line profiles correspond to the red lines across the respective images in Figure 4.15.

4.2.3 Summary of Pd Studies Results

Below is a list areas of interest and key results from the Pd Studies discussed in section 4.2.1, and 4.2.2. These results are later referred to in the summary in Chapter 5.

Pd films on Si (100)

- React at room temperature to form Pd_xSi
- When annealed, Si is segregated onto the surface

Un-annealed Pd films on SiC

- Do not react at room temperature on either stepped or standard surfaces
- Are conformal with the substrate surface

Annealed Pd thin [0.4nm (1-2 ML)] films on SiC

- React to form Pd_xSi on the standard surface
- Do not react on the stepped surface

Annealed Pd intermediate [10.5 nm (~48 ML) or less] films on SiC

- Form Pd_xSi on both surfaces

Annealed Pd thick [46.5 nm (~216 ML)] films on SiC

- Form a $C/Pd_3Si/SiC$ structure on standard surfaces
- Form a $Pd_3Si/C/SiC$ structure on stepped surfaces

Annealed Pd film morphology on SiC

- Depends on initial film thickness
- Depends on initial surface state

4.3 Ni Studies

This section presents the results describing the interactions of Ni with SiC stepped and standard surfaces is presented. First, however, the results of a study exploring Ni-Si interactions. The goal of this study was to provide a greater understanding of AES line shape changes of the Si-LMM and low Ni feature at 62 eV as Ni and Si interact. Second the study of Ni-SiC interactions is presented.

4.3.1 Interaction of Ni with Si (100)

Unlike Pd-Si interactions, no AES spectra were found in the literature for Ni silicide features below 110 eV. Therefore, a short AES study was necessary to understand Ni-Si interactions and obtain lineshape information for these features. The study was conducted by collecting AES spectra of 1.5 nm (6-7 ML) and 3.0 nm (~13 ML) as-deposited Ni films on annealed MFE Si (100) and then annealing at 700 ^{o}C. A SiC anneal before deposition was done to create a front-face back face temperature correlation curve.

Figure 4.17 shows the evolution of the surface from the clean Si (100) through the 700 ^{o}C anneal. Also, for reference, a spectrum of a thick Ni film is provided. There are three key observations to be made from this set of spectra. First, no matter how much Ni is deposited, the O-KLL peak and the C-KLL are present at approximately the same intensities. High resolution spectra reveal that the C line shape is indicative of sp^2 bonding found in graphite on the MFE (100) Si surface, and in the sp^3 bonding in nickel carbide[58] even at room temperature. Second, even after 3.0 nm (~13ML) of Ni is deposited, the Si-LMM peak at 92 eV is still clearly present. With 13 ML of Ni present, the Si-LMM peak from the substrate should be completely attenuated. Therefore, there must be significant intermixing (Si out diffusion, Ni in diffusion, or both) between Ni and Si at room temperature for this to occur. Third, after annealing the Ni-LMM peaks are

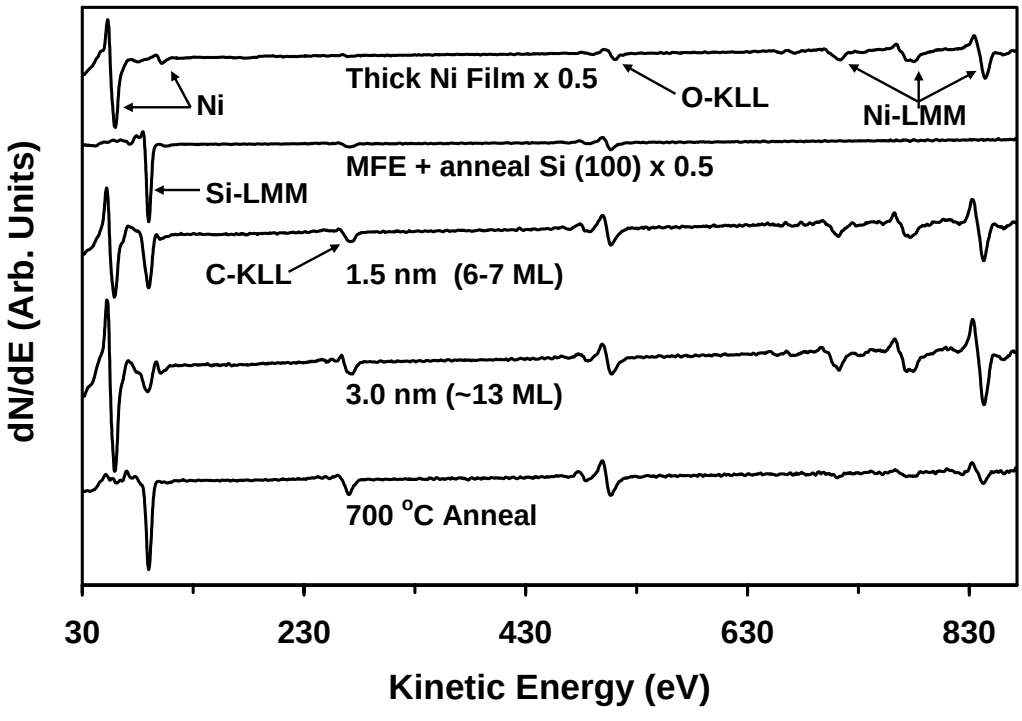

Figure 4.17. Survey spectra of the Ni- Si (100) study.

reduced by 76% and the Si-LMM peak at 92 eV increases by a factor of four. Using known sensitivity factors[75] the Si to Ni ratio was determined to be 3:1, which indicates a Si rich surface.

The high-resolution spectra, show in Figure 4.18, reveal significant lineshape changes in Si-LMM peak at 92 eV. Here, the thick Ni film spectrum (provided for reference) shows that the Ni feature at 102 eV should have relatively little effect on the Si-LMM peak at 92 eV. Likewise the Ni peak at 62 eV should not be affected by the Si-LMM peaks. As the Ni film becomes thicker, the Si-LMM peak broadens as the Ni features at 62 eV and 102 eV increases in intensity. The change in the Si-LMM peak shape clearly indicates that a chemical reaction between the Ni and Si takes place even at room temperature. The spectrum for the 1.5 nm film demonstrates the broadest Si-LMM

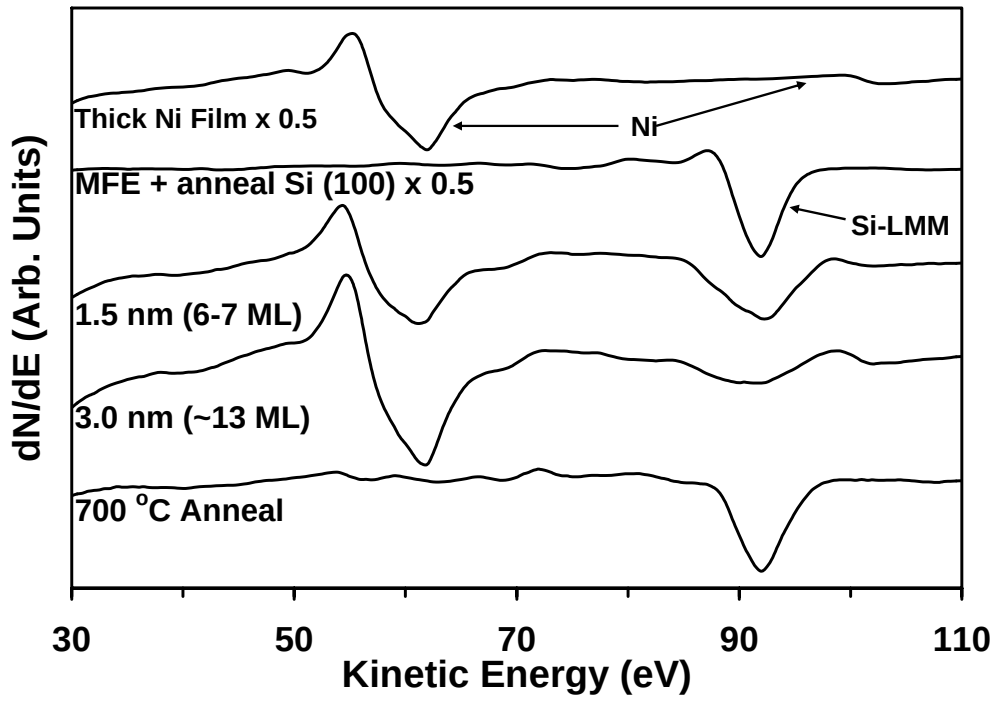

Figure 4.18. SI-LMM spectra of the Ni- Si (100) study.

line shape while still retaining some intensity. This line shape is believed to be that of Ni silicide and will be referred to in later discussions concerning the interaction of Ni and SiC. The Si-LMM peak for the 3.0 nm film show attenuation but no further broadening. This suggest that Si has stopped reacting because it is being covered by the Ni film After annealing at 700 ^{o}C the Si-LMM peak re-emerges at 92 eV and has a similar shape to that of the elemental Si, but is lacking the shoulder at 88 eV. At the same time all of the Ni peaks have been attenuated. This suggests that there has been inter-diffusion and segregation of Si on the surface. However, it is unclear if, and/or how much the Si is interacting with the Ni.

4.3.2 Ni Interactions with Standard and Stepped 6H-SiC

In this section, the AES and AFM results that are characteristic of Ni-SiC interactions on un-annealed standard and stepped SiC surfaces are presented. Thus, the results for annealed Ni films of different thicknesses are presented. AFM images and line profiles for the annealed Ni films on stepped and standard surfaces are located at the end of the section. Again, this was done in order to present the AFM data in a fashion that allows the reader to easily view the different surface morphologies between films of different thicknesses.

Un-annealed films on both stepped and standard surfaces produced similar results, both chemically and morphologically. Because of these strong similarities only one set of AES and AFM data, representative of both surfaces, is presented. Figure 4.19 presents AES survey spectra for un-annealed Ni films on the standard SiC surface. There are three key observations to be made from this set of spectra. First of all, the O-KLL peak

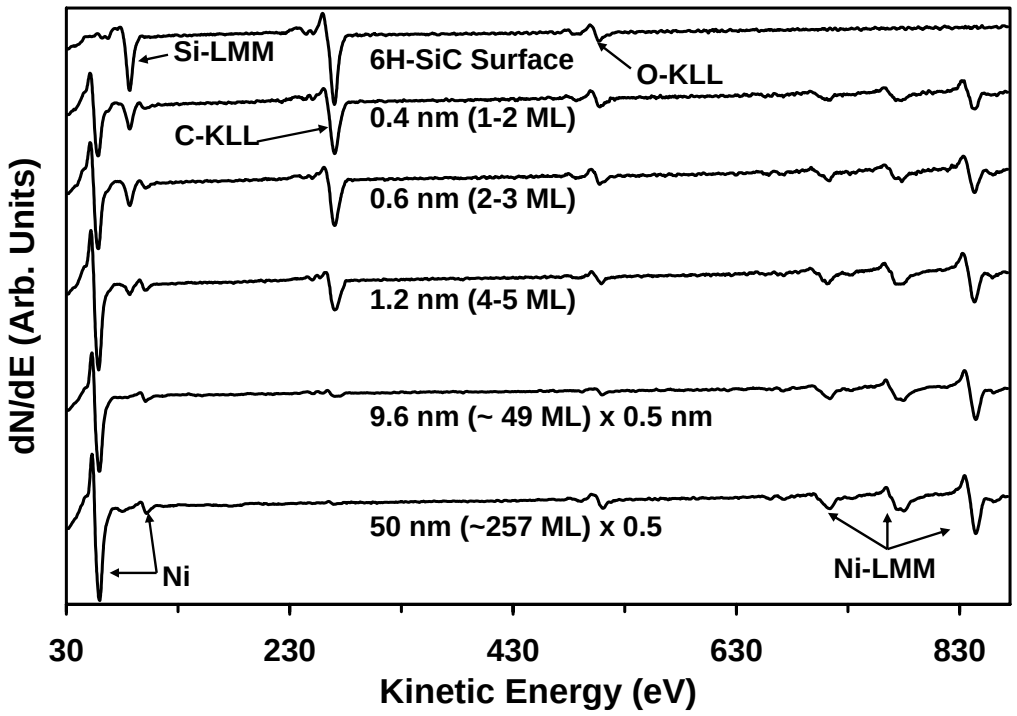

Figure 4.19. Survey spectra of un-annealed Ni films on 6H-SiC.

at 512 eV is present in all of the spectra at about the same amount, and even though the C-KLL peak at 272 is being attenuated by the Ni film there is always a C-KLL peak present. This closely follows the observations made in the Ni-Si study.

The second observation is that the Si-LMM peak at 88 eV is attenuated approximately 55 %, 70 % and 90 %, respectively, by the 0.4 nm, 0.6 nm and 1.2 nm Ni film. This is consistent with a simple model for attenuation due to the overlaying film. High resolution spectra, not shown, reveals that the Ni feature at 62 eV increases as thicker films are deposited, but there is no change in Si-LMM shape. Hence, when Ni is deposited on SiC there seems to be little or no room temperature inter-diffusion or reaction between the Ni film and the Si in the substrate. This is in contrast to the Ni-Si interaction where significant room temperature inter-diffusion and reaction were observed.

The third observation, from Figure 4.19, is that the lineshape of the C-KLL peak begins to change as soon as Ni is deposited. This is seen more clearly with high resolution spectra C-KLL spectra show in Figure 4.20. For the Standard Surface the C-KLL peak exhibits a lower wing at 272 eV, shoulder at 261 eV and plasmon peaks at 246 and 254 eV all indicative of sp^3 C bonded in SiC (i.e. SiC-C). The spectrum of a 50 nm Ni film (clearly) indicates that there are no Ni features that can interfere with the C-KLL spectra. Therefore, any line shape changes, other than attenuation, in the C-KLL peak are due to chemical interaction. The spectrum for the 0.4 nm (1-2 ML) Ni film shows a peak beginning to build in at 259 eV. After 0.6 nm on Ni is deposited new peaks are clearly developed at 253 and 259 eV, along with shift in the C-KLL upper wing to 265 eV. In addition, not only is the lower wing of the C-KLL peak attenuated by the Ni films (as

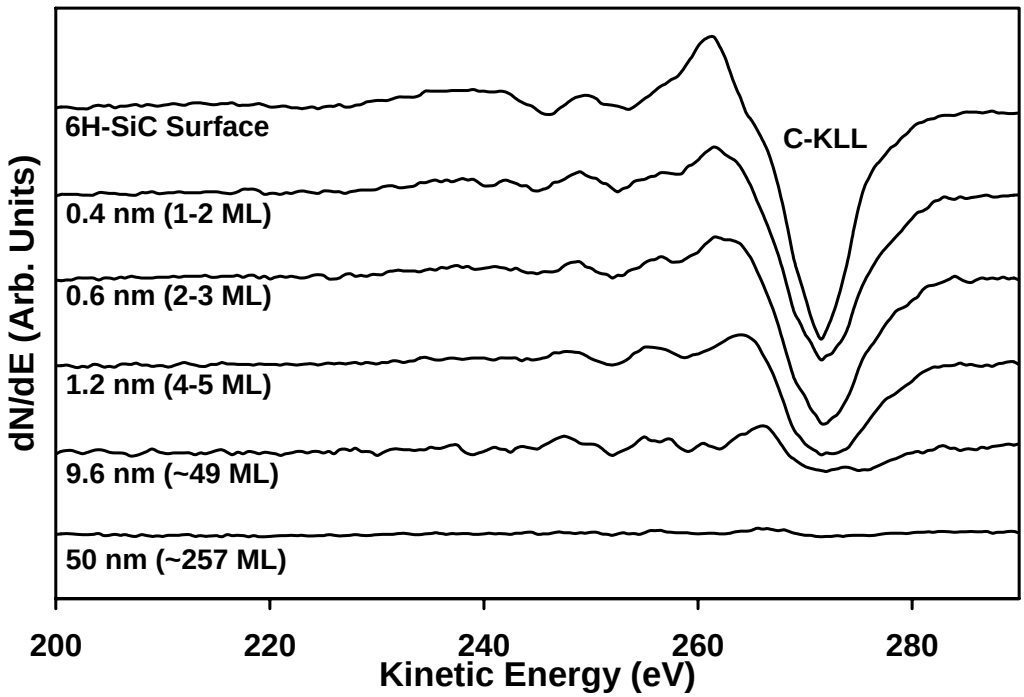

Figure 4.20. C-KLL spectra of un-annealed Ni film on 6H- SiC.

expected), but it is increasingly broadened as the Ni films become thicker. The lineshape, resulting from these changes is indicative of C bonded to Ni.[58] That is, nickel carbide. Also, even after 50 nm (~257 ML) there is still remnant this C-KLL lineshape. Considering the short IMFP of Auger electrons, this implies that there is some still some nickel carbide within a couple of monolayers of the surface. The spectrum suggests that

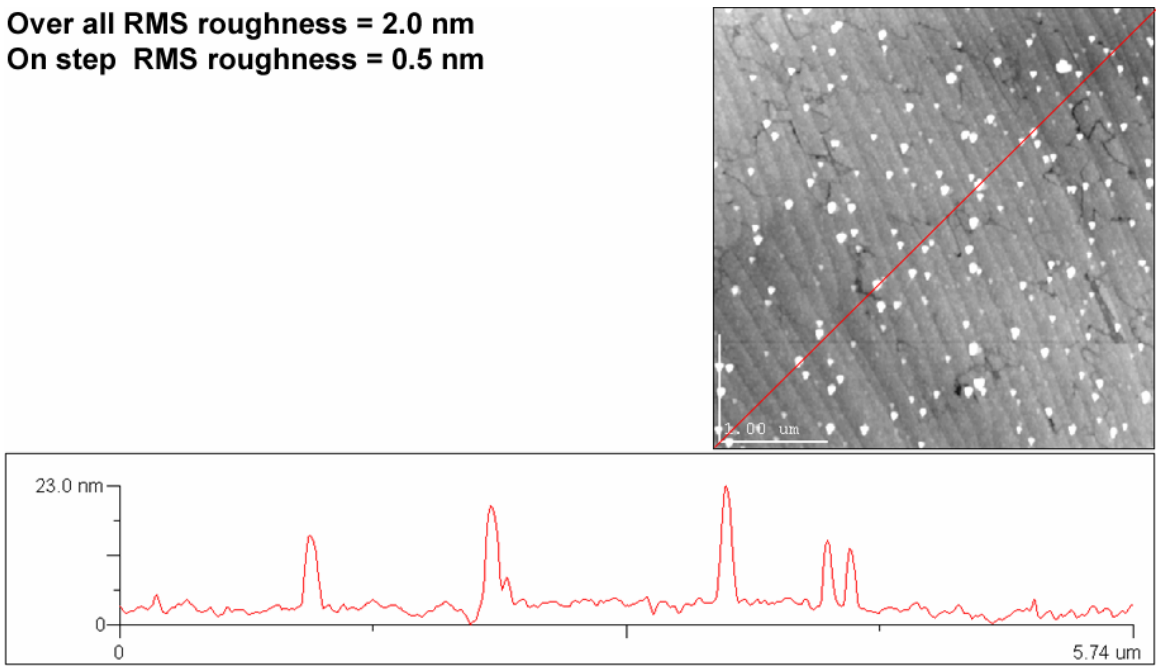

Figure 4.21. AFM image of an un-annealed 50 nm (~256 ML) Ni on SiC. The inset is a line profile taken across the red line in the image.

Ni covers the surface with little, if any, silicide formation and only a small amount of carbide formation.

Figure 4.21 is a typical AFM image of an un-annealed Ni film deposited on a stepped surface (on axis). The steps of the SiC are clearly visible with 50 nm of Ni deposited. The terrace RMS roughness is 0.5 nm, which is comparable to stepped, on axis, surfaces before deposition. However there are also many clusters that cover ~3 %

of the total surface area. The largest of these is 20 nm tall and 170nm wide. Clearly, these clusters account for only a small amount material on the surface. Therefore these clusters are possibly the source of the extremely weak carbide C-KLL peak.

Unlike the un-annealed films, annealed Ni films annealed SiC exhibit chemical and morphological dependence on initial Ni film thickness and the initial surface state (stepped or standard). In the subsequent discussion, all Ni film thickness values refer to the initial Ni film thickness prior to annealing, and unless other wise mentioned the films have annealed.

The spectra in Figure 4.22 show the Si-LMM and low energy Ni features for films on the Standard Surface. Reference spectra for a Thick Ni Film and Standard Surface in Figure 4.22 reveals that the low lying Ni feature at 62 eV may interfere with the Si-LMM

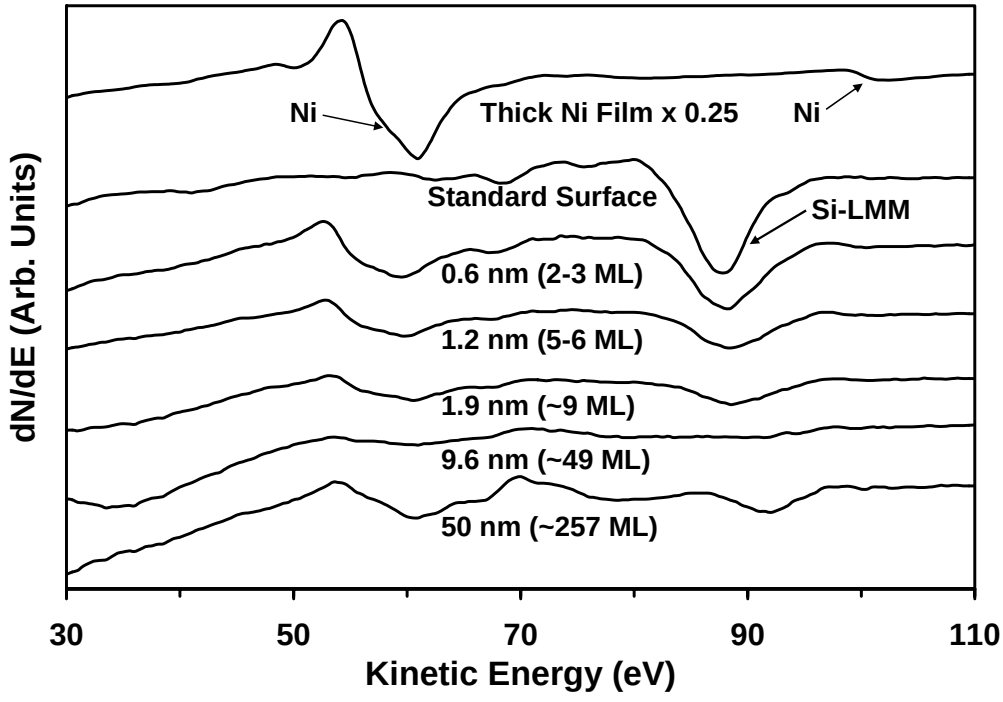

Figure 4.22. Si-LMM spectra of annealed Ni films on standard SiC surfaces.

plasmon peaks but other wise not affect the Si-LMM peak at 88 eV. Likewise the Ni feature at 102 eV will also not interfere with the Si-LMM peak.

The spectrum for the 0.6 nm film has a definite Ni peak at 62 eV. For the 0.6 nm, 1.2 nm, 1.9 nm and 9.6 nm films, the Si-LMM peak at 88 eV is attenuated and shows some evidence for changes in lineshape. The spectrum of the 1.2 nm film compared to the spectra for the 0.6 nm film reveals that the intensity of both the Si-LMM and Ni peaks is significantly reduced with little or no changes in peak shape. This trend continues for the spectra for the 1.9 and 9.6 nm films. Reduction of peak intensity without change in shape is consistent with one material being covered by another. The trend however is reversed for spectra of the 50 nm film where there is a definite increase in the Ni feature at 62 eV and there is a re-emergence of a broad Si-KLL peak at 92 eV. This broad Si-KLL peak at 92 eV is representative of the silicide peaks shown in Figure 4.18 (1.5 nm thick film).

Figure 4.23 shows the complementary set of C-KLL spectra to the Si-LMM spectra shown in Figure 4.22. Reference spectra for a Thick Ni film and the Standard Surface show that there are no Ni features that interfere with the C-KLL peak at 272 eV. After a 0.6 nm thick Ni film is annealed on the standard surface, the lower wing of the C-KLL peak at 272 eV is broadened, the upper wing at of the C-KLL peak at 261 eV and plasmon features at 245 and 252 eV are attenuated. Changes in the C-KLL peak shape along with the increase of the feature at 250 eV is associated with sp^2 bonded C (graphitic C). As evidenced by the spectra for the 1.2 nm, 1.9 nm, and 9.6 nm films the graphitic components continue to build into the C-KLL spectra as the films grow thicker. Eventually, the C-KLL line shape is representative of only graphitic C. The C-KLL

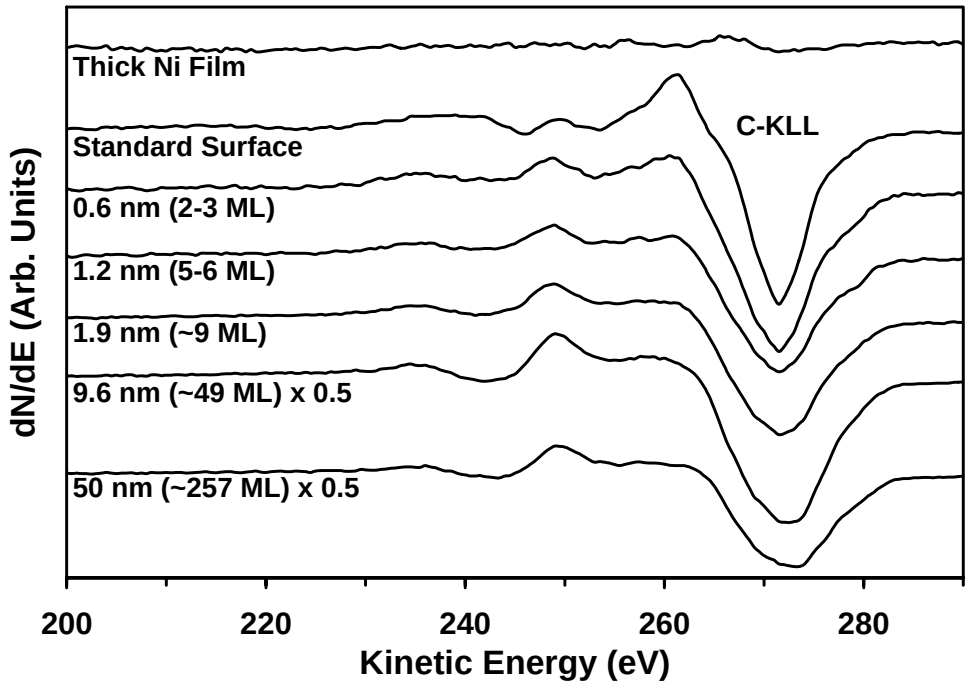

Figure 4.23. C-KLL spectra of annealed Ni films on standard surfaces.

spectrum for the 9.6 nm film is the most intense of the spectra displayed in Figure 4.23, while the Si-LMM spectra for the 9.6 nm film was the most attenuated of the spectra in Figure 4.22

The over all picture presented by the Si-LMM and C-KLL spectra of 0.6 nm -9.6 nm annealed Ni films is that the Ni inter-diffuses with the SiC to form primarily nickel silicides with a graphitic C overlayer. No significant evidence of nickel carbide formation is observed.

The spectrum of the 50 nm film in Figure 4.23 still displays the shape of graphitic C but shows a 36% reduction in the intensity of the C-KLL peak as compared to the 9.6 nm film (Figure 4.23). This reduction in intensity of the C-KLL peak corresponds to the significant increase of the Si-LMM and Ni (Figure 4.22 for the 50 nm film) This

suggests that the graphitic C overlayer is either significantly thinner or Ni silicide is on the surface.

Figure 4.24 displays spectra containing the Si-LMM spectral region for Ni films on stepped SiC surfaces. Again, reference spectra of the Stepped surface and Thick Ni film show that there is minimal interferences between the spectrum of either material. Much like the spectra presented in Figure 4.22 for the Ni on standard surfaces, the spectrum for the 0.6 nm film shows the Ni feature at 62 eV and an attenuated Si-LMM peak with some evidence for a change in lineshape.

The spectrum of the 1.2 nm film in Figure 4.24 shows the continuing attenuation and broadening, along with a slight shift to higher energy of the Si-LMM peak, while the Ni peak continues to increase in intensity. This is in contrast to the 1.2 nm film on the

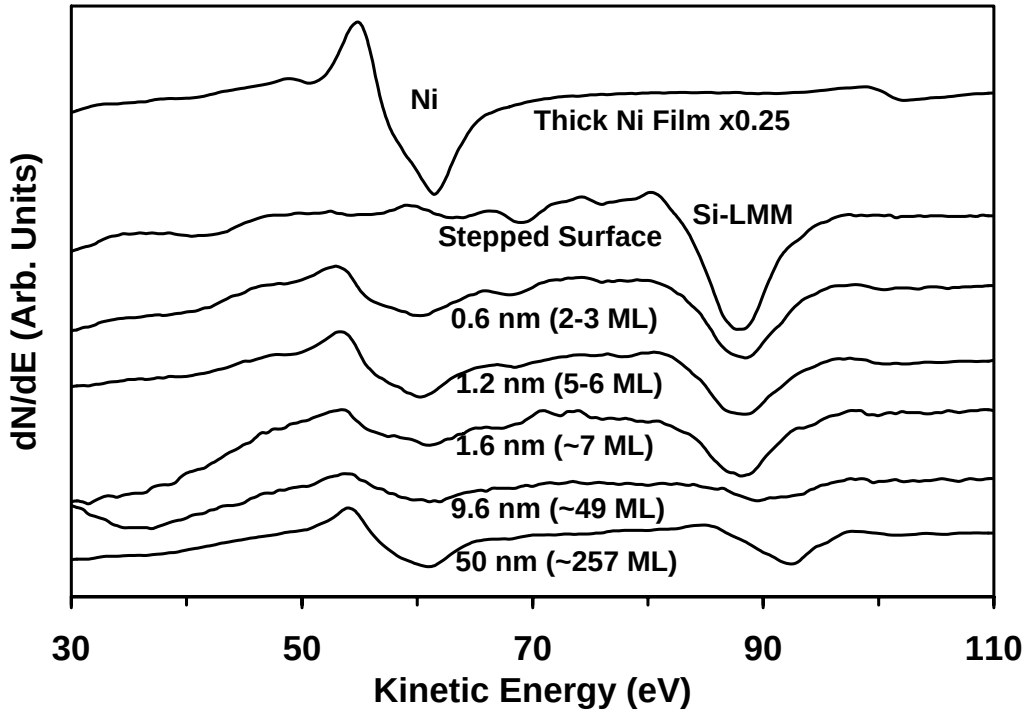

Figure 4.24. Si-LMM spectra of annealed Ni films on stepped SiC surfaces.

standard surface, shown in Figure 4.22, which exhibited an attenuation of both the Si-KLL and Ni peaks. This suggests that the Ni on the surface has interacted less with the SiC on stepped surface than on the standard surface indicating that the stepped surface is more thermally stable.

The intensity of Si-LMM and Ni peaks, decrease in the spectra of the 1.6 and 9.6 nm films shown in Figure 4.24. These spectra also show continued broadening shifting to a higher energy of the Si-LMM peak. Like the spectra of Ni films on standard surfaces of comparable thicknesses, presented in Figure 4.22, the decrease in intensity of the Ni and Si-KLL peaks suggest that the Si and Ni are being covered.

The spectrum of the 50 nm film in Figure 4.24 shows an increase and shift to 92 eV of the Si-LMM peak and increase of the Ni peak. The Si-KLL peak now clearly has the shape of the nickel silicide peak as shown in Figure 4.18 (1.5 nm film). Therefore, Ni silicide has formed either near or on the surface. This is much like the 50 nm Ni film on the standard surface, however, the Si-LMM the peak-to-peak ratio of the stepped to standard surface for the 50 nm film is 2:1. This indicates there is significantly more silicide either close to or on the surface of the stepped sample.

The corresponding C-KLL spectra, shown in Figure 4.25, for the Ni films on stepped surfaces show a complementary story to that of the Si-LMM spectra in Figure 4.24. As the film thickness increases from 0.6 nm to 9.6 nm all of the features associated with sp^2 C or graphite, as discussed for the Ni films on the standard surface, appear and strengthen as a function of initial film thickness. Even though all of the C-KLL spectra for films of 0.6 nm and 2.6 nm exhibit graphitic features, only the C-KLL spectra for the 1.6 nm and thicker films fully exhibit the lineshape associated with graphitic C. This

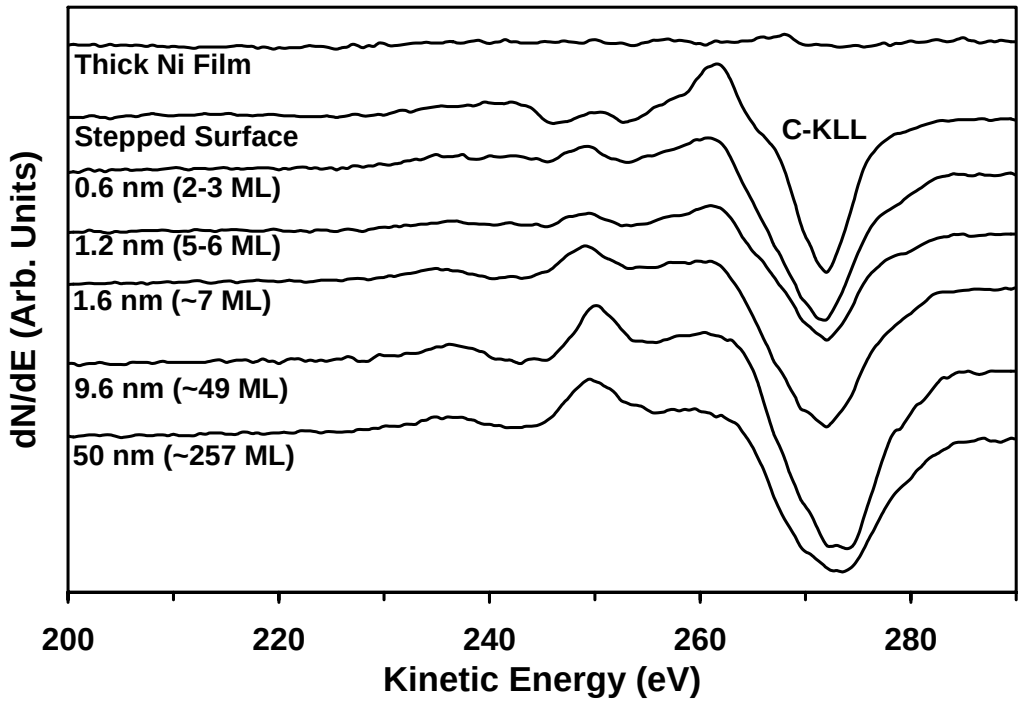

Figure 4.25. C-KLL spectra of annealed Ni films on stepped surfaces.

corresponds to the attenuation of the Ni and Si-KLL peaks in Figure 4.24, suggesting that there is a graphite overlayer. The major difference between film stepped or standard surfaces for films of 9.6 nm or less is that the Si/C (graphite) intensity is 15 % larger for the stepped than the standard surface. Therefore the graphite overlayer appears to be thinner for the stepped surface

The C-KLL spectrum for the 50 nm film, shown in Figure 4.25 is reduced in intensity by (~21%) as compared to the 9.6 nm film. This correlates to the re-emergence of the silicide (Si-LMM at 92 eV) and an increase of the Ni peak in Figure 4.24. This suggests that Ni silicide is near to or on the surface. Again, it is important to note that none of the C-KLL spectra, in figure 4.25, exhibit Ni carbide line shape present in the spectra of un-annealed films shown in Figure 4.20.

AFM results show that morphology of the surface is dependent on both the initial surface, and on the initial film thickness. Figures 4.26 and 4.27 displays the AFM images and line profiles, respectively, of annealed Ni films on standard surfaces. These correspond to the spectra in Figures 4.22 and 4.23. The AFM image of the 0.6 nm film (Figure 4.26) reveals that the surface has an RMS roughness of 0.4 nm, which is similar to the RMS roughness of the standard surface. The bumps observed in the AFM images of the un-annealed Ni films (Figure 4.21) are no longer present. The disappearance of the bumps corresponds to the disappearance of Ni-carbide-like features observed in C-KLL line shape observed in Figure 4.23. This suggests that the bumps seen on the surface of the un-annealed films correspond to Ni carbide.

The AFM image of the 1.2 nm think film on the standard surface (Figure 4.26) reveals the formation of hillock features. These tend to be round in shape with varied height and diameter with the largest being ~6 nm tall and ~150 nm in diameter. The density of these hillocks is only ~4/μm^2 and the surface is still relatively smooth (RMS roughness of 0.6 nm). The hillocks observed in the AFM image and line profile of the 1.9 nm thick film, shown in Figures 4.26 and 4.27, are similar in size and shape to those observed for the 1.2 nm film. However, the hillocks observed for the 1.9 nm film cover the entire surface and the RMS roughness is 1.48 nm. As noted above the C-KLL peak for the 1.9 nm film is that of graphitic C and the Si-LMM peak and Ni feature at 62 eV of the same film are heavily attenuated as evidenced in Figures 4.22 and 4.23. Therefore, these hillocks are mainly comprised of graphitic C.

The AFM image of the 9.6 nm thick film shows that the hillocks seen in the images of the 1.2 and 1.9 nm films are still present but larger hillocks with a less well

defined shape are also present. The larger hillocks are ~6 nm tall and ~300nm wide, and the surface has an overall RMS roughness of 3.92 nm. Hence a thickness dependent transition in morphology is observed between the 1.9 nm and 9.6 nm think films. The C-KLL line shape observed for this film (Figure 4.23) is that of graphitic C, and the S-LMM peak and Ni feature at 65 eV was almost entirely attenuated. Therefore, like the 1.9 nm think film, the features observed on the 9.6 nm film are composed of graphitic C.

Another thickness dependant transition in morphology is observed between the 9.6 nm thick Ni film and the 50 nm think Ni film on the standard surface. The AFM image and line profile, shown in Figures 4.26 and 4.27 of the 50nm thick film, show a surface with significantly larger hillocks with no specific geometrical shape. These features are as large as 14 nm tall and 750 nm wide, and the surface has an RMS roughness of 5.1nm. Recall that the AES spectra in Figures 4.22 and 4.23 for the 50 nm film on the standard surface reveal both the Si-LMM silicide peak and Ni peak are visible, along and a reduced C-KLL peak. Therefore, the morphology change observed in AFM image of the 50 nm thick film corresponds to a significant change in the chemical state of the surface.

Figures 4.28 and 4.29 show the AFM images and their respective lines profiles of the Ni films annealed on stepped surfaces. The AFM image of the 0.6 nm film shows that the clusters, seen in the image of un-annealed Ni film on SiC (Figure 4.21), are no longer present, leaving the stepped surface behind. The RMS roughness of the entire surface is 0.6 nm with a terrace roughness of 0.3 nm for the 0.6 nm Ni film (Figure 4.28). This image and RMS values are comparable to those of the stepped surface shown Figure in 4.2 (b). Like the 0.6 nm film on the standard surface, the bumps seen on the un-

annealed surface are no longer present and there is no evidence of Ni carbide in the C-KLL spectrum shown in Figure 4.25. Again this provides evidence that the bumps seen in Figure 4.21 are composed of Ni carbide

The AFM image of the 1.2 nm thick Ni film reveals the onset of hillocks on the steps of the surface. The hillocks are sparse (~3/5 μm^2) and bridge the width of the terrace and are as wide as 230 nm and as tall as 20 nm. The appearance of these hillocks corresponds to significant increase of graphitic peak shape features in the C-KLL spectrum for this film show in Figure 4.25. The terraces are still clearly visible and have an RMS roughness of 0.3 nm. The 1.2 nm Ni film has an overall surface RMS roughness of 1.0 nm.

Unlike the previously discussed Ni films the morphology of the 1.6 nm thick Ni film is dominated by platelet structures. AFM images taken, after hydrogen etching and before Ni deposition, of the SiC substrate revealed relatively narrow terraces (150 nm) in some areas and wider terraces (200 nm) in other areas. AFM images of different areas of 1.6 nm film revealed that the width of these platelets varied with position and tracked with known terrace widths. Also pre and post AFM images indicate that the platelets align their long axis parallel to the step edge. These platelets tend to be as wide as the steps, 350 nm long and as tall as 20 nm. The height of the platelets is significantly greater than the initial thickness of the Ni film; therefore a significant transport of material must have occurred. The surface of the 1.6 nm film has an overall RMS roughness of 2.8 nm, which is a significant increase over thinner films.

Similar platelets are observed on the 9.6 nm thick Ni film (Figure 4.28). These platelets tend to be as wide as the terrace and ~470 nm long aligned with their long axis

parallel to the step edge (as determined from AFM images taken prior to deposition). The platelets on the 9.6 nm Ni Film are 20-60 nm tall, which is significantly taller then the platelets on the 1.6 nm surface. Again these features are significantly greater than the initial thickness of the Ni film, indicating a substantial amount of material transport has occurred during annealing. The AES spectra for both the 1.6 and 9.6 nm Ni films (Figures 4.24 and 4.25) revealed that even though some Si and Ni features are present along with a little C in the sp^3 state, graphitic C is by far the dominant species on the surface. Therefore, these platelets are mostly made of graphitic C.

For the 50 nm Ni film on a stepped surface another thickness driven change in morphology is observed. The platelets seen in the AFM images for the 1.6 and 9.6 nm films (Figure 4.28) are no longer present. In their place are large hillocks with bumps on top of the hillocks. The hillocks are as large as 2 μm in diameter and 25 nm tall. The bumps tend to have dimensions of 300 nm in diameter and 25 nm high. The surface has an RMS roughness of 10.4 nm. The emergence of this new surface structure correlates to the AES spectra for the 50 nm film (Figures 4.24 and 4.25) that suggest that elemental Ni and Si have returned to the surface. This suggests that the bumps are Ni carbide on island of graphite.

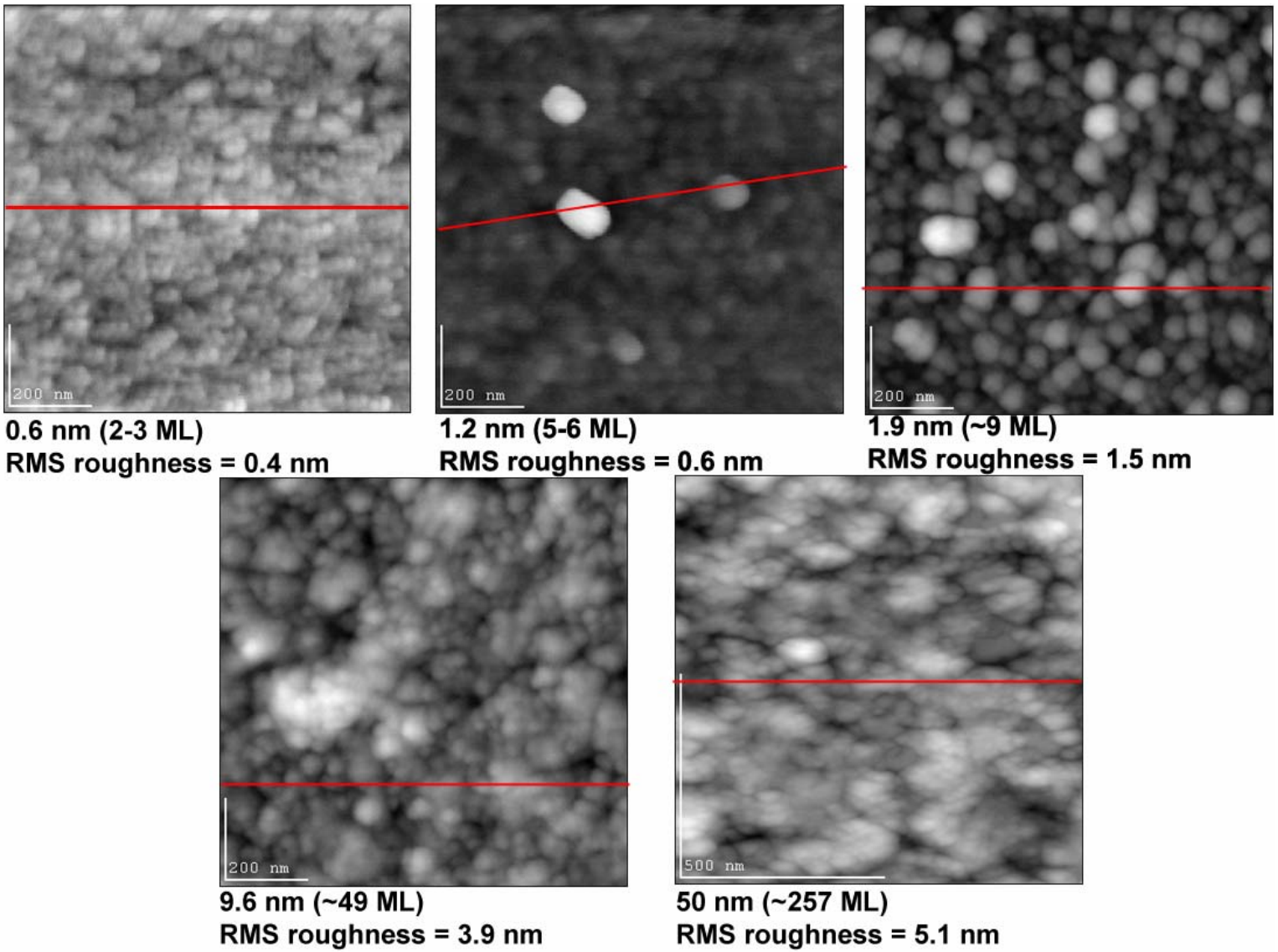

Figure 4.26. AFM images of Ni films annealed on standard surfaces. The red line across each AFM image correspond to a line profile in Figure 4.27.

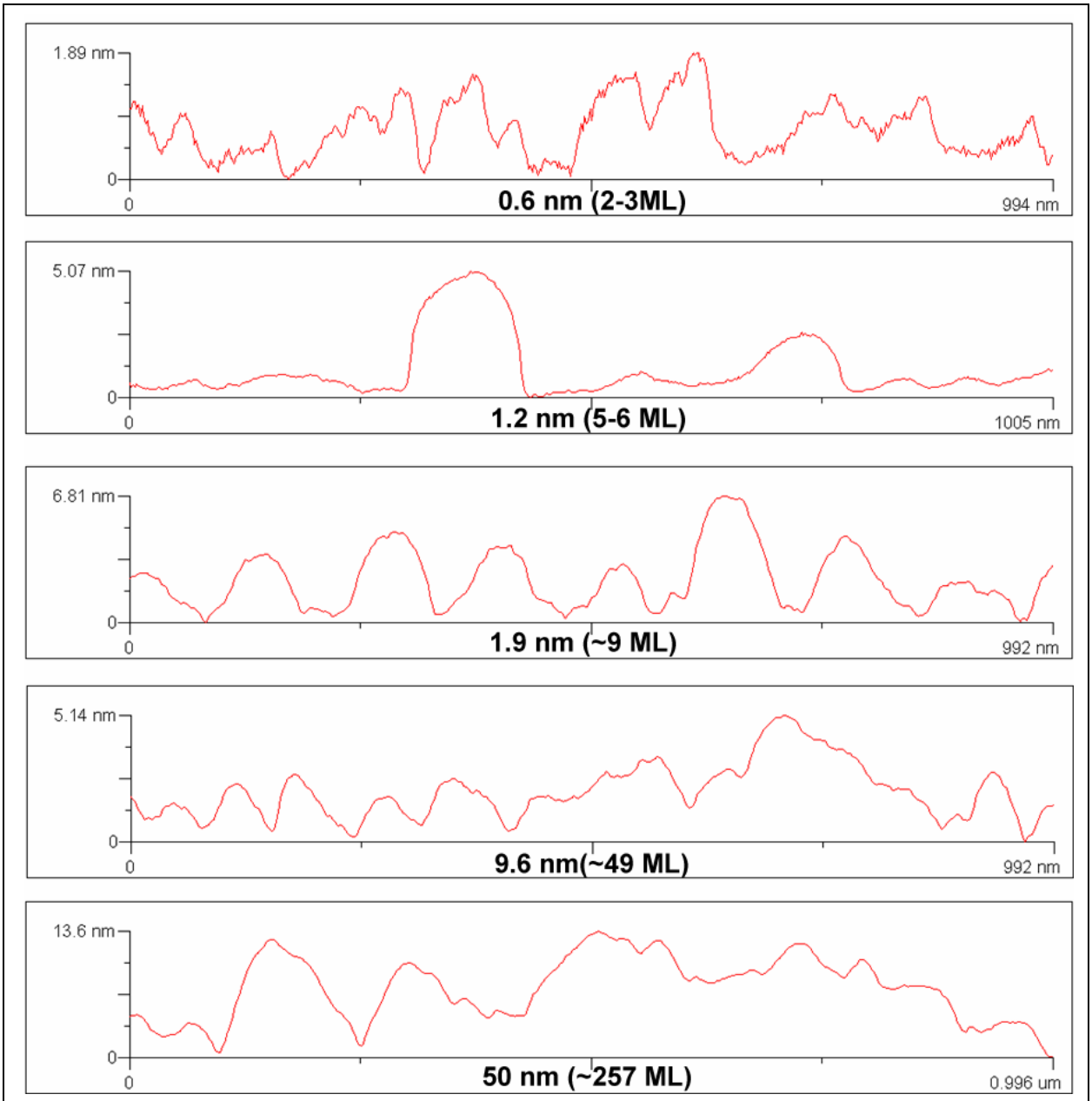

Figure 4.27. Line profiles for AFM images of annealed Ni films on standard surfaces . Note the line profiles correspond to the red lines across the respective images in Figure 4.26.

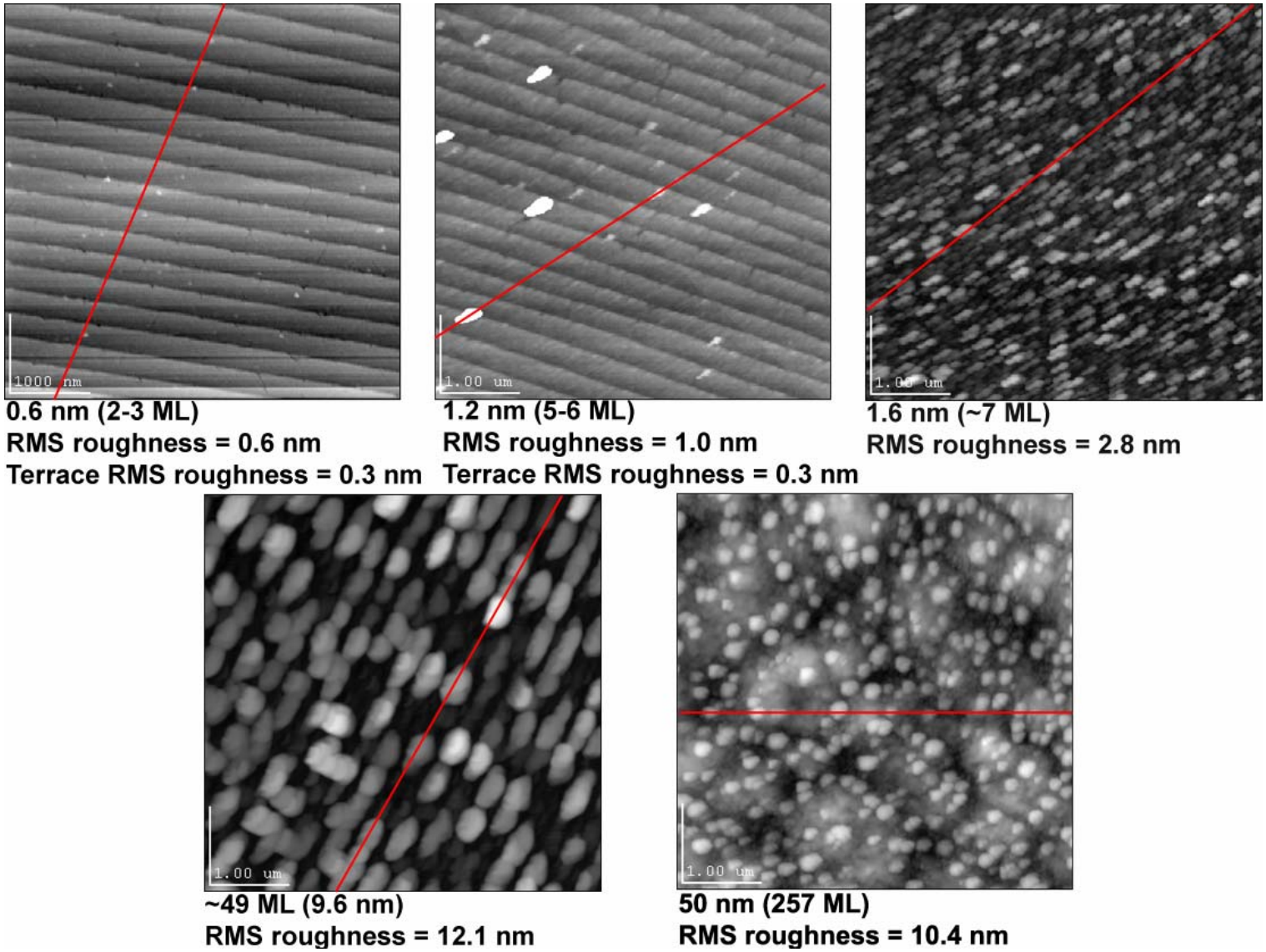

Figure 4.28. AFM images of Ni films annealed on stepped surfaces. The red line across each AFM image correspond to a line profile in Figure 4.29.

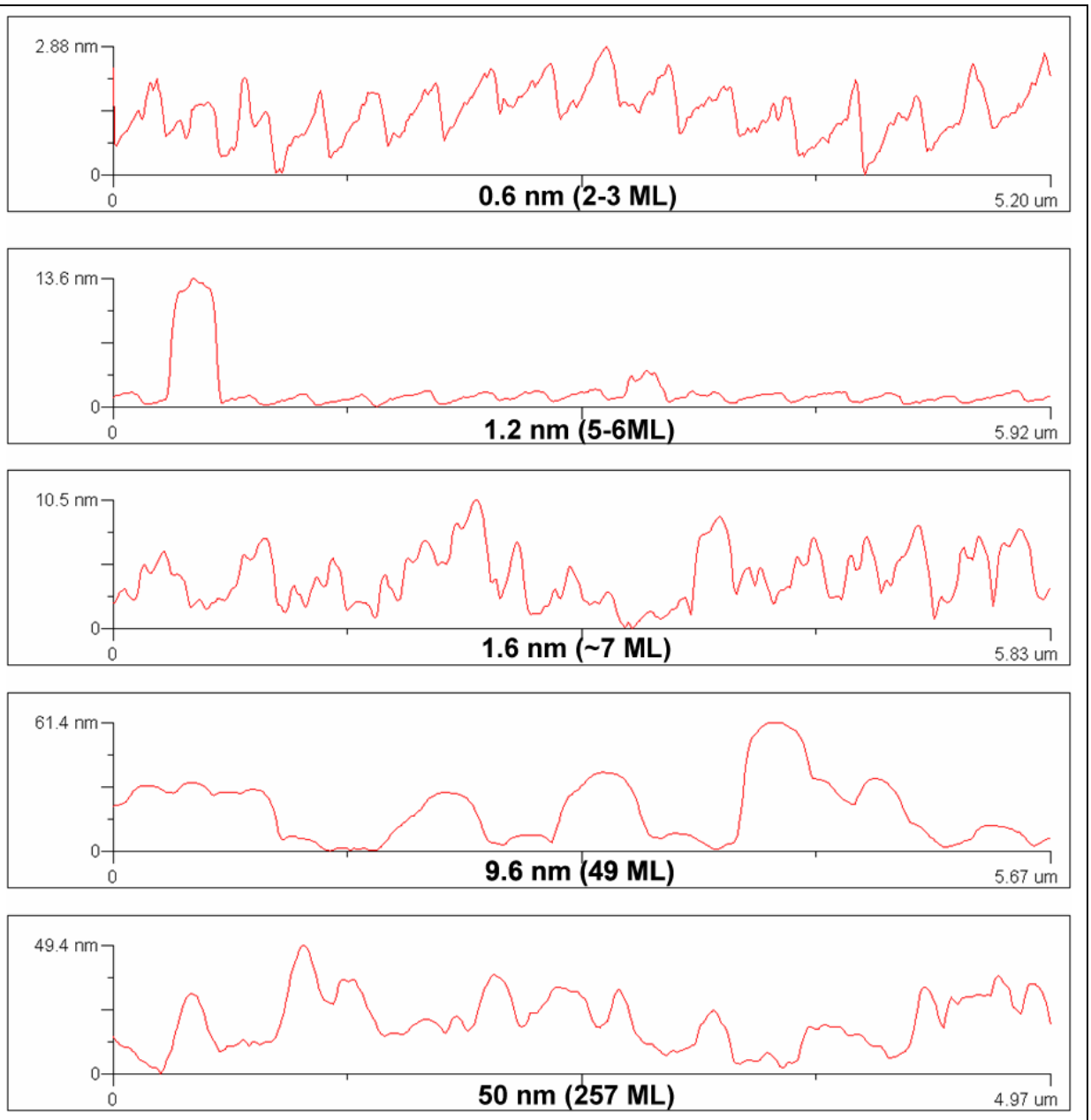

Figure 4.29. Line profiles for AFM images of annealed Ni films on standard surfaces. Note the line profiles correspond to the red lines across the respective images in Figure 4.28.

4.3.3 Summary of Ni Study Results

Below is a list areas of interest and key results from the Ni Studies discussed in section 4.2.1, and 4.2.2. These results are later referred to in the summary in Chapter 5.

Ni films on Si (100)

- React at room temperature to form Ni silicides
- When annealed elemental Si is segregated onto the surface

Un-annealed Ni films on SiC

- React at room temperature to form carbide clusters on either stepped or standard surfaces
- No indication of reaction between Ni and Si (in SiC) at room temperature
- Other than sparsely populated carbide clusters the films are conformal with the initial surface.

Annealed Ni intermediate [9.6 nm (~49 ML) or less] films on SiC

- Form Graphitic C structures on both stepped and standard surfaces
- Graphite films on stepped surfaces are thinner than on standard surfaces

Annealed Ni thick [46.5 nm (~216 ML)] films on SiC

- Form a C+Ni_xSi/SiC structure on standard surfaces
- Form a Ni_xSi/C/SiC structure on stepped surfaces

Annealed Ni film morphology on SiC

- Depends on thickness
- Depends on initial surface state

CHAPTER 5: SUMMARY, CONCLUSIONS AND RECOMMENDATIONS

The goal of this research was to investigate the interaction of Pd and Ni with stepped 6H-SiC surfaces and to compare these interactions with those on the standard surfaces used to fabricate SiC devices. In the course of these studies, many observations were made concerning the initial state of the stepped and standard SiC surface as well as the interactions of Pd and Ni on the Si (100) hydrogen terminated surface.

The primary conclusion of this research is that the initial state of the SiC surface (stepped vs. standard), the initial surface stoichiometry, and the initial film thickness strongly influence thermal stability of the metal semiconductor interface. The results clearly indicate that the stepped surfaces with large atomically flat terraces provide distinct advantages in this respect. Our results suggest, and recent work elsewhere indicates, that significant improvement in sensor performance can be achieved by improving the substrate quality. Work is in progress to correlate these conclusions with electrical characterization.

AES results analysis that the Si/C ratio was typically 0.8 for the stepped surfaces and 0.6 for the standard surfaces. That is, both the stepped and standard surfaces are C rich, but the stepped surface is more stoichiometric than the standard surface. As compared to SiC films grown *in-situ*, (where oxygen and extraneous C contamination of the surfaces are not a problem), the Si-LMM and C-KLL AES lineshapes for the stepped surfaces are more carbide like than those for the standard surfaces. In particular, the C-KLL peak for the standard surface shows evidence of significant levels of C-C bonding.

This is consistent with the enhanced levels of C on those surfaces. A residual, sub-monolayer, level of surface oxygen was always observed on the hydrogen etched (HF dipped) surface.

AES Si-LMM spectra of Pd on the hydrogen terminated Si (100) 1x1 surface shows that there is significant interdiffusion and reaction, even at room temperature, to form silicides. This clearly indicates a remarkable level of intermixing and reaction at room temperature. Our observations of the Si-LMM lineshape for Pd-silicides were consistent with those previously reported. The results suggest that after annealing at 500 ^{o}C, Si is segregated onto the silicide surface.

Results for Ni on the hydrogen terminated Si (100) 1x1 tell a similar story to that of Pd. At room temperature, there is evidence for interdiffusion and reaction to form Ni silicide. For the small amount of residual C on the Ni surface, the C-KLL spectra indicates that there is a reaction to form Ni carbide. This is observed only at room temperature. After annealing 700 ^{o}C, the carbide is not observed, and the evidence suggests that Si is segregated onto the Ni silicide surface.

For the interaction of Pd on SiC, AFM indicates that all un-annealed films on both the stepped and standard surfaces were conformal with the initial surface. There is also no evidence for the room temperature reaction of Pd with SiC for either the stepped or the standard surfaces. This indicates that there is much less intermixing and reaction for SiC than Si. The conclusion is that Pd is more stable on SiC than on Si. If the SiC surface was stoichiometric or Si-rich, we would expect to see evidence for silicide formation, particularly for the thinnest films. This most likely does not occur because we are working on with a C-rich surface for both the standard and stepped surfaces.

After annealing at 670 ^{o}C, Pd films on stepped surfaces show clear evidence of interdiffusion and reaction, and the resulting morphology and composition are dependent on the initial substrate preparation as well as the initial film thickness. The AES results indicate that Si diffuses out of the stepped surface to form Pd_xSi leaving a graphitic under layer. AFM results indicate that the Pd_xSi films of 0.5 nm - 10.5 nm form crystallites on the stepped surface. In contrast, Pd diffuses into the standard surface to form Pd_xSi with a graphitic over layer. Moreover, the AFM results show no evidence for crystallite formation on the standard surface. Thus, while reactant mobility is important for both standard and stepped surfaces, the nature of the transport is controlled by the initial state of the surface.

AES and AFM results of un-annealed Ni films on both stepped and standard surfaces are almost identical. The AES spectra show clear evidence of Ni carbide formation at room temperature. The Si-LMM peak is simply attenuated with no peak shape change. That is, there is no evidence for silicide formation. This may again be a consequence of working on a C-rich substrate surface for both the standard and stepped surfaces. Ni films are conformal for both the stepped and standard surfaces and there is evidence that the carbide forms clusters on the surface.

For Ni Films annealed at 700 ^{o}C on either surface, the Ni carbide features in C-KLL spectra are no longer observed and clusters are gone. Again this leads us to believe that the clusters observed in AFM images of un-annealed Ni films on SiC are carbidic in nature. This agrees with the literature that states that Ni carbide (Ni_3C) is not stable above 500 ^{o}C, and therefore it is not observed on annealed films.

AES results for thin (1.2 nm and less), annealed Ni films on stepped surfaces also show less reaction and less graphite formation compared to standard surfaces. That is, the AES results suggest that Ni is more stable on stepped surface than on the standard surface. AFM results show ordered structures (graphite clusters or platelets) for films 1.2nm - 9.6 nm thick on the stepped surface but round clusters are observed on the standard surface. AES suggests that these formations are mainly graphitic C. AFM images of 50 nm thick film show smaller clusters sitting on top of larger hillocks for the stepped surface. These are correlated with silicide near or on the surface. Hence, the clusters are most likely Ni silicide on graphite hillocks. AFM images of the standard surface only show large hillocks, and the AES spectra reveal Ni silicide formation near or no the surface but it is not clear if the silicide is near or on the surface. Like with Pd on SiC, this leads us to believe that for Ni-on SiC reactant mobility plays an important role in Nickel silicide and graphite formation / film microstructure, and is controlled by the initial state of the surface.

For both Pd and Ni films on SiC reactant mobility plays an important role in silicide and graphite formation and establishing the film microstructure. In both cases reactant mobility is directly linked to the initial SiC surface structure, both in terms of crystal defects and chemical composition. In both cases, films on stepped surfaces are more stable than the standard surface.

Work performed elsewhere[45] indicates that there are advantages to fabricating SiC devices on stepped SiC surfaces. Our research has shed much light on the effects of the initial surface state (i.e., stepped versus standard) on interactions of Pd and Ni with SiC.

What is needed now is to correlate our observations with device performance measurements.

From a fundamental point of view there are also three areas where additional research needs to be conducted. First, there is a question concerning the C-rich SiC surface stoichiometry. Second, there are still questions concerning the remaining oxygen on the stepped surface. Third, the interaction of a metal that forms a stable high temperature carbide, and not silicide, needs to be examined.

REFERENCES

[1] P.G. Neudeck, Electrical Impact of SiC Structural Defects on High Field Devices *Materials Science Forum*, Vol. **338-342**, 1161, (2000).

[2]L-Y. Chen, G.W. Hunter, P.G. Neudeck, and D Knight, X-ray photoelectron spectroscopy study of the heating effects on Pd/6H-SiC, *J. Vac. Sci. Technol. A*, **16(5)**, 2890 (1998).

[3]C.Y. Peng, *Silicon Carbide Epitaxial Growth Using Methalsilanes as Gas Sources, Ph.D. Dissertation*, Morgantown, WV: West Virginia University (2004).

[4] CREE, Inc. 4600 Silicon Drive Durham, NC 27703, http://www.cree.com (2005).

[5]K.S. Ziemer, *Studies of the initial stage of silicon carbide growth on silicon, Ph.D. Dissertation*, Morgantown, WV: West Virginia University (2001).

[6]M. Wiets, M. Weinelt, and T. Fauster, Electronic structure of SiC (0001) surfaces studied by two-photon photoemission, *Phys. Rev B.*, **68**, 125321 (2001).

[7]A.M. Cowley, and S.M. Sze, Surface States and Barrier Height of Metal-Semiconductor Systems, *J App. Phys.*, **36**, 3212 (1965).

[8]M. Mehregany, and C. Zorman, SiC MEMS: Opportunities and Challenges for Applications in Harsh Environments, *Thin Solid Films* **355-356**, 518 (1999).

[9]S. Watanabe, K.Osato, S. Ninimiya, M. Mukaida, T. Tsunoda, and Y. Imai, SiC Thin Film Preparation by ArF Excimer Laser Chemical Vapor Deposition Part 1: Rate of Photolysis of Alkylsilanes by ArF Excimer Laser and Their Decomposition Products, *Thin Solid Films* **274**, 70 (1996).

[10]P. Liaw, and R.F. Davis, Epitaxial Growth and Characterization of B-SiC Thin Films*, Journal of the Electrochemical Society* **132 (3)**, 642 (1985).

[11]M. Mehregany, C. Zorman, N. Rajan, and C.H. Wu, Silicon Carbide MEMS for Harsh Environments*, Proceedings of the IEEE* **86 (8)**, 1594 (1998).

[12]Vision 21: The ultimate power plant concept,. U.S. Department of Energy, http://www.fossil.energy.gov/programs/powersystems/vision21/ (July 2005)

[13]C.E. Weitzel, J.W. Palmour, C.H. Carter, Jr., K. Moore, K.J. Nordquist, S. Allen, C. Thero, and M. Bhatnagar, Silicon Carbide High-Power Devices, *IEEE Transactions On Electron Devices* **43**, 1732, (1996).

[14]C.E. Weitzel, and K.E. Moore, Performance Comparison of Wide Bandgap

Semiconductor rf Power Devices, *Journal of Electronic Materials* **27 (4)**, 365 (1998).

[15]F. Nava, E Vittone, P.G. Fuochi, and C. Lanzieri, Radiation tolerance of epitaxial silicon carbide detectors for electrons and γ-rays, *Nuc. Inst. and Meth. in Phys. Re A* **514**, 126(2003)

[16]D.A. Scheiman, G.A. Landis, and V.G. Weizer *AIP Conf. Proc.*M. S. ElGenk ed parts 1 and 2, **458**, 616 (1999).

[17] S.O. Kasap *Electronic Materials and Devices 2nd Ed.*, McGraw-Hill Companies , Inc., New York (2002).

[18]A. Lloyd Spetz, L. Uneues, H. Svenningstrop, P. Tobias, L.-G. Ekedahl, O. Larsson, A Goras, S. Savage,, C Harris, P. Martensson, R. Wigren, P. Salomonsson, B. Haggendahl, P. Ljung, M. Mattsson, and I. Lundstrom, SiC Based Field Effest Gas Sensors for Industrial Applications, *phys. stat. sol.*, **185**, 15 (2001).

[19]S. Zangooie, H. Arwin, I. Lundström, and A. Lloyd Spetz, Ozone Treatment of SiC for Improved Performance of Gas Sensitive Schottky Diodes, *Sensors and Actuators B*, **58**, 389 (1999).

[20]U.S. Dept. of Commerce: National Bureau of Standards *Crystal Data Determinative Tables 3rd ed. Vol. II InorganicCcompounds* editor J.D.H. Donnay and H.M. Ondik. Washington DC (1973).

[21]R.A. King, R.A.D. Mackenzie, and G.D.W. Smith, "Field emission and atom probe field ion microscope studies of palladium-silicide-coated silicon emitters", *J. Vacuum Sci. Technol*. B, **13**, 603 (1995).

[22]M.F. Singleton, and P. Nash, C-Ni (Carbon Nickle), *Phase Diagrams of Binary Alloys ed. P. Nash*, ASM International, Materials Park, OH, 50 (1991).

[23]M. Qin, V.M.C. Poon,, and S.C.H. Ho, Investigation of Polycrystalline Nickel Silicide Films as Gate Materials, *J. Electrochem Soc*, **148**, G271 (2001)

[24]J. Crofton , L.M. Porter, and J. R. Williams, The Physics of Ohmic Contacts to SiC, *phys. stat. sol. (b)*,**202**, 581 (1997).

[25]Silicon Carbide Growth and Characterization, Carnefie Mellon SiC Research, http://neon.mems.cmu.edu/skowronski/SiC%20front.htm (July 2005).

[26]R.S. Kern, and R.F. Davis, Deposition and Doping of Silicon Carbide by Gas-Source Molecular Beam Epitaxy, *App. Phys. Letters*, **71**, 1356 (1997).

[27]J. Takahashi and N. Ohtani, Modified-Lely SiC Crystals Grown in [1100] and [1120] Directions, *phys. stat. sol.(b)*, **202**,163 (1997).

[28]J.A. Lely, *Ber Dtsch Keram Ges*, **32**, 229 (1955).

[29]R.C. Glass, D. Henshall, V. F. Tsvetkov, and C. H. Carter Jr., SiC Seeded Crystal Growth, *phys. stat. sol. (b)*, **202**, 149 (1997).

[30]Compound Semiconductor Solutions, Dow Corning Corporation Corporate Center, PO box 994,Midland MI 48686-0994, http://www.dowcorning.com/content/compsemi/default.asp (July 2005).

[31]R. Kakanakov, L. Kassamakova-Kolaklieva, N. Hristeva, G. Lepoeva, and K. Zekentes, Thermally Stable Low Resistivity Ohmic Contacts for High Power and High Temperature SiC Device Applications, *23rd International Conference on Microelectronics. Proceedings*, **1**, 205 (2002).

[32]M. W. Cole, P. C. Joshi, and M. Ervin, Fabrication and characterization of pulse laser deposited Ni_2Si Ohmic contacts on n-SiC for high power and high temperature device applications, *J App. Phys.*, **89**, 4413, (2001)

[33]L. Scaltrito, G. Fanchini, S. Porro, M. Cocuzza, F. Giorgis, C.F. Pirri, P. Mandracci,C. Ricciardi, S. Ferrero, C. Sgorlon, G. Richieri, and L. Merlin, Surface analysis and defect characterization of 4H–SiC wafers for power electronic device applications, *Diamond and Related Materials*, **12**, 1224 (2003).

[34]H.G. Henry, G. Augustine, G.C. DeSalvo, R.C. Brooks, R.R. Barron, J.D. Oliver, Jr., A.W. Morse, B.W. Veasel, P.M. Esker, and R.C. Clarke, S-band operation of SiC power MESFET with 20 W (4.4 W/mm) output power and 60% PAE, *IEEE Transactions on Electron Devices*, **51**, 839 (2004).

[35] I. Lundstrom, S Shivaraman, C. Svensson, and L. Lundkvist, A hydrogen-sensitive MOS field-effect transistor, *App. Phys. Lett.*, **26**, 55 (1975).

[36]Silicon Carbide High Temperature Integrated Electronics and Sensors, NASA Glenn Research Center, http://www.lerc.nasa.gov/WWW/SiC.html (July 2005).

[37]L-Y. Chen, G.W. Hunter, P.G. Neudeck, G. Bansal, J. B. Petit, D. Knight, C-C. Liu, and Q. Wu, Electronic and Interfacial Properties of Pd/6H-SiC Schottky Diode Gas Sensors, L *Transactions of Third International High Temperature Electronics Conference*, *Albuquerque, New Mexico* June 9–14, (1996).

[38]V.M. Bermudez Auger and electron energy-loss study of the Pd/SiC interface and its dependence on oxidation, *Applications of Surface Science*, Vol. 17, 12 (1983).

[39]D Briggs, and M.P. Seah, *Practical Surface Analysis, 2nd ed.*, West Sussex,

England: John Wiley & Sons (1983).

[40] G.W. Hunter, P.G. Neudeck, L-Y Chen, D.Knight, C.C. Liu, and Q.H. Wu, Silicon carbide based detection of hydrogen and hydrocarbons, *Inst Phys.Conf Ser,* No 142 Chapter 4 (1995).

[41]S. Yu. Davydov, A.A. Lebedev, O.V. Posrednik, and Yu. M. Tairov, Role of Silicon Vacanies in Formation of Schottky Barriers at Ag and Au Contacts to 3C- and 6H-SiC, *Semiconductors*, **36**, 653 (2002).

[42]I.P. Nikitina, K.V. Vassilevski, N.G. Wright, A.B. Horsfall, A.G. O'Neill, and C.M. Johnson, Formation and role of graphite and nickel silicide in nickel based Ohmic contacts to n-type silicon carbide, *J App Phys*, **97**, 083709-1 (2005).

[43]L-G. Ekedahl, M. Eriksson, and I. Lundstrom, Hydrogen Sensing Mechanisms, *Acc. Chem. Res.*, **31**, 249 (1998).

[44]P.G. Neudeck, J.A. Powel, G.M. Beheim, and E.L. Benavage, Enlargment of step-free SiC surfaces by homoepitaxial web growth of thin SiC cantilevers, *J. App. Phys.*, **92**, 2391, (2002).

[45]G.W. Hunter, P.G.Neudeck, J. Xu, D. Lukco, A. Trunek, M. Artale, P. Lampard,D. Androjna, D. Makel, B. Ward, and C.C. Lu, Development of SiC-Based Gas Sensors for Aerospace Applications, *Mat. Res. Symp. Proc.*, **815**, J4.4.1 (2005).

[46]R.T. Tung, J.M.Gibson and J.M. Poate, Formation of Ultrathin Single Crystal Silicide Films on Si: Surface and Interfacial Stabilization of Si-Ni2 Epitaxial Structures, *Phys. Rev Lett.*, **50**, 429 (1983).

[47]K. Robbie, S.T. Jemander, N. Lin, C. Hallin, R. Erlandsson, G. V. Hansson, and L.D. Madsen, Formation of Ni intercalation compounds, *Phys, Rev B*, **65**, 155401-1 (2001).

[48] R.T. Tung, J.M. Poate, J.M. Gibson, and D.C. Jacobson, Epitaxial Silicides, *Thin Solid Films*, **93**, (1982).

[49]T. Nakamuram, and M. Satoh, Schottky barrier height of a new Ohmic contact $NiSi_2$ to n-type 6H-SiC, *Solid-State Electron.*, **46**. 2063 (2002),

[50]F. La Via, F. Roccaforte, A. Makhtari, V. Raineri, P. Musumeci, and L. Calcagno, Structural and electrical characterisation of titanium and nickel silicide contacts on silicon carbide,*Microelectron. Eng.*, **60**, 269 (2002).

[51]A. Oya and H. Marsh, Phenomena of caltalytic graphitization, *J. Mater. Sci*, **17**, 309 (1982).

[52]Ts. Marinova, V. Krastev, C. Hallin, R. Yakimova, and E. Janzen, Interface chemistry and electric characterization of nickel matallisation on 6H-SiC, *Appl. Surf. Sci.*, **99**, 119 (1996).

[53]M.G. Rastegaeva, A. N. Andreev, A. A. Petrov, A. I. Babanin, M. A. Yagovkina, and I. P. Nikitina, The influence of temperature treatment on the formation of Ni-based Schottky diodes and Ohmic contacts, *Mater. Sci. Eng. B,* **46**, 254 (1997).

[54]S.Y. Han, K.H. Kim, J.K. Kim, H.W. Jang, K.H. Lee, N.K. Kim, E D. Kim, and J.L. Lee, Ohmic contact formation mechanism of Ni on *n*-type 4H-SiC, *Appl. Phys. Lett*,. **79**, 1816 (2001).

[55]P. Auger J. Phys. Radium **6**, 205 1925

[56]J.M Lannon, Jr., *Nucleation and Growth Studies Relevant to Diamond Thin Film Synthesis, Ph.D. Dissertation*, Morgantown, WV: West Virginia University (1996).

[57]J.S. Gold, *Characterization of a novel methyl radical source and related thin film growth studies, Ph.D. Dissertation,* Morgantown, WV: West Virginia University (2002).

[58]A. Amoddeo, L.S. Caputi, and E. Colavita, Carbon Auger lineshapes on Ni(111) surface: evidence for new phases, J. Electron, *Spectrosc. Relat. Phenom.*, **62**, 263 (1993).

[59]A. M. D. Assa'd, and M. M. El Gomati, Backscattering Coefficients for Low Energy Electrons, *Scanning Microscopy*, **12**, 185 (1988).

[60]O.K.T. Wu, and E.M. Butler, Auger signal intensity dependence on surface area (roughness), *J. Vac. Sci. Technol,*, **20**, (1982).

[61]P.H. Holloway, The Effect of Surface Roughness on Auger Electron Spectroscopy, *J. Elect. Spec. and Rel. Phenom*,**7**, 215 (1975).

[62]I. Lindau, and W.E. Spicer, The Probing Depth in Photoemission and Auger-Electron Spectroscopy, *J. Elect. Spec. and Rel. Phenom.*, **3**, 409 (1974).

[63] C. J. Powell, Attenuation Lengths of Low-Energy Electrons in Solids, *Surface Science*, **44**, 29 (1974).

[64] M. P. Seah, and W. A. Dench, Quantitative Electron Spectroscopy of Surfaces: A Standard Data Base for Electron Inelastic Mean Free Paths in Solids, *Surface and Interface Analysis*, **1**, 2 (1979).

[65]R.E. Ballard, Emperical mean free path curves for electron scattering in solids, *J. Elect. Spec. and Rel. Phenom.*, **25**, 75, (1982).

[66]C. J. Powell, and A Jablonski, *NIST Electron Inelastic-Mean-Free-Path Database*, U.S.

Department of Commerce, Technology Administration Standard Reference Data Program, (December 2000).

[67]Scanning Probe/Atomic Force Microscopy: A Technology Overview *Veeco Instruments Inc. Application Note*, AN48 (2003).

[68]MikroMash USA 9755 SW Commerce Cir, Suite B-1Wilsonville, OR 97070, http://www.spmtips.com (July 2005).

[69]R. Howland, and L. Benatar, *A Practical Guide to Scanning Probe Microscopy,* ThermoMicroscopes (2000).

[70]C.B. Prater, P. G. Maivald K.J. Kjoller, and M.G. Heaton, Tapping Mode Imaging Applications and Technology, *Veeco Instruments Inc. Application Note*, AN04 (2004)

[71]Veeco Instruments Inc., 100 Sunnyside Blvd. Ste. B, Woodbury New York 11797-2902, http://www.veeco.com (July2002).

[72]L.S. Hirsch, *Preparation of Substrates for Semiconductor Growth Using Atomic Hydrogen, Masters Thesis,* Morgantown, WV: University of West Virginia (1998).

[73] Physical Electronics Industries, Inc., *Handbook of Auger Electron Spectroscopy, 2nd ed*., Eden Prarie, MN (1978).

[74]J.M. Lannon, J.S. Gold, and C.D. Stinespring, Evidence for surfactant mediated nucleation and growth of diamond, *Appl. Phys. Lett.* **73**, 226 (1998).

[75]G.E. McGuire, *Auger Electron Spectroscopy Reference Manual*, Plenum Press New York (1979).